博士論文

Study on Multi-Electron Transfer Reactions Based on Spectroelectrochemistry and Enzyme Genetics

(分光電気化学及び酵素遺伝学に基づく
多電子移動反応に関する研究)

応用化学専攻　石北研究室

37-157125　　大岡英史

Contents

Chapter 1

General Introduction

1.1 Multi-Electron Transfer Reactions

Multi-electron transfer reactions are a class of redox half-reactions which involve more than one electron.[1–4] These reactions are important in terms of efficient energy–material conversion, which is not only a requirement of a sustainable human society,[5–8] but also a fundamental aspect governing biological processes.[2,9–14]

For example, the four-electron transfer between water and oxygen are core components of photosynthesis and aerobic respiration, which are known to be the two main energy production pathways in Nature (Figure 1.1). In photosynthesis,[15,16] light energy is used to drive the endergonic oxygen evolution reaction ($2\,H_2O \rightarrow O_2 + 4\,H^+ + 4\,e^-$, OER), which liberates electrons from water molecules. The attained electrons can then be used to reduce atmospheric CO_2 into biomass ($6\,CO_2 + 24\,H^+ + 24\,e^- \rightarrow C_6H_{12}O_6 + 6\,H_2O$). On the other hand, aerobic respiration uses molecular oxygen as a terminal electron acceptor[17] *via* the oxygen reduction reaction ($O_2 + 4\,H^+ + 4\,e^- \rightarrow 2\,H_2O$, ORR). The combustion of biomass *via* aerobic respiration yields a cycle of carbon and oxygen elements with no net emission, which is a requirement of a sustainable energy–material conversion system.

It is important to note that the hydrogen economy, which is attracting widespread attention recently, is equivalent to the biological energy cycle at a fundamental chemical level.[18–29] Namely, the four-electron interconversion between water and oxygen are used to generate a transient, electron rich, energy carrier (biomass in the biosphere, hydrogen in the hydrogen economy). In this way, multi-electron transfer reactions are important for both biological and artificial energy conversion processes.

Oxygen Evolution
Photosynthesis

O_2

Oxygen Reduction
Respiration

$2H_2O \rightarrow$
$O_2 + 4H^+ + 4e^-$

Biomass

$(CH_2O)_n$

$O_2 + 4H^+ + 4e^-$
$\rightarrow 2H_2O$

Fuels

Solar-driven
water electrolysis

H_2O

Fuel Cells
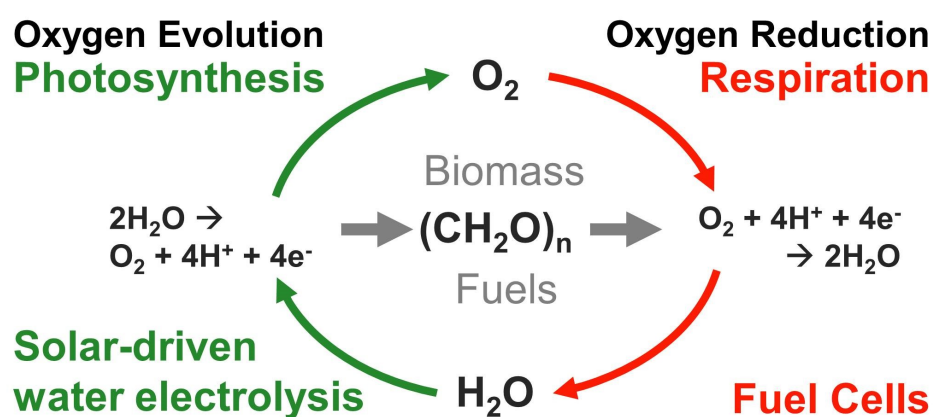
Fig. 1.1 The sustainable energy–material conversion strategy in Nature based on the reversible redox interconversion of water and oxygen. Industrial processes which are chemically equivalent of the reactions performed in biology are also indicated in this figure.

However, because energy–material conversion is a fundamental aspect of biology, the regulation of multi-electron transfer processes is known to influence factors such as cancer,[30,31] aging,[32,33] and evolution.[34] For example, aerobic respiration (ORR) is the main energy acquisition pathway for healthy human cells. However, cancer cells are known to prefer anaerobic fermentation, which is known to be less energy efficient. This tendency, known as the Warburg effect,[35] may be because the generation of reactive oxygen species (ROS) triggers programmed cell death (apoptosis),[36–38] whose main function is to terminate malignant cells. By suppressing the generation of ROS, cancer cells effectively suppress a major mechanism of cell death, allowing themselves to proliferate for longer periods compared to normal cells. The relationship between aging and ROS has also been proposed at the individual (multicellular) scale, where cumulative cell damage due to ROS is explained to be the main cause of aging (Free radical theory of aging).[39–41] Therefore, aerobic respiration is intricately linked to many of the health issues which are being most widely studied today. On the other hand, however, it has been hypothesized that aerobic respiration, or to be more specific, the development of the mitochondria, has allowed intense diversification of biological species, due to the drastic increase of the energy available per gene.[34] Therefore, understanding multi-electron transfer reactions is important for a vast array of processes, not only to enhance human sustainability, but also to establish a deeper understanding of life processes in general. In the introduction section of each of the following chapters, the importance of multi-electron transfer will be revisited from different angles based on arguments focusing on a specific reaction or aspect of multi-electron transfer.

1.2 Current Theory of Multi-Electron Transfer Reactions

1.2.1 Overview of the d-band Theory

There has been extensive effort to understand multi-electron reactions, with the most notable approach being the d-band theory. The d-band theory is at its heart an extension of the Sabatier principle,[42–44] which states that an ideal catalyst must bind an intermediate neither too strongly nor too weakly. This is because a strong catalyst-substrate interaction would hinder the desorption process, while one that is too weak does not allow the catalyst to play a sufficient role during the reaction. Although the Sabatier principle was first proposed by Paul Sabatier in 1911,[42] the advancement of computational chemistry has allowed the catalytic activity of a given surface to be predicted based on the binding energies of various reaction intermediates.[45–47]

There are numerous reports on the successful application of this approach, and the evaluation and comparison of a wide array of materials based on a common descriptor have proved beneficial in the field of catalysis. Below, the basic concept of the d-band theory will be briefly illustrated using the acid–base mechanism of the OER as an example.[*1] This mechanism has been investigated extensively by many groups, such as Norskov[48–51] and Koper[52,53] groups. The elementary reactions are assumed to be:

[*1] There are two well-known OER mechanisms in the literature (the acid–base mechanism and the direct-coupling mechanism), see Chapter 2 for details.

$$H_2O \text{ (liq.)} + M \rightarrow M{-}OH + H^+ + e^- \tag{1.1}$$

$$M{-}OH \rightarrow M{=}O + H^+ + e^- \tag{1.2}$$

$$M{=}O + H_2O \rightarrow M{-}OOH + H^+ + e^- \tag{1.3}$$

$$M{-}OOH \rightarrow O_2 + H^+ + e^- + M \tag{1.4}$$
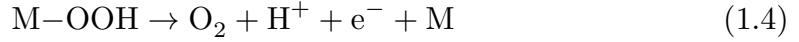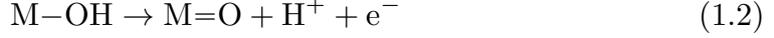
when M indicates a vacant metal site, and M-X indicates an adsorbed form of X. The Gibbs free energy change for each reaction is therefore as follows:

$$\Delta G_1 = \Delta G_{M{-}OH} - \Delta G_{M{-}H_2O} - eU + k_B T \ln \alpha_{H^+} \tag{1.5}$$

$$\Delta G_2 = \Delta G_{M{=}O} - \Delta G_{M{-}OH} - eU + k_B T \ln \alpha_{H^+} \tag{1.6}$$

$$\Delta G_3 = \Delta G_{M{-}OOH} - \Delta G_{M{=}O} - eU + k_B T \ln \alpha_{H^+} \tag{1.7}$$

$$\Delta G_4 = \Delta G_{M{-}O_2} - \Delta G_{M{-}OOH} - eU + k_B T \ln \alpha_{H^+} \tag{1.8}$$

Here, the U stands for the electrode potential on the standard hydrogen electrode (SHE) scale, and $\ln \alpha_{H^+}$ stands for the proton activity.

By referring to the free energy change for $(H^+ + e^-)$ transfer to that of $\frac{1}{2}H_2$ transfer, the effect of electrochemical potential on the driving force of each elementary reaction can be calculated. In analogy to the experimental SHE reference scale, this model is now referred to as the computational hydrogen electrode (CHE) model.[43,46,54] The initial mechanistic assumption that one proton and one electron are transferred during each elementary reaction was primarily due to the existence of the CHE, which has difficulties in modeling the energies of reactions which involve non-equivalent amounts of protons and electrons. However, as all

Gibbs energy changes show the same dependence on U and $\ln\alpha_{H^+}$, these equations predict that the relative barriers of each individual step, and therefore the activity of the catalyst, do not depend on the pH. This does not always accurately depict what occurs experimentally,[55–57,57] as will be explained in detail in Chapter 3. However, the decoupling of protons and electrons, which is the origin of pH-dependent catalytic activity, is theoretically predicted to decrease the activity of the catalyst.[58] Therefore, the CHE model predicts the highest possible activity of a given material, and is a powerful method to screen various candidate materials.

This screening is done by predicting the overpotential of each material. Within this theoretical framework, the overpotential η_{OER} is assumed to be the minimum potential (U) where $\Delta G_1 \sim \Delta G_4 \leq 0$. Therefore, η_{OER} is defined as:

$$\eta_{OER} = \frac{\Delta G_{OER}}{e} - 1.23 \text{ V} \tag{1.9}$$

when

$$\Delta G_{OER} = \max \left[\Delta G_1, \Delta G_2, \Delta G_3, \Delta G_4 \right] \tag{1.10}$$

Here, due to the Gibbs energy difference of the total reaction, the sum of $\Delta G_1 \sim \Delta G_4$ must be equal to 4.92 eV (1.23 × 4). Therefore, an OER catalyst with a minimum overpotential ($\eta_{OER} = 0$) must meet the following equality:

$$\Delta G_{OER} = \Delta G_1 = \Delta G_2 = \Delta G_3 = \Delta G_4 = 1.23 \text{ eV} \tag{1.11}$$

This is an important conclusion from the d-band theory. The Sabatier principle, which was the experimental precursor of this model, originally proposed the existence of an optimum binding energy between the catalyst and the substrate. Equation 1.11 is the quantitative representation of the Sabatier principle, as $\Delta G_1 \sim \Delta G_4$ are all dependent on the binding energies of intermediates such as

$\Delta G_{\text{M–OH}}$. Based on this equation, the ideal catalyst will perform each elementary reaction at the theoretical thermodynamic potential. Otherwise, the least favorable reaction will generate a finite overpotential ($\eta_{\text{OER}} > 0$). Therefore, there is currently extensive effort in the field of electrocatalysis to develop materials which possess reaction energetics that resemble the optimum landscape.[59–62]

However, based on a systematic analysis of binding energies, the existence of "scaling relationships" between the adsorption energies of different intermediates has become apparent.[48,61–65] These linear relationships are often unfavorable in terms of catalyst development. For example, on rutile type oxide materials:

$$\Delta G_{\text{M–OOH}} = 1.05 \; \Delta G_{\text{M–OH}} + 3.0 \text{ eV} \tag{1.12}$$

$$\Delta G_{\text{M–OH}} = 0.61 \; \Delta G_{\text{M=O}} - 0.58 \text{ eV} \tag{1.13}$$

These linear relationships impose restrictions on the catalytic activity, because Equation 1.11, which requires the energetic difference between $\Delta G_{\text{M–OH}}$ and $\Delta G_{\text{M–OOH}}$ to be 2.46 eV, cannot be satisfied. The existence of a finite overpotential ($\eta_{\text{OER}} > 0 \leftrightarrow \Delta G_{\text{OER}} > 1.23$ eV) is shown quantitatively below, by assuming $\Delta G_{\text{M–OOH}} \propto \Delta G_{\text{M–OH}}$ for simplicity:

$$
\begin{aligned}
\Delta G_{\text{OER}} &= \max[\Delta G_1, \Delta G_2, \Delta G_3, \Delta G_4] \\
&\geq \max[\Delta G_2, \Delta G_3] \\
&= \max[\Delta G_{\text{M=O}} - \Delta G_{\text{M–OH}}, \Delta G_{\text{M–OOH}} - \Delta G_{\text{M=O}}] \\
&= \max[\Delta G_{\text{M=O}} - \Delta G_{\text{M–OH}}, 3.0 \text{ eV} - (\Delta G_{\text{M=O}} - \Delta G_{\text{M–OH}})] \\
&\geq 1.5 \text{ eV}
\end{aligned}
\tag{1.14}
$$

This leads to a minimum η_{OER} of 0.27 V, which can be realized when ΔG_2 = ΔG_3 = 1.5 eV, and both ΔG_1 and ΔG_4 are smaller than 1.5 eV. A graphical representation of the analysis presented here can be found in Figure 1.2.
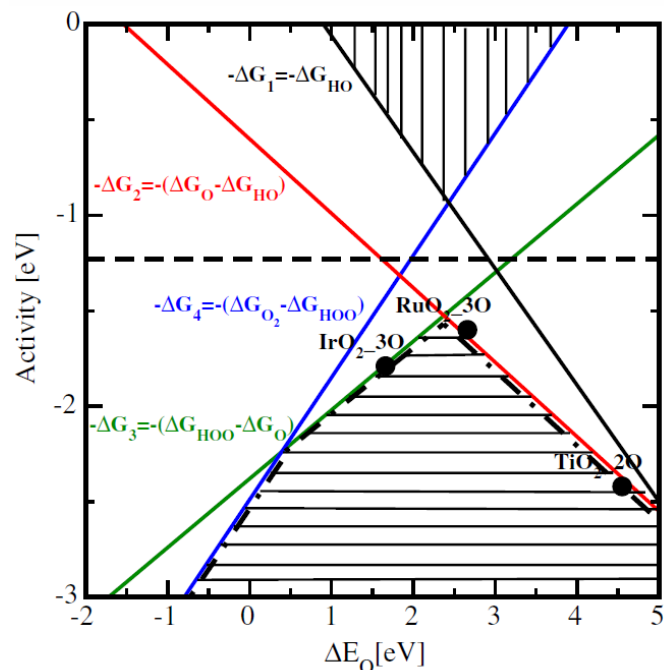
Fig. 1.2 A graphical representation of Equations 1.5 to 1.8 with respect to the oxygen binding energy. The X-axis (E_O, adsorption energy determined computationally) is related to the Gibbs free energy change by the following equation: $\Delta G_{M=O} = E_O +$ (Zero point energy correction) + (Entropy correction). Reproduced from reference 54 with permission from Elsevier.

Although the exact equations differ depending on the type of materials, the existence of linear correlations within binding energies is independent of the class of materials. These relationships arise because the binding energies of reaction intermediates are often similar. For example, a slope of nearly one between the OH and OOH intermediates can be rationalized by their similar conformation of binding through a metal–oxygen single bond.[54] The relationship between ΔG_{M-OH} and $\Delta G_{M=O}$, which shows a slope of *ca.* 0.5, can also be rationalized due to the fact that the M=O intermediate binds through a double bond.

The general methodology to quantify overpotentials using the adsorption energies of reaction intermediates, and the existence of scaling relationships which hinder the development of zero-overpotential catalysts, holds true for multi-

electron transfer reactions in general.[48,61–65] Therefore, optimizing the binding energy is one of the most widespread methods to develop efficient multi-electron transfer catalysts. Indeed, active materials have been developed based on the d-band theory for a variety of reactions such as oxygen evolution,[60] oxygen reduction,[59] and hydrogen evolution.[66]

The d-band theory still does not always give an accurate rationalization of observed experimental trends, however, because the CHE model often overestimates the activity. For example, if the proton and electron are decoupled, this reaction pathway deviates from the assumptions of the d-band theory (Figure 1.3), leading to a pH-dependent decrease in the activity.[58] Furthermore, the d-band theory does not take into account valence changes of the catalytic site. For example, in the biological OER enzyme photosystem II (PS II), the four Mn ions composing the active site are known to be oxidized from Mn^{3+} to Mn^{4+} in a stepwise manner.[67,68] The O–O bond formation steps discussed by the d-band principle takes place after the four charges necessary for water oxidation have been accumulated at the active site of PS II. Similar mechanisms involving the valence change of metal ions have also been observed for other multi-electron transfer enzymes such as hydrogenases, as well as artificial oxide catalysts such as MnO_2, Fe_2O_3, amorphous Ir oxide (IrO_x), and RuO_2 using *in-situ* spectroscopic techniques. Therefore, the charge accumulation process is expected to be a fundamental component of multi-electron transfer reactions.

For these reasons, although the simplicity of the d-band theory has proven to be useful for the development of efficient catalysts, it is important to develop a more intricate and multi-dimensional understanding of multi-electron transfer reactions. Not only would this allow for a more rational understanding of a wider variety of catalysts, thus further enhancing catalyst development, it would also help understand the plasticity and flexibility of energy-conversion processes in biology.
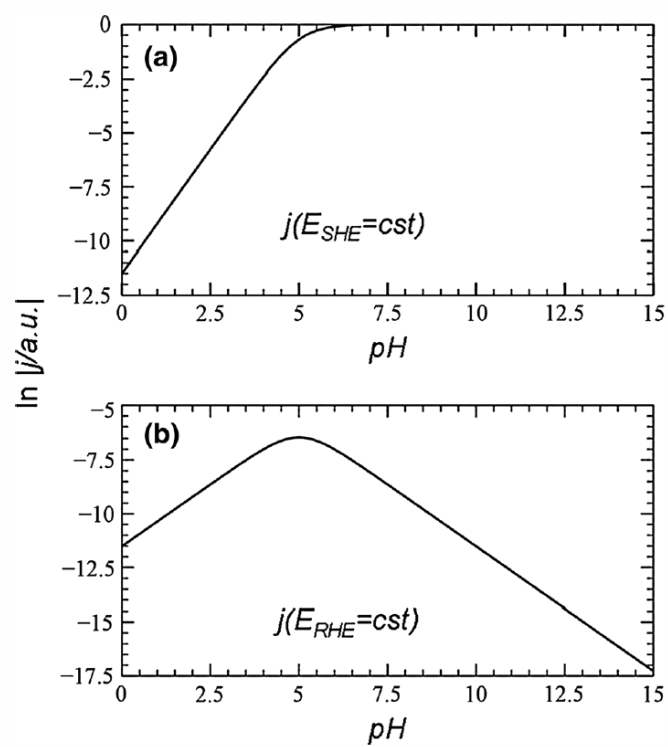
Fig. 1.3   Reaction rate of a stepwise proton–electron transfer process plotted with respect to the pH. Reproduced from reference 58.

1.3 Objective and Overview of this Thesis

The objective of this study is to expand the current understanding of multi-electron transfer by identifying reaction regulation strategies which were previously unconsidered. To this end, the author has studied various multi-electron transfer systems using a combination of spectroelectrochemical and bioinformatic techniques. The main part of this thesis consists of three chapters, each of which is dedicated to understanding multi-electron transfer regulation at a specific level. The chapters are ordered from microscopic to macroscopic point of views, and through this approach, the author has attempted to develop a multi-dimensional understanding of multi-electron transfer reactions.

In chapter 2, multi-electron transfer regulation was studied from the viewpoint of valence change and charge accumulation.[56,69,70] Through this approach, the author has attempted to clarify the mechanistic difference which leads to the discrepancy in the catalytic activity between 3d-metal catalysts and 4d/5d-rare metal catalysts. In order to achieve this goal, the oxygen evolution mechanism of IrO_x, which is one of the most active OER catalyst known today,[71,72] was studied using *in-situ* spectroelectrochemical techniques.[56,69,70] In contrast to 3d-metal catalysts such as MnO_2 or Fe_2O_3, the charge accumulation process of IrO_x was found to be efficient, both thermodynamically and kinetically.[70] This difference in the OER mechanism leads to an accumulation of reaction intermediates, which enhances the OER kinetics of IrO_x.[73–75] As charge accumulation is heavily dependent on the electronic configuration of the metal ion,[55,76] it can be expected that not only IrO_x, but other 4d/5d catalysts with low spin electronic configurations also possess an inherently efficient charge accumulation process, providing a possible explanation to the high activity of 4d/5d-rare metal catalysts in general.

In chapter 3, multi-electron transfer regulation was studied from the viewpoint of local pH and reaction environments.[77] The diminished selectivity of CO_2 reduction due to the competition with hydrogen evolution is one of the major

challenges of this field.[78,79] However, despite studies which report differences in Faradaic efficiency upon changing the pH, the pH is not an explicit parameter in the current form of the d-band theory. In particular, it does not differentiate between hydrogen evolution from water reduction $(2\,H_2O + 2\,e^- \rightarrow H_2 + 2\,OH^-)$ or proton reduction $(2\,H^+ + 2\,e^- \rightarrow H_2)$. In this chapter, the author has attempted to uncover the effect of local pH on the selectivity of CO_2 reduction by actively manipulating the proton concentration at the electrode surface using a rotating disc electrode (RDE). Based on the local pH dependence of the hydrogen evolution current, it was shown that water reduction is the major reaction pathway for hydrogen evolution even in a relatively acidic (pH 2.5) electrolyte, due to the depletion of protons from the electrode surface.[77] Furthermore, only the water reduction pathway was inhibited in the presence of CO_2. These results showcase the importance of reaction environments, because despite the smaller activation barrier and higher resistivity to inhibition, proton reduction fails to become the major reaction pathway due to local pH effects. The insight provided in this chapter is expected to promote further catalyst development for the CO_2 reduction.

In chapter 4, multi-electron transfer regulation in biological systems was studied in order to gain insight into optimization strategies which are beyond the boundaries of pure physical chemistry.[80,81] Namely, the evolutionary strategy of photosynthesis (biological OER enzyme) was studied from the viewpoint of genetic optimization[81] and photomotility.[80] By comparing the genetic structure with that of the reverse reaction (cytochrome c oxidase, ORR enzyme), the author has found that the OER enzyme has attempted to minimize the bioenergetic repair cost of enzyme repair. This suggests that instead of developing a stable oxygen evolution enzyme, Nature chose to supplement the instability of PS II by minimizing its repair cost and performing frequent repairs. This stability focused optimization was observed also at the cellular level, as *Euglena gracilis* cells

were found to preferentially orient themselves such that they were not subject to excess solar irradiation. The biological strategy of maintaining the balance between energy consumption and acquisition showcases the importance of stability in terms of multi-electron transfer regulation.

Finally, in chapter 5, an overview and perspective based on the strategies concerning multi-electron transfer catalysis presented in this thesis will be presented. Through these approaches, the author has attempted to construct a multi-dimensional understanding of multi-electron transfer regulation.

References

[1] Koper, M. T. *J. Electroanal. Chem.* **2011**, *660*, 254–260.

[2] Andréasson, L.-E.; Bränden, R.; Reinhammar, B. *Biochim. Biophys. Acta* **1976**, *438*, 370–379.

[3] Luther, G. W. *Aquat. Geochem.* **2010**, *16*, 395–420.

[4] Tributsch, H. *Phys. Status Solidi. A* **2014**, *211*, 2052–2062.

[5] Vante, N. A.; Tributsch, H. *Nature* **1986**, *323*, 431–432.

[6] Lewis, N. S.; Nocera, D. G. *Proc. Natl. Acad. Sci. U. S. A.* **2006**, *103*, 15729–15735.

[7] Fujii, K.; Nakamura, S.; Sugiyama, M.; Watanabe, K.; Bagheri, B.; Nakano, Y. *Int. J. Hyd. Energ.* **2013**, *38*, 14424–14432.

[8] Jia, J.; Seitz, L. C.; Benck, J. D.; Huo, Y.; Chen, Y.; Ng, J. W. D.; Bilir, T.; Harris, J. S.; Jaramillo, T. F. *Nat. Commun.* **2016**, *7*, 13237.

[9] Krishtalik, L. I. *Biochim. Biophys. Acta* **1986**, *849*, 162–171.

[10] Krishtalik, L. *Bioelectrochem. Bioenerg.* **1990**, *23*, 249–263.

[11] Krishtalik, L. I. *Biochim. Biophys. Acta* **1989**, *977*, 200–206.

[12] Babcock, G. T.; Wikström, M. *Nature* **1992**, *356*, 301–309.

[13] Babcock, G. T. *Proc. Natl. Acad. Sci. U. S. A.* **1999**, *96*, 12971–12973.

[14] Gnaiger, E.; Steinlechner-Maran, R.; Méndez, G.; Eberl, T.; Margreiter, R. *J. Bioenerg. Biomembr.* **1995**, *27*, 583–596.

[15] Mulo, P.; Sicora, C.; Aro, E.-M. *Cell. Mol. Life Sci.* **2009**, *66*, 3697.

[16] Cox, N.; Pantazis, D. A.; Neese, F.; Lubitz, W. *Acc. Chem. Res.* **2013**, *46*, 1588–1596.

[17] Yoshikawa, S.; Shinzawa-Itoh, K.; Nakashima, R.; yaono, R.; Yamashita, E.; Inoue, N.; Yao, M.; Fei, M. J.; Libeu, C. P.; Mizushima, T.; Yamaguchi, H.;

Tomizaki, T.; Tsukihara, T. *Science* **1998**, *280*, 1723–1729.

[18] Muradov, N. Z.; Veziroğlu, T. N. *Carbon-Neutral Fuels and Energy Carriers (Green Chemistry and Chemical Engineering)*; CRC Press, 2017.

[19] Schlögl, R. *Topics in Catalysis* **2016**, *59*, 772–786.

[20] Singh, S.; Jain, S.; Venkateswaran, P.; Tiwari, A. K.; Nouni, M. R.; Pandey, J. K.; Goel, S. *Renew. Sust. Energ. Rev.* **2015**, *51*, 623–633.

[21] Ashena, M.; Sadeghi, H.; Yavari, K.; Najarzadeh, R. *International Journal of Energy Economics and Policy* **2016**, *6*.

[22] Mohammed, Y.; Mustafa, M. W.; Bashir, N.; Ogundola, M.; Umar, U. *Renew. Sust. Energ. Rev.* **2014**, *34*, 361–370.

[23] Oyedepo, S. O. *Renew. Sust. Energ. Rev.* **2014**, *34*, 255–272.

[24] Dincer, I.; Acar, C. *Int. J. Energ. Res.* **2015**, *39*, 585–606.

[25] Joya, K. S.; de Groot, H. J. *ChemSusChem* **2014**, *7*, 73–76.

[26] Lewis, N. S. *Science* **2016**, *351*, aad1920.

[27] Hosseini, S. E.; Wahid, M. A. *Renew. Sust. Energ. Rev.* **2016**, *57*, 850–866.

[28] Lee, J.; Jeong, B.; Ocon, J. D. *Curr. Appl. Phys.* **2013**, *13*, 309–321.

[29] Zhang, F.; Zhao, P.; Niu, M.; Maddy, J. *Int. J. Hyd. Energ.* **2016**, *41*, 14535–14552.

[30] Warburg, O. *Science* **1956**, *123*, 309–314.

[31] Pelicano, H.; Xu, R.-h.; Du, M.; Feng, L.; Sasaki, R.; Carew, J. S.; Hu, Y.; Ramdas, L.; Hu, L.; Keating, M. J. *J. Cell Biol.* **2006**, *175*, 913–923.

[32] Wei, Y.-H.; Lu, C.-Y.; Wei, C.-Y.; Ma, Y.-S.; Lee, H.-C. *Chin. J. Physiol.* **2001**, *44*, 1–12.

[33] Fleming, J.; Miquel, J.; Cottrell, S.; Yengoyan, L.; Economos, A. *Gerontol.* **1982**, *28*, 44–53.

[34] Lane, N.; Martin, W. *Nature* **2010**, *467*, 929–934.

[35] Vander Heiden, M. G.; Cantley, L. C.; Thompson, C. B. *Science* **2009**, *324*, 1029–1033.

[36] Simon, H.-U.; Haj-Yehia, A.; Levi-Schaffer, F. *Apoptosis* **2000**, *5*, 415–418.

[37] Piconi, L.; Quagliaro, L.; Assaloni, R.; Da Ros, R.; Maier, A.; Zuodar, G.; Ceriello, A. *Diabetes Metab. Res. Rev.* **2006**, *22*, 198–203.

[38] Bragado, P.; Armesilla, A.; Silva, A.; Porras, A. *Apoptosis* **2007**, *12*, 1733–1742.

[39] Harman, D. *J. Gerontol.* **1968**, *23*, 476–482.

[40] Kirkwood, T. B.; Kowald, A. *BioEssays* **2012**, *34*, 692–700.

[41] Stadtman, E. R. *Science* **1992**, *257*, 1220–1224.

[42] Sabatier, P. *Ber. Dtsch. Chem. Ges* **1911**, *44*, 2001.

[43] Nørskov, J. K.; Studt, F.; Abild-Pedersen, F.; Bligaard, T. *Fundamental Concepts in Heterogeneous Catalysis*; John Wiley and Sons, 2014.

[44] Vojvodic, A.; Nørskov, J. K. *Natl. Sci. Rev.* **2015**, *2*, 140–143.

[45] Man, I. C.; Su, H.-Y.; Calle-Vallejo, F.; Hansen, H. A.; Martínez, J. I.; Inoglu, N. G.; Kitchin, J.; Jaramillo, T. F.; Nørskov, J. K.; Rossmeisl, J. *ChemCatChem* **2011**, *3*, 1159–1165.

[46] Rossmeisl, J.; Logadottir, A.; Nørskov, J. K. *Chem. Phys.* **2005**, *319*, 178–184.

[47] Kjaergaard, C. H.; Rossmeisl, J.; Nørskov, J. K. *Inorg. Chem.* **2010**, *49*, 3567–3572.

[48] Halck, N. B.; Petrykin, V.; Krtil, P.; Rossmeisl, J. *Phys. Chem. Chem. Phys.* **2014**, *16*, 13682–13688.

[49] Dickens, C. F.; Nørskov, J. K. *J. Phys. Chem. C* **2017**, *121*, 18516–18524.

[50] Gauthier, J. A.; Dickens, C. F.; Chen, L. D.; Doyle, A. D.; Nørskov, J. K. *J. Phys. Chem. C* **2017**, *121*, 11455–11463.

[51] Lu, Z.; Chen, G.; Li, Y.; Wang, H.; Xie, J.; Liao, L.; Liu, C.; Liu, Y.; Wu, T.; Li, Y.; Luntz, A. C.; Bajdich, M.; Cui, Y. *J. Am. Chem. Soc.* **2017**, *139*, 6270–6276.

[52] Li, H.; Li, Y.; Koper, M. T.; Calle-Vallejo, F. *J. Am. Chem. Soc.* **2014**, *136*,

15694–15701.

[53] Diaz-Morales, O.; Ledezma-Yanez, I.; Koper, M. T.; Calle-Vallejo, F. **2015**,

[54] Rossmeisl, J.; Qu, Z.-W.; Zhu, H.; Kroes, G.-J.; Nørskov, J. K. *J. Electroanal. Chem.* **2007**, *607*, 83–89.

[55] Takashima, T.; Hashimoto, K.; Nakamura, R. *J. Am. Chem. Soc.* **2012**, *134*, 1519–1527.

[56] Ooka, H.; Takashima, T.; Yamaguchi, A.; Hayashi, T.; Nakamura, R. *Chem. Commun.* **2017**, *53*, 7149–7161.

[57] Huynh, M.; Bediako, D. K.; Liu, Y.; Nocera, D. G. *J. Phys. Chem. C* **2014**, *118*, 17142–17152.

[58] Koper, M. T. *Top. Catal.* **2015**, *58*, 1153–1158.

[59] Suntivich, J.; Gasteiger, H. A.; Yabuuchi, N.; Nakanishi, H.; Goodenough, J. B.; Shao-Horn, Y. *Nat. Chem.* **2011**, *3*, 546–550.

[60] Suntivich, J.; May, K. J.; Gasteiger, H. A.; Goodenough, J. B.; Shao-Horn, Y. *Science* **2011**, *334*, 1383–1385.

[61] Hong, X.; Chan, K.; Tsai, C.; Nørskov, J. K. *ACS Catalysis* **2016**, *6*, 4428–4437.

[62] Hong, X.; Chan, K.; Tsai, C.; Nørskov, J. K. *ACS Catal.* **2016**, *6*, 4428–4437.

[63] Montoya, J. H.; Tsai, C.; Vojvodic, A.; Nørskov, J. K. *ChemSusChem* **2015**, *8*, 2180–2186.

[64] Calle-Vallejo, F.; Martinez, J.; García-Lastra, J. M.; Rossmeisl, J.; Koper, M. *Phys. Rev. Lett.* **2012**, *108*, 116103.

[65] Hessels, J.; Detz, R. J.; Koper, M.; Reek, J. N. *Chem. Eur. J.* **2017**,

[66] Hinnemann, B.; Moses, P. G.; Bonde, J.; Jørgensen, K. P.; Nielsen, J. H.; Horch, S.; Chorkendorff, I.; Nørskov, J. K. *J. Am. Chem. Soc.* **2005**, *127*, 5308–5309.

[67] Umena, Y.; Kawakami, K.; Shen, J.-R.; Kamiya, N. *Nature* **2011**, *473*, 55–60.

[68] Suga, M.; Akita, F.; Hirata, K.; Ueno, G.; Murakami, H.; Nakajima, Y.; Shimizu, T.; Yamashita, K.; Yamamoto, M.; Ago, H.; Shen, J.-R. *Nature* **2015**, *517*, 99–103.

[69] Ooka, H.; Wang, Y.; Yamaguchi, A.; Hatakeyama, M.; Nakamura, S.; Hashimoto, K.; Nakamura, R. *Phys. Chem. Chem. Phys.* **2016**, *18*, 15199–15204.

[70] Ooka, H.; Yamaguchi, A.; Takashima, T.; Hashimoto, K.; Nakamura, R. *J. Phys. Chem. C* **2017**, *121*, 17873–17881.

[71] Zhao, Y.; Vargas-Barbosa, N. M.; Hernandez-Pagan, E. A.; Mallouk, T. E. *Small* **2011**, *7*, 2087–2093.

[72] Seitz, L. C.; Dickens, C. F.; Nishio, K.; Hikita, Y.; Montoya, J.; Doyle, A.; Kirk, C.; Vojvodic, A.; Hwang, H. Y.; Norskov, J. K.; Jaramillo, T. F. *Science* **2016**, *353*, 1011–1014.

[73] Le Formal, F.; Pastor, E.; Tilley, S. D.; Mesa, C. A.; Pendlebury, S. R.; Grätzel, M.; Durrant, J. R. *J. Am. Chem. Soc.* **2015**, *137*, 6629–6637.

[74] Kucernak, A. R.; Zalitis, C. *J. Phys. Chem. C* **2016**, *120*, 10721–10745.

[75] Conway, B.; Tilak, B. *Electrochim. Acta* **2002**, *47*, 3571–3594.

[76] Mazin, I.; Khomskii, D.; Lengsdorf, R.; Alonso, J.; Marshall, W.; Ibberson, R.; Podlesnyak, A.; Martinez-Lope, M.; Abd-Elmeguid, M. *Phys. Rev. Lett.* **2007**, *98*, 176406.

[77] Ooka, H.; Figueiredo, M. C.; Koper, M. T. *Langmuir* **2017**, *33*, 9307–9313.

[78] Kortlever, R.; Shen, J.; Schouten, K. J. P.; Calle-Vallejo, F.; Koper, M. T. *J. Phys. Chem. Lett.* **2015**, *6*, 4073–4082.

[79] Zhang, Y.-J.; Sethuraman, V.; Michalsky, R.; Peterson, A. A. *ACS Catal.* **2014**, *4*, 3742–3748.

[80] Ooka, H.; Ishii, T.; Hashimoto, K.; Nakamura, R. *RSC Adv.* **2014**, *4*, 20693–20698.

[81] Ooka, H.; Hashimoto, K.; Nakamura, R. *submitted to Mol. Inform.*

Chapter 2

Element Strategy of Multi-Electron Transfer

2.1 Introduction

2.1.1 Overview of This Chapter

In this chapter, the author has attempted to understand the multi-electron transfer from the viewpoint of valence change and charge accumulation.[1–3] It is widely recognized that biological enzymes utilize 3d-metal elements such as Mn,[4–6] Fe,[7,8] Co,[9–12] Ni,[13–15] and Cu[8,16,17] to catalyze multi-electron transfer reactions efficiently. However, despite extensive studies to increase the activity of artificial 3d-metal catalysts, the most active manmade catalysts are those based on 4d/5d-rare metals, such as Ru[18–20] or Ir (oxygen evolution),[21–25] Pt (hydrogen evolution or oxygen reduction),[26–29] and Au[30–32] or Ag[31,33] (CO_2 reduction). In order to elucidate the difference between 3d-metals and 4d/5d rare metal catalysts, the author has studied the oxygen evolution mechanism of amorphous Ir oxide (IrO_x) from the viewpoint of valence change and charge accumulation. The charge accumulation process has been observed in both enzymatic[4–6,34–36] and artificial systems, and it has even been reported to be rate-limiting in some cases, such as MnO_2[37,38] or Fe_2O_3.[39,40] Despite its evident importance, however, charge accumulation remains an under-evaluated process in the presiding theory of multi-electron transfer (d-band theory), which places emphasis on the interaction between the substrate and the catalyst.[41] Therefore, a mechanistic study on the charge accumulation efficiency of IrO_x, and a mechanistic comparison between 3d-metal catalysts (MnO_2 and Fe_2O_3) and 4d/5d metals (IrO_x) is expected to yield insight into the element strategy of multi-electron transfer catalysis.

2.1.2 Element Strategy and Oxygen Evolution Catalysis

The oxygen evolution reaction $(2\,H_2O \rightarrow O_2 + 4\,H^+ + 4\,e^-$, OER) is currently under intense investigation[21,42–45] as a possible method to enhance the sustainability of human society. The electrons and protons liberated from water can be utilized to drive a reduction half-reaction such as hydrogen evolution $(2\,H_2O + 2\,e^- \rightarrow H_2 + 2\,OH^-)$[27,46] or CO_2 reduction (for example, $CO_2 + 8\,e^- + 8\,H^+ \rightarrow CH_4$),[47–51] providing an environmentally-friendly way of generating chemical fuels. Therefore, coupling these electrochemical reactions with renewable electricity provides a means to remedy the temporal fluctuation of sustainable energy sources. The strategy of alleviating the intermittency of renewable energy by generating chemical fuels *via* the OER is chemically equivalent to the energy strategy of biological photosynthesis,[5] and is expected to greatly facilitate the handling of environmentally-friendly energy sources (Figure 1.1).[52] In order to compose a sustainable energy cycle such as that found in Nature, it is necessary to develop robust and efficient OER catalysts.

There are currently several groups of materials which are known to possess high OER activity. One example is amorphous Ir oxide (IrO_x) and other Ir oxides, which are robust under anodic conditions and are known to maintain activity across a wide range of pH.[21–25] Several studies have also attempted to synthesize mixed oxides with Ru,[53–55] due to the slightly lower overpotential of RuO_2.[18–20] Regardless of the exact composition, however, the scarcity and high costs associated with 4d/5d elements such as Ru and Ir impose limitations to the large-scale applicability of rare metal catalysts.[56] Therefore, it is highly desirable to substitute the rare metal catalysts with those derived from earth-abundant 3d-metals.

So far, however, this has proven to be a significant scientific challenge, due to the large overpotentials and low stability of 3d-metal catalysts. The majority of 3d metal oxides[57,57,58] such as MnO_2,[37,38] NiO_2,[44] Co_3O_4,[59] and Fe_2O_3[39,40] operate most efficiently under alkaline conditions. With few exceptions,[42,60–62] both their activity and stability deteriorate in acidic and neutral pH. Although NiFe catalysts have already seen industrial use in the field of alkaline electrolysis, the pH dependence of 3d-metal catalysts hinders their applicability for polymer electrolyte membrane (PEM) electrolyzers, due to the acidic environment at the vicinity of the electrode. As the high conductivity of the charge carrier (H^+) is one of the major benefits of the PEM system, high activity and stability at acidic pH is a requirement towards successful implementation in PEM electrolyzers.[63–65] On a more general note, the efficiency at acidic pH is a fundamental chemical parameter for evaluating anode materials, because the local pH at the anode is expected to decrease during electrolysis.[66–68] As will be explained in detail in Chapter 3, the local pH at the electrode is dictated by the consumption and generation of H^+ and OH^-.[69] Although the presence of buffer molecules may provide an additional flux for H^+ diffusion (consumption), the local pH at the electrode will acidify if the rate of H^+ generation, *i.e.*, the rate of OER, is sufficiently large. Therefore, in order to develop 3d-metal OER catalysts as substitutes for 4d/5d-metals such as Ru or Ir, it is critical to increase their activity, especially in low pH regions.

2.1.3 Current Efforts to Increase the Activity of 3d-Metal Catalysts

Currently, the properties of electrocatalysts are often rationalized based on the d-band theory and the computational hydrogen electrode (CHE) model.[41,45,70–73] As stated in detail in Chapter 1, the d-band theory is at its heart a quantitative extension of the Sabatier principle, which predicts that the existence of an optimum binding energy for each reaction intermediate. If the binding energy is too small, the catalyst will not interact sufficiently with the reactant, while binding interactions which are too strong would hinder the ability of the intermediate to either desorb or react further, effectively "poisoning" the catalyst. There have been numerous studies which have reported an increase of the OER activity by optimizing the binding energy of a specific intermediate, showcasing the benefits of having a single physicochemical parameter (binding energy) as a descriptor to map the chemical space composed of various materials.

However, there are limitations to the current state of the d-band theory. For example, Man *et al.* have predicted the OER activity of various oxide materials based on the binding energy between the metal and oxygen (Figure 2.1).[45] This study is based on the assumption that OER proceeds *via* the acid–base mechanism, which is one of the two commonly proposed OER mechanisms (Figure 2.2A).

$$H_2O \text{ (liq.)} + M \rightarrow M{-}OH + H^+ + e^- \tag{2.1}$$

$$M{-}OH \rightarrow M{=}O + H^+ + e^- \tag{2.2}$$

$$M{=}O + H_2O \rightarrow M{-}OOH + H^+ + e^- \tag{2.3}$$

$$M{-}OOH \rightarrow O_2 + H^+ + e^- + M \tag{2.4}$$
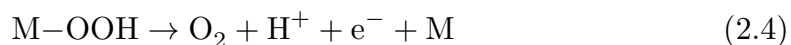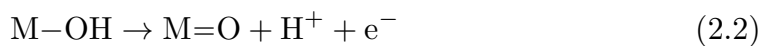
Interestingly, however, only a *ca.* 0.1 V difference in activity could be found between MnO_2 and IrO_x (Figure 2.1). This is in stark contrast to the 500-mV difference in overpotential found in neutral electrolytes ($6 < \text{pH} < 8$).
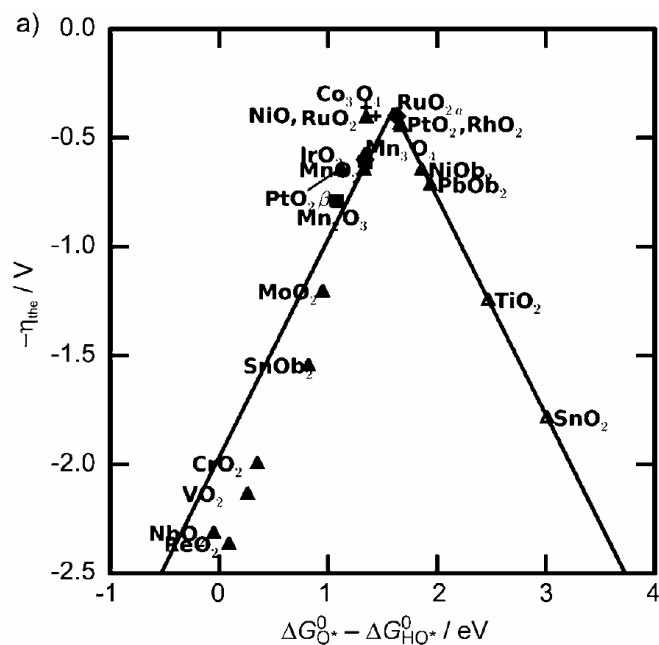
Fig. 2.1 The OER activity of oxide catalysts predicted computationally based on the acid–base mechanism. Reproduced from ref. 45 with permission from Wiley.

(A) Acid-Base Mechanism
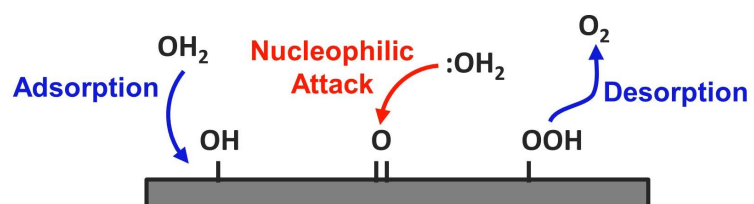
(B) Direct-Coupling Mechanism
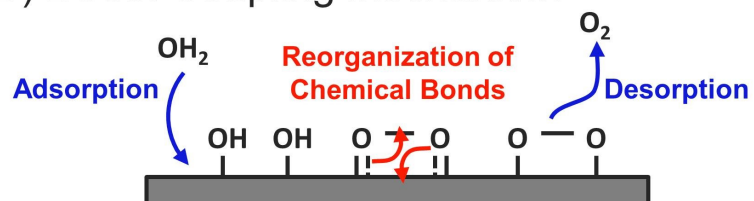
Fig. 2.2   Schematic representation of the acid–base mechanism (A) and the direct–coupling mechanism (B).

On the other hand, Busch *et al.*[74] have calculated the overpotential between MnO_2 and IrO_x assuming a direct–coupling mechanism (Figure 2.2B). The main difference between the two OER mechanisms is in how the chemical bond between two oxygen atoms will be formed. In contrast to the acid–base mechanism in which a water molecule or hydroxyl ion initiates a nucleophilic attack on a surface adsorbed oxygen species, in the case of a direct–coupling mechanism, two adjacent oxygen species will rearrange their chemical bonds to result in an O–O bond:

$$2\,H_2O + (\text{liq.}) \,+\, 2M \rightarrow 2\text{M-OH} + 2\,H^+ + 2\,e^- \qquad (2.5)$$

$$2\,M{-}OH \rightarrow 2M{=}O + 2\,H^+ + 2\,e^- \qquad (2.6)$$

$$2M{=}O \rightarrow M{-}O{-}O{-}M \qquad (2.7)$$

$$M{-}O{-}O{-}M \rightarrow O_2(\text{gas}) + 2\,M \qquad (2.8)$$
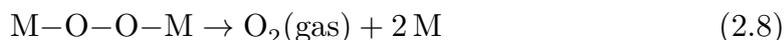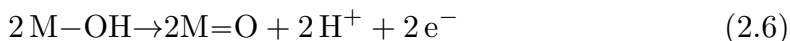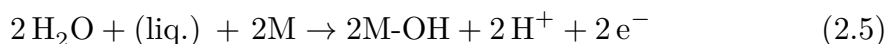
However, also in this case, only a 0.02 V (Figure 2.3) difference in the overpotential between IrO_x and MnO_2 could be found. The fact that two independent studies[45,74] which have assumed different OER mechanisms still could not explain the difference between these materials indicates that key aspects of catalysis remain unresolved, especially because the experimentally observed overpotential difference of *ca.* 500 mV is greater than typical density functional theory (DFT) errors.[75]
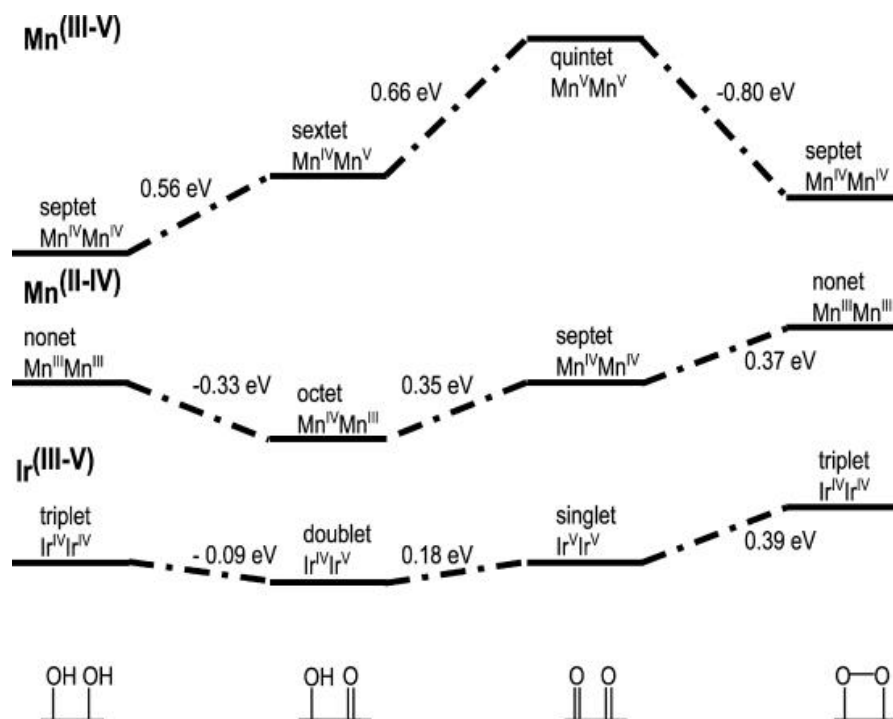
Fig. 2.3 The OER activity of oxide catalysts predicted computationally based on the direct–coupling mechanism. Reproduced with permission from ref. 74. Copyright (2013) American Chemical Society.

2.1.4 Valence Change and Charge Accumulation

One origin of the discrepancy between theory and experiment may be because the Sabatier principle focuses extensively on the interaction between the substrate and the catalyst.[41] Although these interactions have proven useful to predict the barriers of bond formation and dissociation, in the case of multi-electron transfer catalysis, multiple charges must be stored prior to the reorganization of chemical bonds.[37] This charge accumulation process can be considered a general phenomenon in multi-electron transfer, as the valence change of a metal ion has been observed for a variety of catalytic sites in both artificial and enzymatic systems. For example, the active site of the biological OER enzyme, photosystem II (PS II), possesses four Mn ions.[4,76] Based on extensive *in-situ* spectroscopic evidence, it is now widely recognized that these Mn ions are oxidized from Mn^{3+} to Mn^{4+} in a successive manner during catalysis, which would allow the active site to accumulate the four charges necessary for the four-electron oxidation of water.[*1] The valence change of metal ions during enzyme turnover is also well documented for other multi-electron transfer enzymes such as hydrogenases, nitrogenases, RubisCO, and nitrate reductases, as well as for artificial electrocatalysts such as MnO_2,[37,38] Fe_2O_3,[39,40] and Molybdenum oxo-sulfides.[77] Furthermore, in some 3d-metal catalysts such as MnO_2[37,38,78] or Fe_2O_3,[39,40] the charge accumulation process has been reported to dictate the OER activity based on *in-situ* spectroelectrochemistry. These observations suggest charge accumulation is a fundamentally important process during electrocatalysis, and therefore, studying multi-electron transfer reactions not only based on binding energies, but also from the viewpoint of valence change is important to rationalize the differences in activity between different materials.

[*1] Although the accumulation of the first three charges is well-documented, there is still dispute on the existence of the fourth Mn^{4+}. For details, see references 4,34–36.

2.2 Objective

The objective of the study in chapter 2 is to understand the role of valence change and charge accumulation on the efficiency of multi-electron transfer reactions. Especially in light of the fact that only negligible differences in binding energies were observed between MnO_2 and IrO_x, the author has hypothesized that the critical mechanistic difference between MnO_2 and IrO_x lies not in the kinetics of bond formation, but in the kinetics of charge accumulation.[1-3] To this end, the OER mechanism of IrO_x was studied from the viewpoint of charge accumulation using *in-situ* evanescent wave spectroscopy. By monitoring the d-d transition of Ir in an *in-situ* manner, the valence change of Ir during OER could be observed directly. The surface sensitivity and the temporal resolution of this technique yield insight into the kinetics of valence change, which is beneficial in order to conduct intermediate scavenger experiments. By studying the mechanistic difference of MnO_2 and IrO_x which leads to the difference in OER activity, the author has attempted to gain insight into the critical difference between the abundant 3d-metals and the highly active 4d/5d rare-metal catalysts (Figure 2.4).
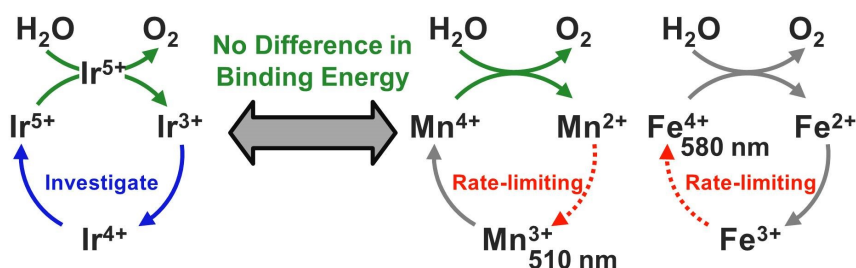
Fig. 2.4 Strategy of chapter 2. The charge accumulation process was found to be rate-limiting on MnO_2[37,38,78] and Fe_2O_3[39,40] based on *in-situ* spectroelectrochemistry. Therefore, by studying the OER mechanism from the viewpoint of charge accumulation, the author has attempted to gain insight into the critical difference between the abundant 3d-metals and the highly active 4d/5d rare-metal catalysts.

2.3   Materials and Methods

2.3.1   Fabrication of IrO$_x$ Electrodes

IrO$_x$ electrodes were fabricated as previously reported.[21] First, NaOH was dissolved into 50-mL of MilliQ water to reach a pH of 12.1. The addition of 0.1 mmol K$_2$IrCl$_6$ (48.3 mg) to the alkaline solution yielded an opaque brown solution. The mixture was then heated from room temperature at a rate of 3 °C/min to 70 °C under constant stirring using a hot plate held at 80 °C. The solution was lifted from the hot plate as necessary to adjust the rate of heating. Upon reaching 70 °C, the resulting solution was cooled immediately in an ice bath, during which the pH of the solution increased from 8.81 to 9.5. A time record of the pH, temperature, and solution color can be found in Table 2.1, and the UV–Vis spectrum of the obtained solution can be found in Figure 2.5. However, although the UV–Vis spectrum was similar to that of the original report,,[21] the pH of the solution was outside the range reported to yield a stable IrO$_x$ film ($8 <$ pH < 9). Adjusting the pH of the solution by adding NaOH or HCl resulted in the formation of Ir^{4+} oxides as can be seen from the broad visible peak at $\lambda > 500$ nm, and was not pursued further. The cooled solution was stored at 4°C in the dark and was kept as the Ir stock solution. After diluting the stock solution to 1/10th in 3 M NaCl, IrO$_x$ was electrodeposited on indium tin oxide (ITO) and fluorine-doped tin oxide (FTO) substrates under galvanostatic conditions (25 μA cm^{-2}, 60 seconds). The evanescent wave spectra obtained during the electrodeposition process indicate the deposition of an Ir^{4+} oxide, as can be seen in the broad absorption maxima at *ca.* 550 nm (Figure 2.6). As the effect of temperature on the electrodeposition of IrO$_x$ has previously been documented,[79] the electrodeposition solution was allowed to equilibrate to room temperature before fabrication of the IrO$_x$ electrodes.

Table 2.1 Record of pH, color, and temperature during the hydrolysis of K_2IrCl_6.

Time/min	pH	Temperature/°C	color
0	25.2	12.12	Brown
1	28.0	11.97	
2	31.2	11.89	
3	34.2	11.63	
4	37.0	11.76	
5	39.3	11.72	
6	42.5	11.66	
7	46.0	11.59	
8	49.1	11.53	Golden yellow
9	53.1	11.49	
10	54.0	11.41	
11	58.6	10.99	Lemon yellow
12	60.5	10.51	
13	64.0	10.02	Cloudy yellow
14	67.0	9.32	
15	70.0	8.81	Cloudy blue
16	16.0	9.50	Cloudy blue
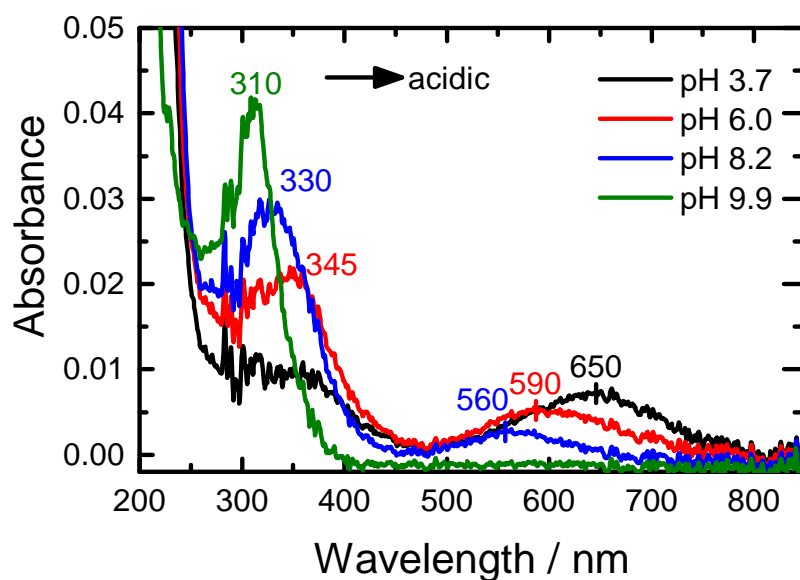
Fig. 2.5 UV–Vis spectra of the IrO_x stock solution at various pH. The absorption at $\lambda > 500$ nm found at acidic pH is assignable to the formation of Ir^{4+}–oxides.
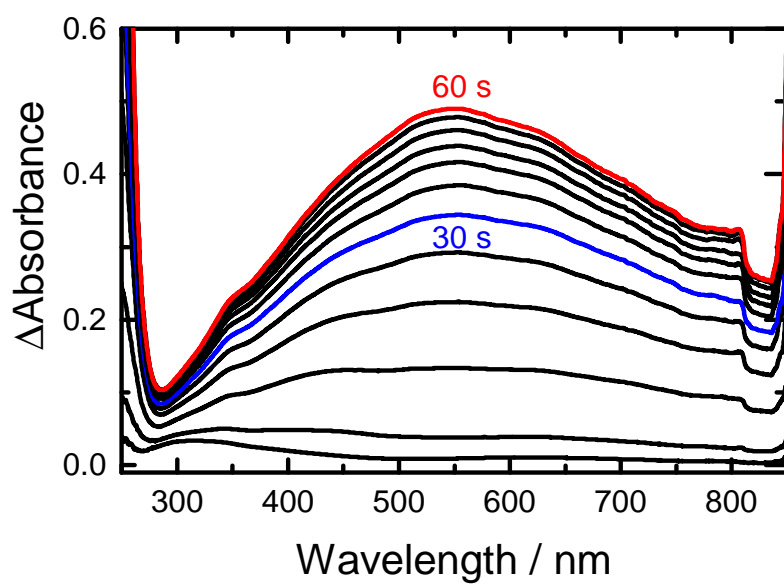
Fig. 2.6 The evanescent wave spectra obtained during the electrodeposition of the IrO$_x$ film. The broad absorption at *ca.* 550 nm is a characteristic of Ir^{4+}–oxides.

2.3.2 *In-Situ* Evanescent Wave Spectroscopy

A surface and interface spectrometer system (SIS5000, System Instruments) combined with a custom-made three-electrode electrochemical cell was used for the *in-situ* evanescent wave spectroscopy measurements (Figure 2.7). An ITO-coated optical waveguide (quartz, refraction index = 1.47) was placed underneath the electrochemical reactor. The IrO_x film was electrodeposited directly on top of the ITO of the optical waveguide, which serves as an internal multiple reflection element necessary to generate an evanescent wave at the interface between the working electrode and the electrolyte. The incident light from the 150-watt xenon lamp was inclined at an angle of *ca.* 3 ° parallel to the surface of the ITO substrate.
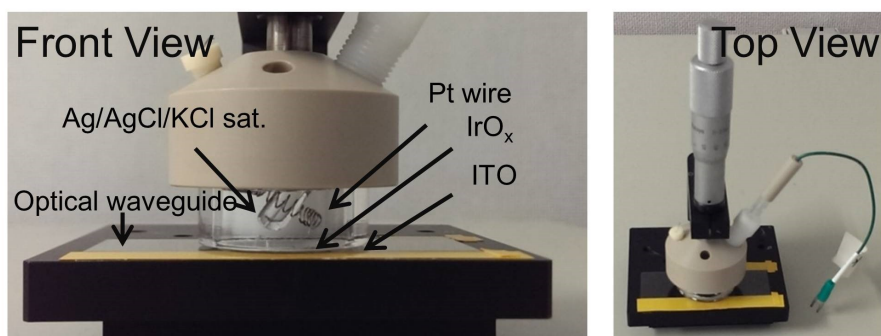
Fig. 2.7 Experimental setup for the evanescent wave spectroscopy measurements.

2.3.3   Inlet Electrochemical Mass Spectroscopy

In order to confirm the evolution of oxygen *in-situ* during intermediate scavenger (H_2O_2 addition) experiments, a quadrupole mass spectrometer (QMS, Pfeiffer Vacuum QMG220M1) was connected to the electrochemical reactor using a similar setup to the differential electrochemical mass spectrometer (DEMS).[80–84] Briefly, the vacuum chamber of the mass spectrometer is connected to the electrolyte with a stainless capillary which is covered with a microporous polytetrafluoroethylene (PTFE) membrane. This setup allows gaseous molecules within the electrolyte to diffuse into the vacuum chamber of the mass spectrometer, allowing real-time sampling of the gas products (time lag < 2 minutes). The gas-tight electrochemical chamber was bubbled with argon gas for 30 minutes prior to each measurement.

2.3.4   Electrochemistry

The electrolyte was prepared by first adding the components of Britton-Robinson Buffer (0.4 M each of phosphate, borate, and acetate) to a 0.5 M Na_2SO_4 solution, and then adjusting the pH to the desired value by addition of H_2SO_4 or NaOH. In the case of unbuffered solutions, pH was adjusted by adding H_2SO_4 or NaOH directly to the 0.5 M Na_2SO_4 solution. All glassware were sonicated in ultrapure water directly before measurements. A platinum wire and an Ag/AgCl/KCl (saturated) electrode were used as the counter and reference electrodes, respectively for all measurements. All electrochemical potentials have been converted into the standard and reversible hydrogen electrode scales (SHE and RHE, respectively) after measurements. An automatic polarization system (HZ-5000, Hokuto-Denko) was used as the potentiostat. An Excel spreadsheet was used to calculate the rate constants of E_1 and E_2. The slopes v_a and v_c were evaluated from the peak positions in the cyclic voltammograms where the scan rate was 10 V/s to 100 V/s for E_1, and from 10 V/s to 50 V/s for E_2.

2.3.5 Computation

Gaussian 09 packages[85] were used for modeling the UV–Vis spectra of binuclear IrO_x clusters. The B3LYP (Becke, 3-parameter, Lee–Yang–Parr) exchange-correlation functional, was chosen for calculation, due to the successful implementation of a previous study on IrO_x clusters.[86] Ir atoms were calculated using the LANL2DZ basis set, whereas the 6-311++G(d,p) basis set was adopted for other atoms. The geometries of the binuclear Ir cluster were optimized at the unrestricted B3LYP level after examining low, intermediate and high spin states, with and without symmetry constraints. A binuclear Ir oxide cluster was chosen in order to represent the hydrated nature of IrO_x, which displays markedly superior activity compared to its rutile counterpart. A mononuclear Ir oxide cluster was unable to reproduce the experimentally obtained spectra. The absorption spectra of the obtained geometries were calculated using time-dependent DFT (TDDFT).[87] 40 states were solved in TDDFT calculations.

2.4 Results and Discussion

2.4.1 Redox Potentials and Kinetics of Charge Accumulation

Figure 2.8 shows the cyclic voltammograms of IrO_x in a buffered 0.5 M Na_2SO_4 electrolyte at various pH. The voltammogramss show typical redox behavior of hydrous IrO_x films and are in agreement with previous reports.[21,23,88,89] Namely, the redox transition from Ir^{3+} to Ir^{4+} (E_1) can clearly be seen from pH 2-12, while that of Ir^{4+} to Ir^{5+} (E_2) becomes more obvious at alkaline pH[*2]. E_1 and E_2 shift with a pH dependence of *ca.* 30 mV/pH on the RHE scale (Figure 2.9, green and blue symbols), which is in accord with the "super-Nernstian" behavior reported by Steegstra *et al.*[89] On the other hand, the onset potential of OER, defined by the potential where the current density exceeds 10 $\mu A\ cm^{-2}$ remained relatively constant across the pH range from 2 to 12 (Figure 2.9, black squares). Although the high activity of IrO_x towards OER in a wide range of pH has been documented previously,[21,89] this pH dependence (0 mV/pH with respect to the RHE scale) is in stark contrast to the pH dependence of MnO_2[37,78] and Fe_2O_3[39,40] ($>$ 0 mV/pH at neutral and acidic pH, $<$ 0 mV/pH at alkaline pH). It should also be noted that the clear voltammetric peaks (E_1 and E_2) before the onset of OER, along with the difference in pH dependence between the onset of OER and the redox potentials for valence change, suggest that redox transitions of Ir ions are not involved in the rate-limiting step of OER.

[*2] The assignment of the redox peaks in the literature is also confirmed by the *in-situ* evanescent wave measurement results shown in Figure 2.15.
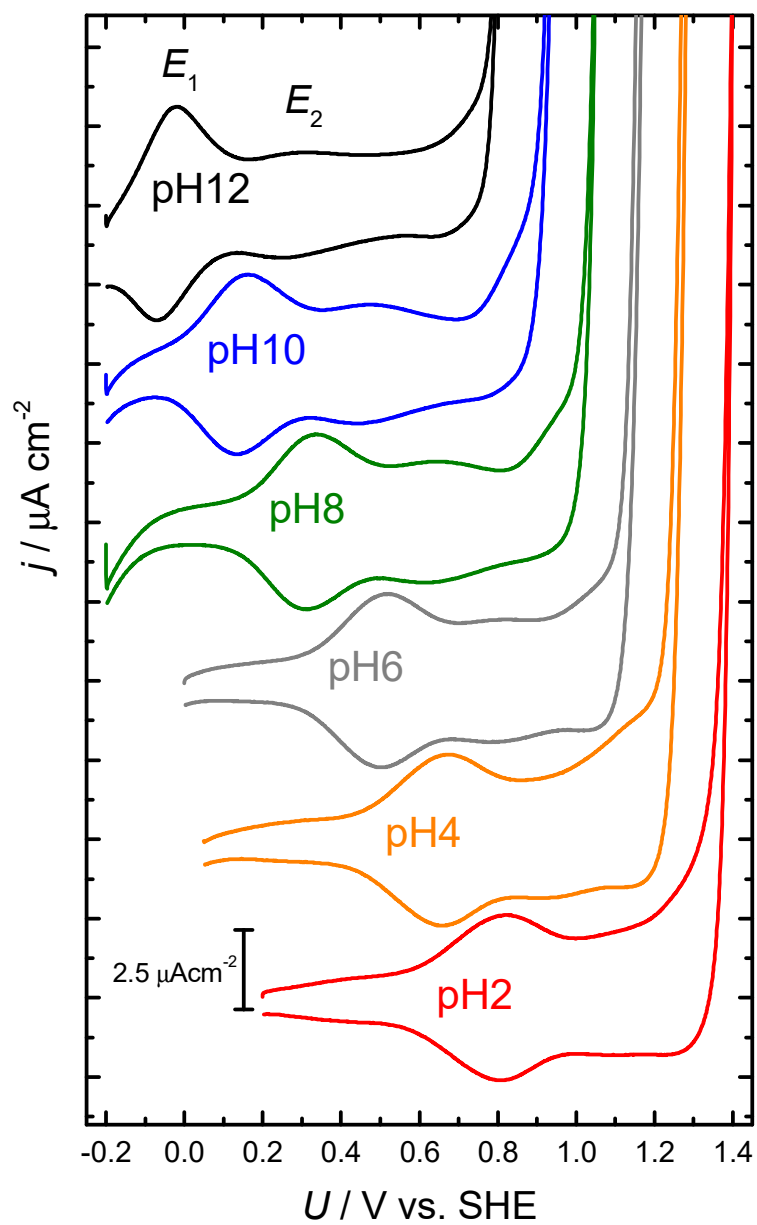
Fig. 2.8 Cyclic voltammograms of the IrO_x electrode obtained in a buffered 0.5 M Na_2SO_4 electrolyte. Each voltammogram has been offset by 5 μA cm^{-2}, and the potentials are referenced versus the SHE. Scan rate: 10 mV/s.
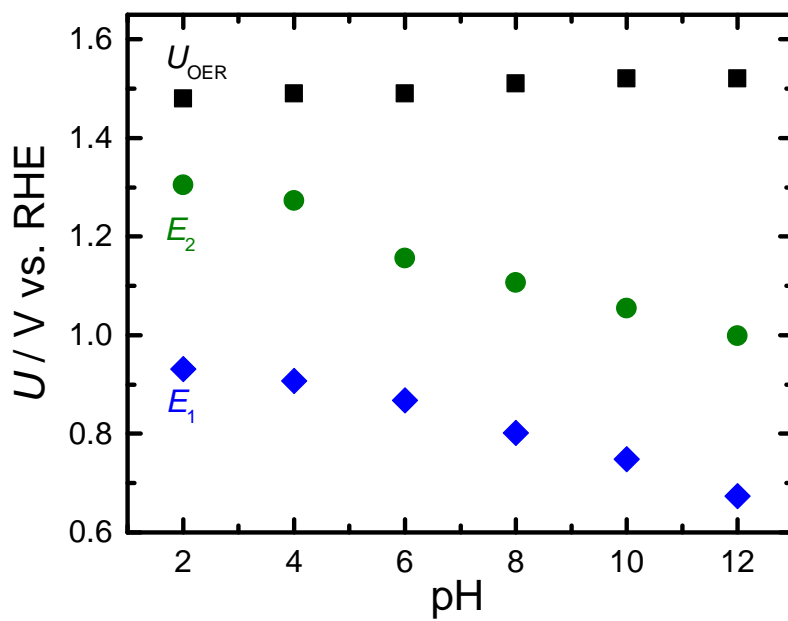
Fig. 2.9 Onset potential of OER (U_{OER}), E_1 ($\mathrm{Ir}^{3+} \to \mathrm{Ir}^{4+}$, blue), and E_2 ($\mathrm{Ir}^{4+} \to \mathrm{Ir}^{5+}$, green). U_{OER} was defined as the potential where the OER current exceeded 10 $\mu\mathrm{A}\ \mathrm{cm}^{-2}$.

In order to obtain evidence that the valence state change of Ir ions is not rate-limiting, the standard rate constants[*3] of E_1, E_2, and OER were obtained using trumpet plots and Tafel plots. The trumpet plots used to evaluate the rate constants of E_1 and E_2 are shown in Figures 2.10 and 2.11, respectively. The raw voltammograms for the trumpet plots are shown in Figure 2.12. In all cases, the separation of the anodic peak potential with the cathodic peak potential can be observed upon increasing the potential scan rate above 10 V/s. The rate constants can be obtained by applying Laviron's theory of diffusionless electrochemical systems. [90]

Namely, in the case of a diffusionless electrochemical system, the standard rate constant k can be evaluated from the following equation:

$$k = \frac{\alpha n F v_c}{RT} = \frac{(1-\alpha) n F v_a}{RT} \tag{2.9}$$

where R stands for the gas constant, T for absolute temperature, α the electron transfer coefficient, n for the number of electrons transferred, and v_a and v_c for the anodic and cathodic slopes of the trumpet plot, respectively. The value of α can be calculated from the trumpet plot using:

$$\frac{\alpha}{1-\alpha} = \frac{v_a}{v_c} \tag{2.10}$$

The results based on the analysis of trumpet plots are shown in Tables 2.2 and 2.3. The raw voltammograms are shown in Figure 2.12. Regardless of pH, the rate constants for the two redox transitions (E_1 and E_2) were found to be in the order of 1/s.

[*3] Rate constants at zero overpotential
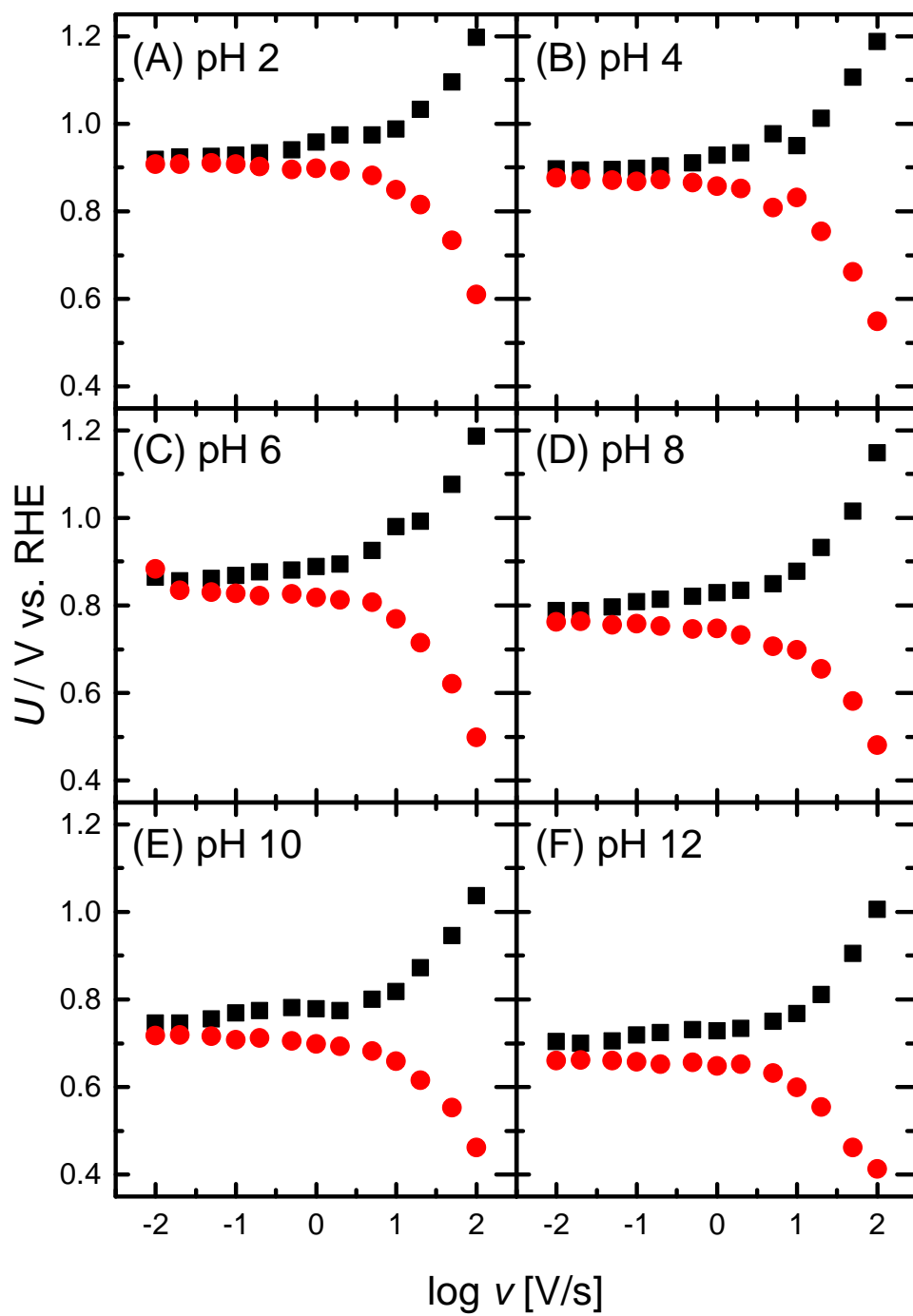
Fig. 2.10 Scan rate dependence of E_1 at pH 2 (A), 4 (B), 6 (C), 8 (D), 10 (E), and 12 (F).

43
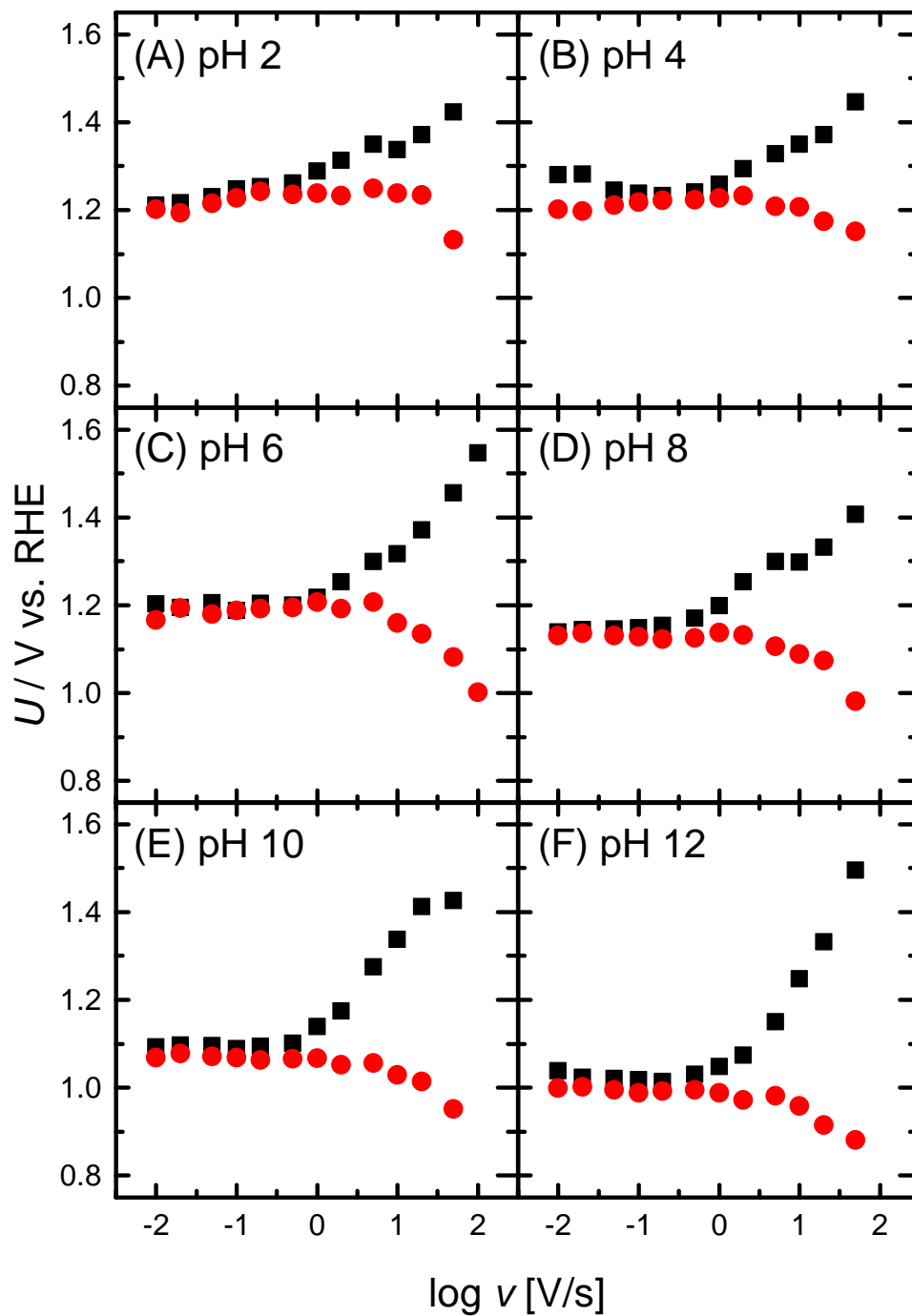
Fig. 2.11 Scan rate dependence of E_2 at pH 2 (A), 4 (B), 6 (C), 8 (D), 10 (E), and 12 (F).
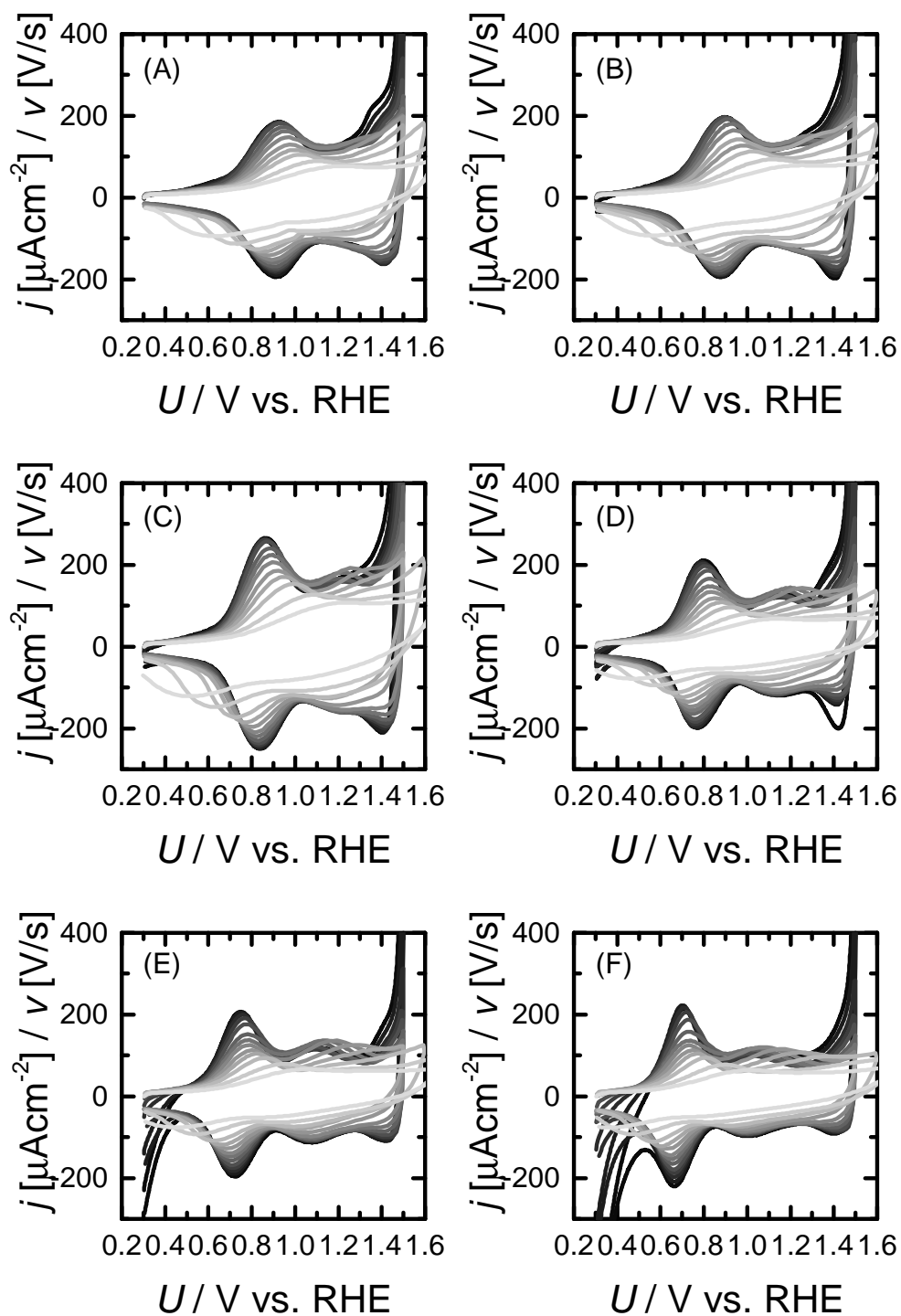
Fig. 2.12 Cyclic voltammograms of IrO$_x$ measured at different scan rates in pH 2 (A), 4 (B), 6 (C), 8 (D), 10 (E), and 12 (F). The peak positions of E_1 and E_2 obtained from these voltammograms were used to construct the trumpet plots shown in Figures 2.10 and 2.11.

Table 2.2   Results obtained from the trumpet plot analysis of E_1.

pH	v_a [V/log(V/s)][a]	v_c [V/log(V/s)][b]	α[c]	k [1/s][d]
2	0.203	0.235	0.464	4.21
4	0.237	0.276	0.462	4.94
6	0.207	0.267	0.438	4.50
8	0.263	0.213	0.552	4.55
10	0.215	0.192	0.528	3.93
12	0.238	0.192	0.553	4.11

[a] Slope of the anodic peak in the trumpet plot (Figure 2.10).
[b] Slope of the cathodic peak in the trumpet plot (Figure 2.10).
[c] Electron transfer coefficient.
[d] Rate constant of redox transition between Ir^{3+} and Ir^{4+}.

Table 2.3   Results obtained from the trumpet plot analysis of E_2.

pH	v_a [V/log(V/s)][a]	v_c [V/log(V/s)][b]	α[c]	k [1/s][d]
2	0.124	0.153	0.447	2.65
4	0.140	0.077	0.653	1.92
6	0.198	0.111	0.639	2.76
8	0.157	0.158	0.498	3.05
10	0.122	0.114	0.517	2.27
12	0.357	0.109	0.766	3.24

[a] Slope of the anodic peak in the trumpet plot (Figure 2.11).
[b] Slope of the cathodic peak in the trumpet plot (Figure 2.11).
[c] Electron transfer coefficient.
[d] Rate constant of redox transition between Ir^{4+} and Ir^{5+}.

In order to compare the kinetics of valence change with that of OER, the rate constant of OER was evaluated using Tafel plots. Figure 2.13 shows the Tafel plots of IrO_x from pH 2 to 12. The parameters obtained from the Tafel plot, such as the Tafel slope ($\frac{\partial U}{\partial \log|j|}$), exchange current density, Ir coverage, and rate constants are summarized in Table 2.4.

At all pH, the rate constant for OER was found to be several orders of magnitude smaller than that of E_1 and E_2. Although the calculation of rate constants was based on the assumption that all electrochemically active sites are active for the OER (acid–base mechanism), a decrease of active sites by half due to the occurrence of a direct–coupling mechanism does not change the fact that the OER rate constant is significantly smaller than that of charge accumulation. Therefore, by combining the thermodynamic insight from Figure 2.9 with the kinetic analysis of rate constants, it can be concluded that the charge accumulation process is more favorable than the overall OER process from both kinetic and thermodynamic viewpoints.
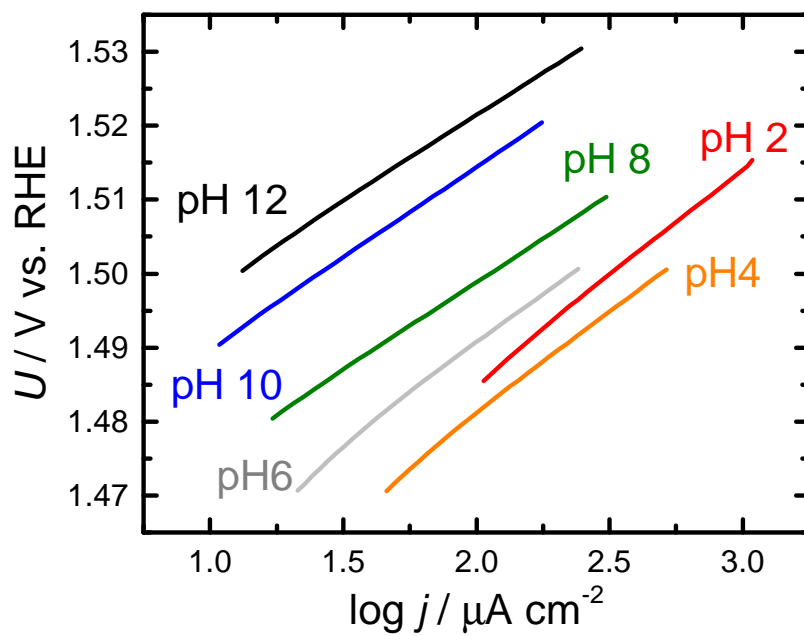
Fig. 2.13 Tafel plots at pH 2, 4, 6, 8, 10, and 12 constructed based on the current-potential relationship obtained from the forward (anodic) scans during cyclic voltammetry.

Table 2.4 Exchange current density of the OER current at pH 2, 4, 6, 8, 10, and 12.

pH	Tafel Slope [mV/dec]	j_0 [μA/cm^2] [a]	Γ [μC/cm^2] [b]	k_0 [1/s] [c]
2	29.0	1.61×10^{-7}	15.6	2.58×10^{-9}
4	28.1	1.22×10^{-7}	16.4	1.86×10^{-9}
6	28.0	5.02×10^{-8}	17.6	7.13×10^{-10}
8	23.7	4.76×10^{-10}	9.39	1.27×10^{-11}
10	24.6	2.69×10^{-10}	7.78	8.64×10^{-12}
12	23.4	3.43×10^{-11}	10.6	8.09×10^{-13}

[a] Exchange current density obtained by extrapolating the Tafel plot shown in Figure 2.13 to 1.23 V vs. RHE.
[b] Coverage of Ir calculated from the charge of E_1. All electrochemically active Ir sites were assumed to be active for OER.
[c] Rate constant at equilibrium potential obtained by the equation $j_0 = nFk_0\Gamma$.

2.4.2 *In-Situ* Evanescent Wave Spectroscopy

In order to gain direct insight into the rate-limiting step of OER on IrO_x *in-situ* evanescent wave spectroscopy was performed. The potential dependence of the evanescent wave subtraction spectra is shown in Figure 2.14. Upon scanning the potential positively from 1.2 to 1.5 V vs. RHE, a species with an absorption maximum at *ca.* 450 nm (hereafter denoted as species A_{450}) was observed. This intermediate was observed consistently regardless of the pH, similar to the onset potential of OER (constant at *ca.* 1.5 V vs. RHE, Figure 2.9), suggesting the participation of this intermediate in the rate-limiting step of the OER. This intermediate was assigned to be an Ir^{5+} species, due to the similarity of the UV–Vis absorption maxima with the Ir^{5+} spectra reported by Castillo-Blum *et al.* (447 nm).[91] This assignment is also in accord with previous *in-situ* X-ray absorption spectroscopy (XAS) and X-ray photoelectron spectroscopy (XPS) studies which report the valence of Ir during OER to be between Ir^{4+} and Ir^{5+}.[54,88,92,93] However, the absorption maxima of Ir^{5+} shows a gradual red-shift from 410 nm to 450 nm during the positive potential scan, indicating the electronic state is potential dependent. In other words, the Ir^{5+} at 1.5 V (species A_{450}) and the Ir^{5+} at 1.3 V, which is expected to be generated during E_2, are different species.

The difference between the two Ir^{5+} species can be confirmed by comparing the pH dependence of their formation. Figure 2.15 shows the potential at which each absorption peak is observed, overlayed on the redox potentials shown in Figure 2.9. The correlation between E_2 and the absorption at 410 nm (Figure 2.15, green and black circles) provide strong evidence that the Ir^{5+} generated by the oxidation of Ir^{4+} during the redox process E_2 is the origin of the absorption maximum at 410 nm. On the other hand, the potential at which the absorption maxima at 450 nm is observed correlates well with the pH-independent behavior of the OER onset potential, and shows a markedly different pH dependence with the absorption at 410 nm. As the pH dependence of redox potentials reflect the

coupling between proton transfer and electron transfer, it can be concluded that the species A_{450} is a different species with the Ir^{5+} formed by the oxidation of Ir^{4+} (redox process E_2). These results indicate that the rate-determining step of the OER on IrO_x is not the valence change of Ir, but an electronic state change of Ir^{5+}, which is represented experimentally by the 40-nm red-shift of the Ir^{5+} absorption spectra. The fact that IrO_x possesses favorable kinetics for valence change suggests O–O bond formation is responsible for the rate-limiting step of OER on IrO_x.
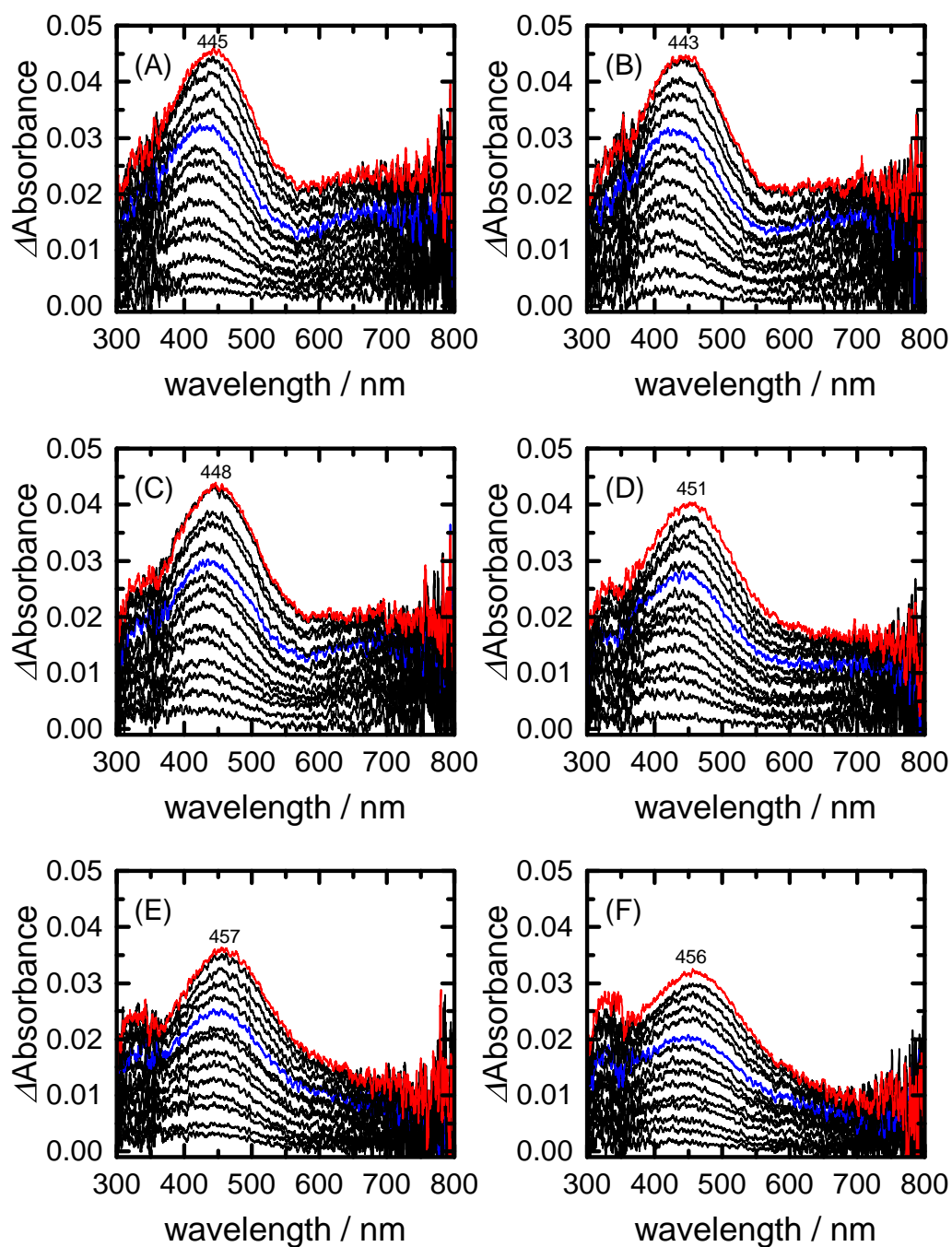
Fig. 2.14   Evanescent wave spectra of IrO$_x$ from 1.2 V and 1.5 V in pH 2 (A), 4 (B), 6 (C), 8 (D), 10 (E), and 12 (F). The spectrum at 1.2 V was used as the reference spectrum. Spectra are shown in 20 mV intervals, and the spectra at 1.5 V and 1.4 V are indicated in red and blue, respectively.
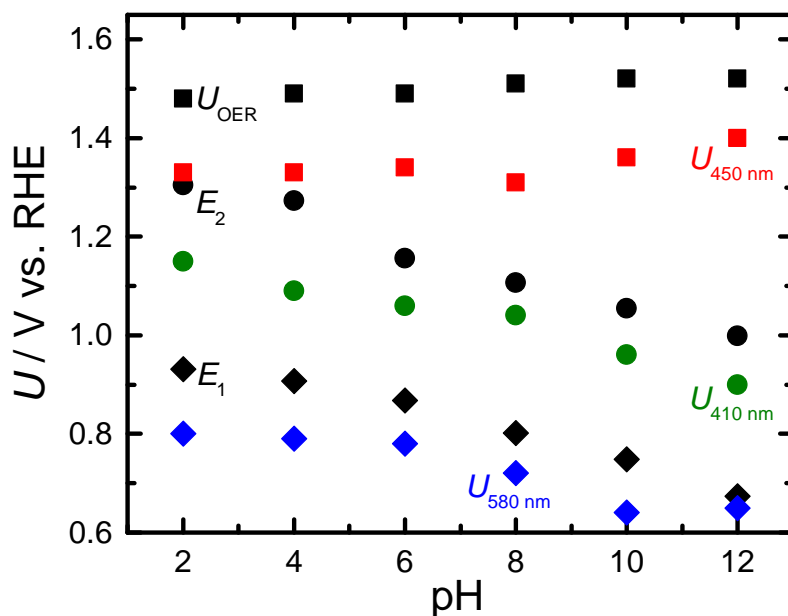
Fig. 2.15 Potentials at which the absorption at 450 nm (red squares), 410 nm (blue diamonds), and 580 nm (green circles) were observed, plotted with respect to the pH of the electrolyte. The onset potential for OER and the potentials for valence change of Ir (E_1, E_2), taken from Figure 2.9, are also plotted in black. The same symbols indicate spectroelectrochemical observations which are expected to be derived from the same physicochemical phenomenon. The onset potential for the absorption at 450 nm indicates the potential where the absorption at 450 nm exceeded 0.02 in Figure 2.14. Onset potentials for the absorptions at 410 nm and 580 nm were defined as the potential where the absorption at the specified wavelength increased by more than 0.005 compared to a spectrum taken at a 100 mV negative potential. The definition of the onset potential differs with that of species A_{450}, because the pH dependence of the absorption at 410 nm and 580 nm hinders the usage of a single potential as a reference.

2.4.3 Action Experiments to Confirm the Legitimacy of Species A_{450} as a Reaction Intermediate

In order to obtain direct evidence that species A_{450} is not a byproduct but a true reaction intermediate which participates in the O–O bond formation step, its interaction with H_2O_2 was studied. H_2O_2 is the two-electron oxidation product of water, and although the H_2O_2 molecule itself is not expected to be generated during the OER, the adsorbed form of H_2O_2 is expected to behave similarly with intermediates which have undergone O–O bond formation such as surface peroxo species.[94,95] Therefore, if the rate-limiting step of OER on IrO_x is truly O–O bond formation, the addition of H_2O_2 to the electrolyte is expected to drastically increase the rate of oxygen generation by allowing for another reaction pathway ($H_2O_2 \rightarrow O_2 + 2\,H^+ + 2\,e^-$) which bypasses the rate-limiting O–O bond formation step. Under such a condition, the formation of species A_{450} is expected to be diminished.

The enhanced formation of oxygen in the presence of H_2O_2 was confirmed based on a combination of electrochemistry with the *in-situ* monitoring of evolved oxygen. Figure 2.16 shows the correlation of the oxygen mass signal (m/z = 32) with the current in the presence and absence of H_2O_2. The addition of H_2O_2 resulted in a *ca.* 300 mV negative shift of the onset potential for both the mass signal and the current, indicating that the bypass reaction pathway made available due to the coexistence of H_2O_2 is more favorable than the original OER pathway. This new current was assigned to the oxidation of H_2O_2 to oxygen, and the enhanced current at higher concentrations of H_2O_2 provides additional evidence that O–O bond formation is responsible for the rate-limiting step of OER on IrO_x (Figure 2.17). Therefore, if species A_{450} is responsible for O–O bond formation, the addition of H_2O_2 is expected to suppress its formation.
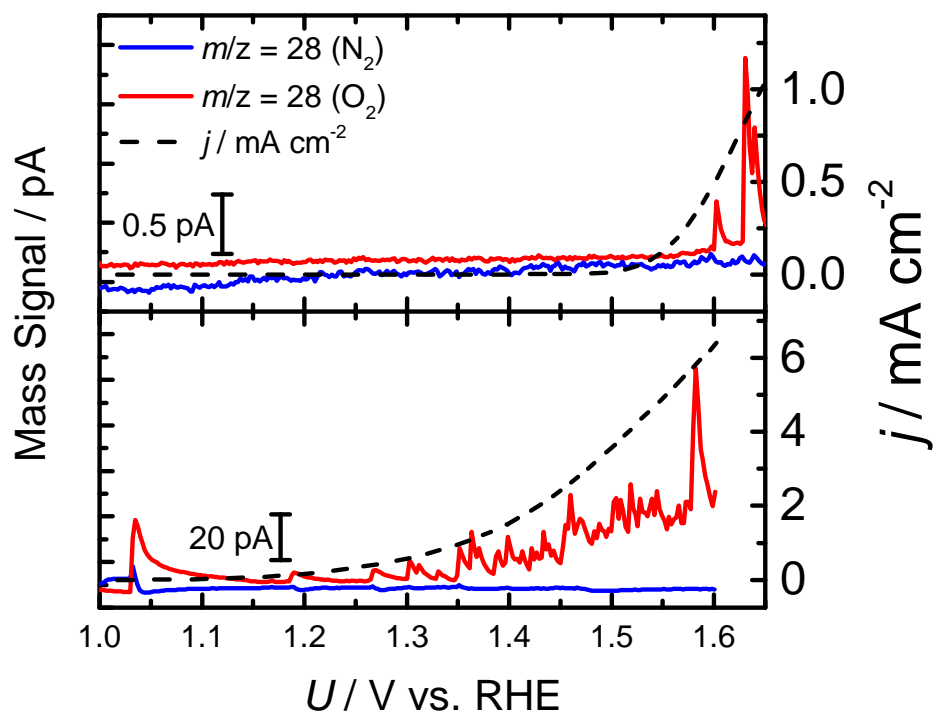
Fig. 2.16   Correlation of the oxygen mass signal ($m/z = 32$) with the OER current in the absence (upper panel) and presence (lower panel) of 0.125 wt% H_2O_2. Potential scan rate: 1 mV/s.
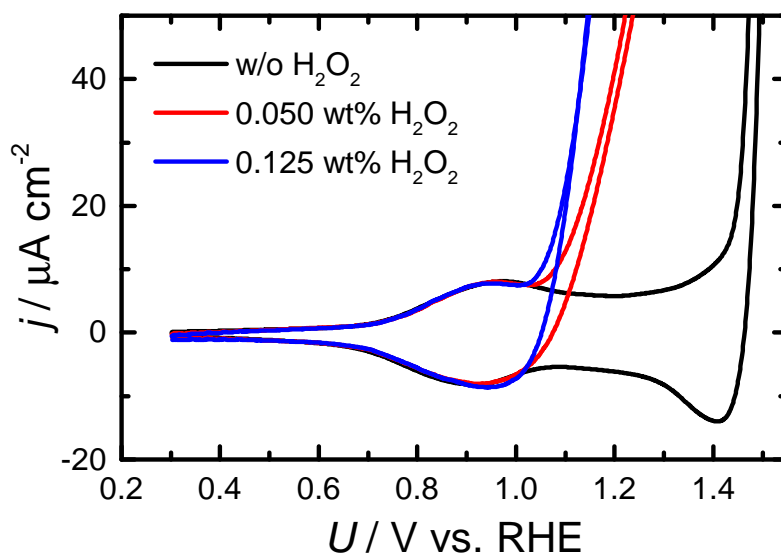
Fig. 2.17   Cyclic voltammograms of the IrO_x film in the presence of different concentrations of H_2O_2. Scan rate: 10 mV/s.

In order to confirm that addition of H_2O_2 inhibits the formation of species A_{450}, *in-situ* evanescent wave spectra were obtained in electrolytes before and after the addition of H_2O_2. Figure 2.18 shows the formation rate of species A_{450} (increase of the absorption at 450 nm per 40-mV potential scan) during a positive potential sweep. In the absence of H_2O_2, the formation rate of species A_{450} increased until *ca.* 1.4 V, which corresponds to the onset potential of OER (U_{OER}). Upon initiation of the OER at potentials above 1.4 V, the rate of absorption increase is suppressed, suggesting the consumption of species A_{450} in a downstream process. Therefore, the distinct shift of the balance between the formation and consumption of species A_{450} before and after the initiation of the OER suggests that species A_{450} is not a byproduct, but a reaction intermediate which is responsible for the rate-limiting step of OER. The effect of H_2O_2 on the formation rate of species A_{450} provides further evidence to this hypothesis, as the formation of species A_{450} was greatly diminished in the presence of H_2O_2. Although a direct reaction between species A_{450} and H_2O_2 cannot be ruled out completely, the cyclic voltammograms shown in Figure 2.17 show that H_2O_2 is readily oxidized by a less-oxidizing species (*e.g.*, Ir^{5+} prior to the red-shift), thus scavenging species A_{450} before it can be formed.

The inhibitory effects of H_2O_2 on the formation of species A_{450} can also be confirmed from the potential dependence of the Ir^{5+} absorption maximum. As can be seen in Figure 2.19, the red-shift of Ir^{5+} is suppressed in the presence of H_2O_2, indicating H_2O_2 inhibits the electronic state change necessary for Ir^{5+} to initiate the OER *via* O–O bond formation.

The direct interaction between H_2O_2 and species A_{450} was confirmed by the addition of H_2O_2 under potentiostatic conditions (Figure 2.20). When H_2O_2 was added into the electrolyte at a potential too negative for OER (1.0 V), no effect on the current density or the absorption at 450 nm could be observed (Figure 2.20, black lines and symbols). However, when H_2O_2 was added at 1.5 V,
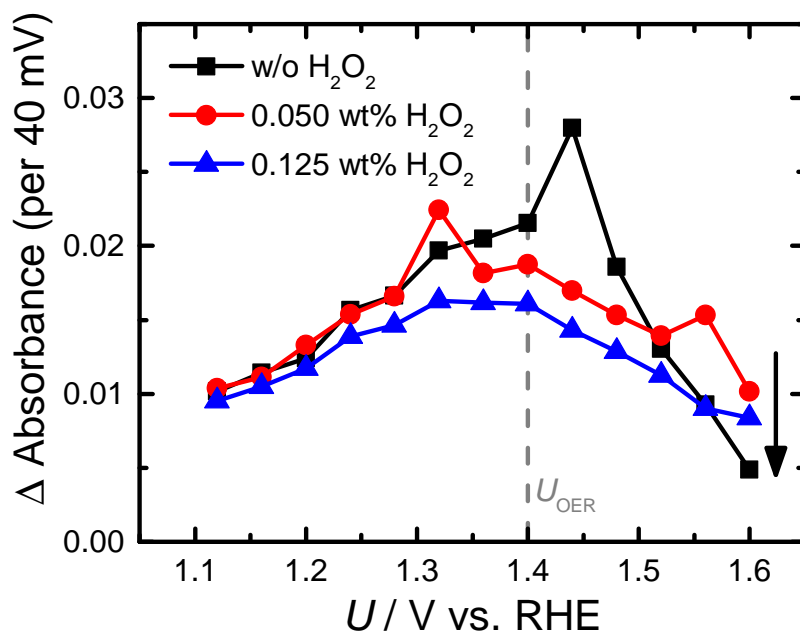
Fig. 2.18 Potential dependence of species A_{450} formation per 40-mV positive potential scan at different concentrations of H_2O_2. Vertical line indicates the onset of OER (U_{OER}).
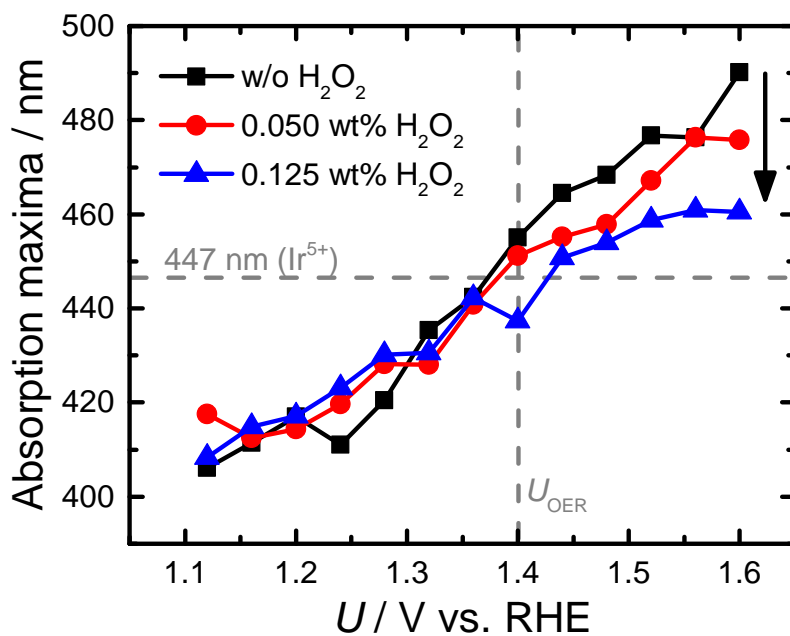
Fig. 2.19 Suppression of Ir^{5+} red-shift upon addition of H_2O_2. Absorption maxima of the generated species per 40-mV scan were measured under the same conditions as in Figure 2.18. Vertical and horizontal lines indicate the onset of OER (U_{OER}) and the literature value (447 nm) of Ir^{5+} absorption.

an abrupt increase in the current density (solid red line) was observed, due to the oxidation of H_2O_2 to O_2. This increase in the current was accompanied by a decrease in the absorption at 450 nm (red filled circle). As H_2O_2 was consumed, both the current and absorbance returned to their original values in a similar time scale (time constant $\tau_{\text{current}} = 4.9$ seconds, $\tau_{\text{absorbance}} = 5.3$ seconds). The amount of species A_{450} scavenged by the addition of H_2O_2 can be estimated to be *ca.* 50 % (0.06 absorbance units) of the total amount of species A_{450}, based on the amount of species A_{450} formed during the positive potential scan (Figure 2.14). The fact that these transient effects were observed only in the presence of both species A_{450} and H_2O_2 provide compelling evidence that H_2O_2 suppresses the formation of species A_{450}. Furthermore, because the role of H_2O_2 in the context of OER is to provide a bypass route to O–O bond formation, the negative interaction between species A_{450} and H_2O_2 suggests that species A_{450} is responsible for mediating O–O bond formation.
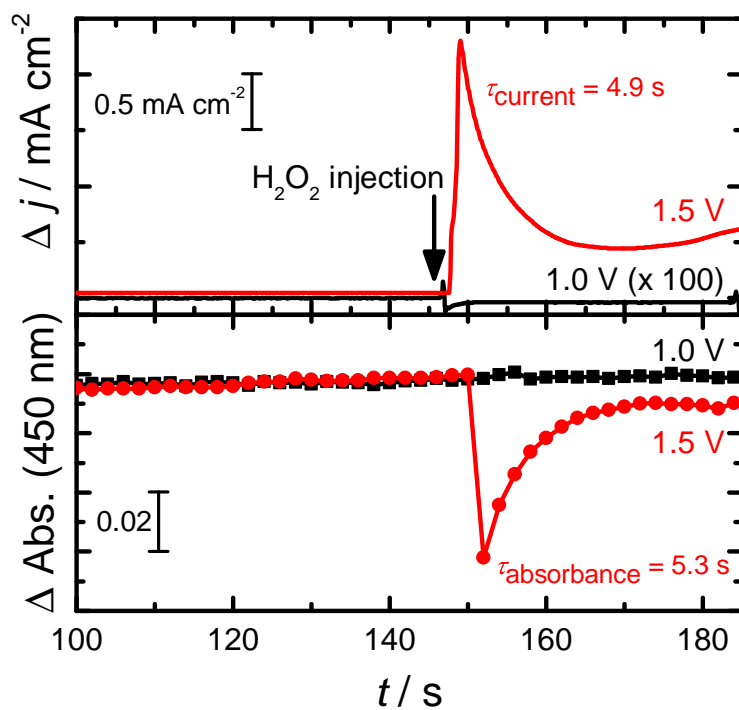
Fig. 2.20   The time profile of the current density (upper panel) and absorption at 450 nm (lower panel) before and after H_2O_2 addition, at potentials above (1.5 V) and below (1.0 V) the onset of oxygen evolution. Values have been offset to highlight the change upon H_2O_2 addition.

2.4.4 Assignment of Species A$_{450}$

In order to gain insight into the chemical origin of species A$_{450}$, the UV–Vis spectra of Ir^{5+} were simulated using DFT calculations. A binuclear Ir^{5+}–Ir^{5+} cluster was chosen in favor of the rutile Ir oxides used previously in computation to account for the hydrated nature of IrO$_{x}$. Not only is the hydrated structure more active as an OER catalyst, the voltammetric features are also markedly different, indicating the rutile structure is not an accurate representation of the IrO$_{x}$ studied in this chapter. As shown in Table 2.5, the quintet state was found to be the most stable Ir^{5+} structure, followed by the triplet state. The structures and molecular coordinates of the quintet and triplet states are given in Figure 2.21 and Tables 2.6 and 2.7. The relative stability of the quintet and triplet state persists regardless of symmetry constraints or solvation effects, and therefore, the UV–Vis spectra of these structures were modeled as the most likely candidates for the origin of the absorption maxima at 450 nm.

Table 2.5   Relative energies of the Ir^{5+} binuclear structure.

Spin state	Energy[a]	Energy[b]	Energy[c]
Singlet	13.03	10.89	13.23
Triplet	8.43	3.02	4.58
Quintet	0	0	0
Septet	57.34	-[d]	-[d]
Nonet	82.41	-[d]	-[d]

[a] C_{2v} symmetry in gas phase.
[b] No symmetry constraint in gas phase.
[c] No symmetry constraint with solvation (PCM: polarized continuum model).
[d] The energies for the septet and nonet states were found to be prohibitively more unstable compared to the quintet state (> 50 kcal/mol) when the structure was optimized with symmetry constraints and without solvation effects and therefore were not studied under different conditions. Energies are reported with respect to the quintet state in kcal/mol units. No imaginary frequencies were observed in the final structures.
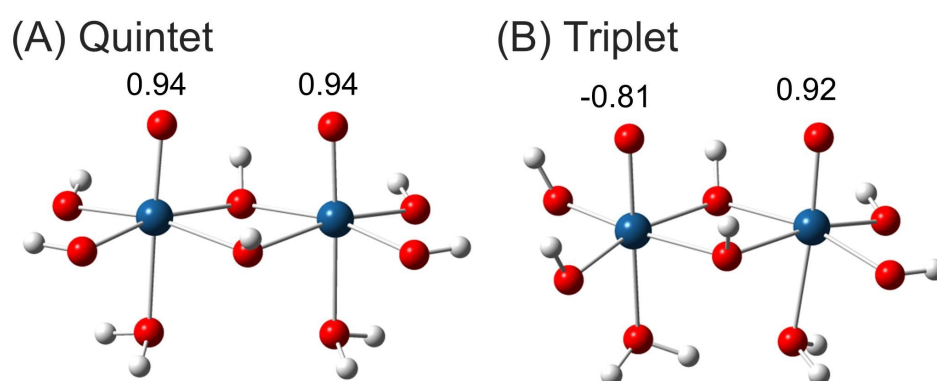
Fig. 2.21 Structures of the Ir^{5+}–Ir^{5+} binuclear cluster optimized without symmetry constraints in a solvated environment. The atomic coordinates of these structures can be found in Tables 2.6 and 2.7. The numbers indicate the spin density of the two oxygen atoms involved in the spin inversion and the O–O bond formation.

Table 2.6 Molecular coordinates of the Ir^{5+} cluster in the quintet state.

Atom	Coordinates		
Ir	-1.65167000	-0.10316400	0.19558000
Ir	1.65088500	-0.10145700	0.19857400
H	-2.89929400	2.05968600	0.22599400
H	-0.00191800	1.90914800	0.74450700
H	2.89624100	2.06267900	0.23023200
H	3.88892400	-1.03864700	-0.02744300
H	0.00050900	-2.19267800	0.43922300
H	-3.88839300	-1.04234000	-0.03467400
O	-3.17600400	1.16050300	0.00973400
O	-3.03193100	-1.49356500	-0.05013300
O	-0.00097500	1.22045300	0.06782500
O	0.00053400	-1.37187300	-0.06919400
O	3.17426400	1.16366800	0.01494100
O	3.03288100	-1.49060700	-0.04439100
H	2.45461500	0.59651600	-2.23616200
H	1.89501200	-0.83781600	-2.42128100
H	-1.89205100	-0.83930100	-2.42448100
H	-2.45085200	0.59543600	-2.24056500
O	1.55926600	-0.15344600	1.97292400
O	-1.56310500	-0.15543400	1.97006900
O	1.69575700	0.02689500	-2.03308400
O	-1.69269100	0.02534300	-2.03618800

Table 2.7   Molecular coordinates of the Ir^{5+} cluster in the triplet state.

Atom	Coordinates		
Ir	-1.58006000	0.06317600	0.19203500
Ir	1.69617900	-0.14419100	0.05454500
H	-3.73154300	1.12656700	-0.23350900
H	0.23474300	1.80542900	0.92273000
H	3.46726800	1.55153100	0.43060800
H	3.36135200	-1.69161900	0.88018300
H	-0.03718600	-1.97357300	0.88566800
H	-2.88167100	-2.04135600	-0.00822100
O	-2.85067200	1.52453500	-0.17367300
O	-3.12420700	-1.12206000	-0.17796900
O	0.15257200	1.27458300	0.11762300
O	-0.02526700	-1.36647600	0.13417700
O	3.05325700	1.19269100	-0.36525500
O	2.88348300	-1.67606400	0.03573500
H	0.55900100	-0.10864700	-2.41800300
H	2.04135100	0.36136500	-2.59298900
H	-1.88609500	-0.64632800	-2.43335700
H	-1.72820400	0.89669200	-2.38960500
O	1.87458800	-0.02672100	1.92917000
O	-1.62453400	0.06908900	1.96613100
O	1.47952900	-0.29115400	-2.15065300
O	-1.33420700	0.06697900	-2.07260900

The UV–Vis spectra of the Ir^{5+} in these structures are shown in Figure 2.22. The UV–Vis spectra of the quintet state, which was the most stable structure out of the 40 structures examined, possessed an absorption maximum at *ca.* 399 nm (d-d transition, Figure 2.22, trace a), which is comparable to the experimentally observed peak at *ca.* 410 nm in experiments. On the other hand, the triplet state had two peaks at *ca.* 396 nm and 491 nm (also d-d transitions, Figure 2.22, trace b). The transition from the quintet state to the triplet state *via* spin inversion of an oxygen ligand yields a differential spectrum with an absorption maximum near 490 nm (Figure 2.22, trace c), which matches well with the spectrum of the fully red-shifted species (Figure 2.19). These calculations indicate the generation of species A_{450} from Ir^{5+} may be assignable to a spin-inversion of an oxygen ligand.
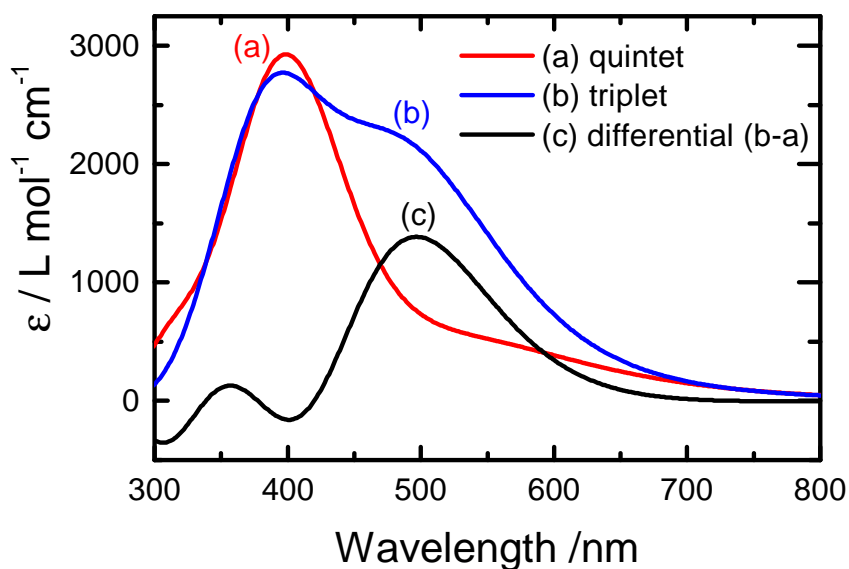
Fig. 2.22 UV–Vis spectra simulated using DFT calculations in the quintet (a) and triplet (b) state. The differential spectrum (b-a) is shown in (c).

Further support for the assignment of the red-shift of Ir^{5+} to the spin transition of an oxygen ligand can be found in Figure 2.23, which shows the energy of the quintet and triplet structures with respect to the distance between the two topmost oxygen atoms. This distance represents the reaction coordinates of O–O bond formation. Most notably, the triplet state was found to have favorable energetics for O–O bond formation, due to the decrease of free energy upon decreasing the O–O distance. In contrast, the energy of the quintet state exhibits a marked increase upon shortening the O–O bond. These results indicate a transition from the quintet state to a triplet state would initiate O–O bond formation, which was suggested to be the rate-limiting step based on the H_2O_2 experiments. The mechanism of a non-electrochemical elementary step, preceded by a kinetically favorable electrochemical step, is consistent with the experimentally observed Tafel slope of 30 mV/dec. The activation barrier of *ca.* 14 kcal/mol for O–O bond formation, obtained from the intersection in Figure 2.23, is also consistent with previously proposed values of O–O bond formation (15-20 kcal/mol). [96,97] Therefore, it can be expected that the generation of species A_{450} *via* the red-shift of the Ir^{5+} is due to a spin inversion at an oxygen ligand of Ir^{5+}. This assignment is supported by a recent DFT study by Ping *et al.* [98] which reports a spin transition of the adsorbed oxygen atom upon desorption of molecular oxygen. A recent study by Pfeifer *et al.* [99] has also experimentally confirmed the active participation of the oxygen ligand during the OER on IrO_x, as the oxidation state change of oxygen ligands were observed directly using *in-situ* XAS. Therefore, the rate-limiting step of OER on IrO_x can be expected to be the spin inversion of an oxygen ligand ligated to Ir^{5+}, which was observed experimentally as the generation of an absorption maxima at 450 nm.
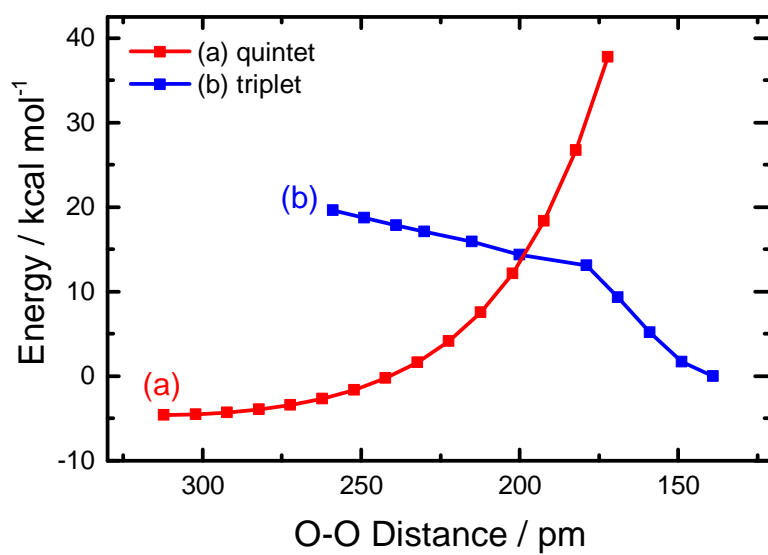
Fig. 2.23 Energies of the quintet and triplet states as a function of the distance between the two topmost oxygen atoms. Colors are the same as in Figure 2.22.

68

Figure 2.24 shows the proposed OER mechanism of IrO_x, based on the electrochemistry, *in-situ* evanescent wave spectroscopy, intermediate scavenging experiments, and DFT calculations shown in this chapter. The Ir ions are gradually oxidized from Ir^{3+} to Ir^{4+}, and from Ir^{4+} to Ir^{5+} as observed both spectroscopically (absorption maxima: 570 nm, 410 nm) and electrochemically (redox peaks: E_1, E_2). However, the Ir^{5+} thus generated is still insufficient to initiate the O–O bond formation. O–O bond formation is initiated only after one of the oxygen ligands of Ir^{5+} has undergone a spin inversion, as observed in the red-shift of the absorption maxima of Ir^{5+}, and the energetics of O–O bond formation obtained computationally. The fact that O–O bond formation is rate-limiting is supported by the drastic increase in the oxygen generation rate upon H_2O_2 addition, as well as the inhibitory effects of H_2O_2 on the spin inversion of oxygen. These results indicate that the charge accumulation process *via* the valence change of Ir ($Ir^{3+} \rightarrow Ir^{4+} \rightarrow Ir^{5+}$) is not the rate-limiting factor for OER on IrO_x. This OER mechanism is in stark contrast to that proposed for MnO_2[37,38,78] or Fe_2O_3,[39,40] where the inefficiency of charge accumulation was found to dictate the overall activity as an OER catalyst.
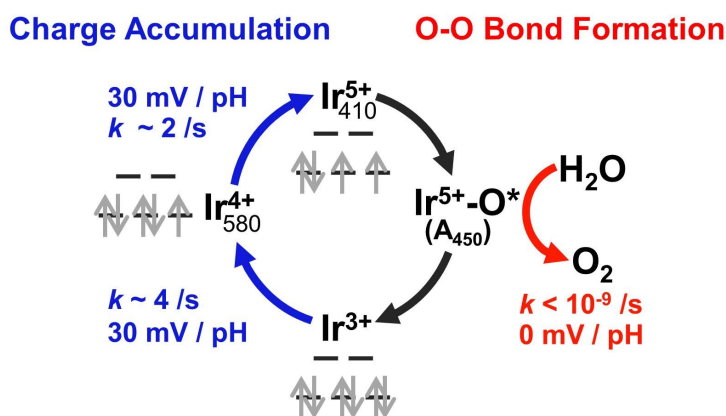
Fig. 2.24   Proposed mechanism of OER on IrO_x based on the results of this study.

2.4.5   Charge Disproportionation and Mechanistic Differences with 3d-Metal Oxides

The contrasting OER mechanism based on the difference of charge accumulation between the 3d-metal catalysts (MnO_2, Fe_2O_3) and the 4d/5d-metal catalyst (IrO_x) may be due to the difference in electronic configuration. In the case of MnO_2 and Fe_2O_3, the formation of an intermediate in the high-spin d^4 electronic state (Mn^{3+} and Fe^{4+}, respectively) was found to be the rate-limiting step of OER in both electrochemical[37–40,78] and photoelectrochemical systems.[100,101] One possible explanation may be because a degeneracy within the e_g orbital decreases the stability with respect to charge disproportionation ($2d^4 \rightarrow d^3 + d^5$, Figure 2.25A). On the other hand, the low-spin electronic structure of Ir would prevent charge disproportionation in advance (Figure 2.25B), as even the most reduced Ir valence observed in this study (Ir^{3+}) has only 6 electrons, which can be accommodated within the t_{2g} orbital. As an alternative explanation, it is also possible to attribute the suppressed activity of the high-spin d^4 electronic structure to their tendency to undergo Jahn-Teller distortion, which was previously proposed to be detrimental to the activity of Mn^{3+}-based electrocatalysts.[102] In either case, a low spin electronic configuration with no e_g electrons would allow for a more favorable charge accumulation process as shown in Figure 2.24. The relationship between OER activity and mechanism with respect to the charge accumulation efficiency will be discussed mathematically in the following section.
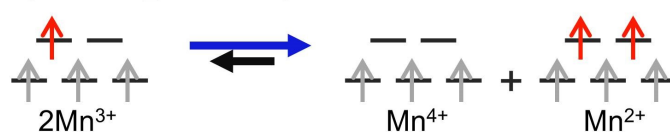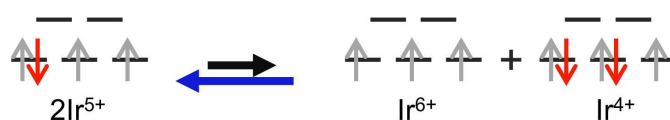
Fig. 2.25 Comparison of MnO_2 (A) and IrO_x (B) catalysts based on their electron configuration and instability to charge disproportionation.

2.4.6 Implications of an Efficient Charge Accumulation Process

In order to discuss the implications of an efficient charge accumulation process, and to rationalize why a difference in the OER mechanism would lead to higher catalytic activity, a mathematical analysis of Tafel slopes will be presented.

The Tafel slope is defined as the potential difference necessary to generate a 10-fold increase in current, and indicates the kinetic efficiency of a catalyst, with smaller Tafel slopes corresponding to higher activity. For example, the Tafel slope of the IrO_x presented in this study is *ca.* 30 mV/dec (Table 2.4)[*4], indicating only a 30 mV potential scan is necessary to increase the current density by an order of magnitude. In contrast, the Tafel slope of MnO_2 is *ca.* 120 mV/dec,[61,103] which is drastically less efficient.

$$\text{Tafel slope} \equiv \frac{\partial U}{\partial \mid \log j \mid} [\text{mV/dec}] \tag{2.11}$$

where U and j indicate the electrode potential and the current density. The "dec" in the unit [mV/dec] is an abbreviation for "decade".

The potential dependence of an electrocatalytic reaction can be expressed based on the Butler–Volmer equation. If the reverse reaction is negligible, *i.e.*, the difference between the electrode potential (U) and the equilibrium potential of OER (U_{OER}) is sufficiently large, the current-potential relationship can be expressed as:

$$j = nFk_0[C]_{rds}{}^r (\exp \frac{\alpha_{rds} F(U - U_{OER})}{RT} \tag{2.12}$$

Here, n, F, k_0, R, and T have their usual notations of number of electrons transferred, Faraday constant, heterogeneous rate constant (rate constant at equilibrium potential), gas constant, and absolute temperature, respectively. The notations $[C]_{rds}$, r, and α_{rds} represent the concentration of the rate-limiting

---

[*4] There are also studies which report a Tafel slope of 40 mV/dec.[21]

intermediate, the reaction order, and the transfer coefficient of the rate-limiting step. Based on Equations 2.11 and 2.12, the Tafel slope can be expressed as:

$$\log j = r\log(nFk_0[C]_\text{rds}) + \log\frac{\alpha_\text{rds}FU}{RT} - \log\frac{\alpha_\text{rds}FU_\text{OER}}{RT}$$

$$\therefore \frac{1}{\text{Tafel slope}} = \frac{\partial\mid\log j\mid}{\partial U} = r\frac{\partial[C]_\text{rds}}{\partial U} + \frac{\alpha_\text{rds}F}{RT\ln 10} \tag{2.13}$$

When the concentration of the rate-limiting intermediate ($[C]_\text{rds}$) is potential independent, $i.e.$, $\frac{\partial[C]_\text{rds}}{\partial U} = 0$, the Tafel slope is determined solely by the second term in Equation 2.13. Substituting the constants with their common values (R) = 8.314 [J K^{-1} mol^{-1}], T = 300 [K] , α = 0.5 [/1], F = 96485 [C/mol]) yields a Tafel slope of 119 [mV/dec]. This is in accord to the Tafel slope of MnO_2, and is also in accord with the OER mechanism of MnO_2, where the concentration of the rate-limiting intermediate (Mn^{2+}) is not expected to increase with the potential.

On the other hand, a Tafel slope smaller than 120 mV/dec can be realized if the concentration of the rate-limiting intermediate is potential dependent ($\frac{\partial[C]_\text{rds}}{\partial U} >$ 0).[100,104,105] For example, if the kinetics of the electrochemical step prior to the rate-limiting step is sufficiently fast, this step can be assumed to be in equilibrium ($[C]_\text{pre} \rightleftharpoons [C]_\text{rds} \xrightarrow{slow} O_2$). Therefore, the concentration of the intermediate responsible for the rate-limiting step ($[C]_\text{rds}$) and its precursor ($[C]_\text{pre}$) can be expressed based on the Nernst equation as follows:

$$U = U_\text{eq} - \frac{RT}{F}ln\frac{[C]_\text{rds}}{[C]_\text{pre}} \leftrightarrow [C]_\text{rds} = [C]_\text{pre}\exp(\frac{F(U - U_\text{OER})}{RT}) \tag{2.14}$$

Therefore, substituting $[C]_\text{rds}$ with $[C]_\text{pre}$ gives the following expression for the Tafel slope:

$$\frac{1}{\text{Tafel slope}} = r\frac{\partial[C]_\text{pre}}{\partial U} + \frac{rF}{RT\ln 10} + \frac{\alpha_\text{rds}}{RT\ln 10} \tag{2.15}$$

Although the value of $\frac{\partial [C]_{pre}}{\partial U}$ is not clear, this would lead to a decrease in the Tafel slope, because in most cases, $\frac{\partial [C]_{pre}}{\partial U} > 0$.[*5]

Even when $\frac{\partial [C]_{pre}}{\partial U} = 0$, if $r = 2$, $\alpha_{rds} = 0$, this would yield a Tafel slope of 30 mV/dec. These values correspond to a mechanism where the coverage of a reaction intermediate (Ir^{5+}) is in equilibrium with its precursor (Ir^{4+}), and the reaction of Ir^{5+} to species A_{450} is the rate-limiting step *via* a direct coupling O–O bond formation mechanism ($\alpha_{rds} = 0$). In other words, the Tafel slope obtained experimentally is consistent with the O–O bond formation mechanism of direct–coupling and the fast kinetics of charge accumulation with respect to the OER.

The enhanced sensitivity of the reaction rate with respect to the electrode potential upon introducing a potential dependence in $[C]_{rds}$ holds true qualitatively, regardless of the reaction mechanism (values of r and α_{rds}). For example, the most well-known example where a Tafel slope is less than 120 mV/dec may be hydrogen evolution on platinum in acidic electrolytes, which exhibits Tafel slopes of 40 mV/dec[104] ($r = 1$ and $\alpha_{rds} = 0.5$). The reaction mechanism for IrO_x OER catalysts and Pt hydrogen evolution catalysts is in stark contrast to the OER mechanism of MnO_2 (Tafel slope $= 120$ mV/dec), where the accumulation of the rate-limiting intermediate (Mn^{2+}) is minimal at anodic potentials. Therefore, a catalyst which can accumulate the rate-limiting intermediate *via* favorable charge accumulation steps is expected to show enhanced kinetics in general. In other words, the favorable charge accumulation process of the 4d/5d-metals, due to their low-spin electronic configuration, may be the origin of the difference in activity between 3d-metals and 4d/5d-metals.

[*5] An exception may be in the case where $[C]_{pre}$ is involved in charge disproportionation

2.5 Summary and Conclusions

The OER mechanism of IrO_x was studied using electrochemistry and *in-situ* evanescent wave spectroscopy from the viewpoint of charge accumulation in order to understand the mechanistic origin of the high activity of 4d/5d rare-metal catalysts. Based on cyclic voltammetry and the pH dependence of redox potentials, the author has confirmed that the valence change of Ir ions in IrO_x are more favorable than the overall OER process, both kinetically and thermodynamically. Based on *in-situ* evanescent wave spectroscopy and DFT calculations, the rate-limiting step was found to be the spin-inversion of Ir^{5+}, which adds further support that valence change and charge accumulation is not rate-limiting on IrO_x. The efficiency of the charge accumulation process allows the concentration term of the Butler–Volmer equation (Equation 2.12) to contribute to the overall reaction rate, enhancing the kinetics of IrO_x as an OER catalyst. Activity enhancement *via* the accumulation of reaction intermediates is known to occur on other 4d/5d rare-metal catalysts such as Pt, indicating its importance in terms of comparison between 3d-metals and 4d/5d rare-metals. This mechanistic difference may occur based on differences in the electronic configuration, giving critical insight into the reason why many 4d/5d rare-metal catalysts show superior activity compared to their 3d-metal counterparts.

References

[1] Ooka, H.; Wang, Y.; Yamaguchi, A.; Hatakeyama, M.; Nakamura, S.; Hashimoto, K.; Nakamura, R. *Phys. Chem. Chem. Phys.* **2016**, *18*, 15199–15204.

[2] Ooka, H.; Yamaguchi, A.; Takashima, T.; Hashimoto, K.; Nakamura, R. *J. Phys. Chem. C* **2017**, *121*, 17873–17881.

[3] Ooka, H.; Takashima, T.; Yamaguchi, A.; Hayashi, T.; Nakamura, R. *Chem. Commun.* **2017**, *53*, 7149–7161.

[4] Yano, J.; Yachandra, V. *Chem. Rev.* **2014**, *114*, 4175–4205.

[5] Vinyard, D. J.; Ananyev, G. M.; Charles Dismukes, G. *Annu. Rev. Biochem.* **2013**, *82*, 577–606.

[6] Vinyard, D. J.; Gimpel, J.; Ananyev, G. M.; Cornejo, M. A.; Golden, S. S.; Mayfield, S. P.; Dismukes, G. C. *J. Biol. Chem.* **2013**, *288*, 5451–5462.

[7] Yoshikawa, S.; Shinzawa-Itoh, K.; Nakashima, R.; yaono, R.; Yamashita, E.; Inoue, N.; Yao, M.; Fei, M. J.; Libeu, C. P.; Mizushima, T.; Yamaguchi, H.; Tomizaki, T.; Tsukihara, T. *Science* **1998**, *280*, 1723–1729.

[8] Tsukihara, T.; Aoyama, H.; Yamashita, E.; Tomizaki, T.; Yamaguchi, H.; Shinzawa-Itoh, K.; Nakashima, R.; Yaono, R.; Yoshikawa, S. *Science* **1995**, *269*, 1069–1074.

[9] Yachandra, V.; Powers, L.; Spiro, T. G. *J. Am. Chem. Soc.* **1983**, *105*, 6596–6604.

[10] Lindskog, S.; Thorslund, A. *FEBS J.* **1968**, *3*, 453–460.

[11] Thorslund, A.; Lindskog, S. *FEBS J.* **1967**, *3*, 117–123.

[12] Håkansson, K.; Wehnert, A. *J. Mol. Biol.* **1992**, *228*, 1212–1218.

[13] Volbeda, A.; Charon, M.-H.; Piras, C.; Hatchikian, E. C.; Frey, M.; Fontecilla-Camps, J. C. *Nature* **1995**, *373*, 580.

[14] Albracht, S. P. *Biochim. Biophys. Acta* **1994**, *1188*, 167–204.

[15] Halcrow, M. A. *Angew. Chem. Int. Ed.* **1995**, *34*, 1193–1195.

[16] Wharton, D. C.; Tzagoloff, A. *Methods Enzymol.* **1967**, *10*, 245–250.

[17] Iwata, S.; Ostermeier, C.; Ludwig, B.; Michel, H. *Nature* **1995**, *376*, 660–669.

[18] Burke, L. D.; Murphy, O. J.; O'Neill, J. F.; Venkatesan, S. *J. Chem. Soc. Faraday Trans.* **1977**, *73*, 1659–1671.

[19] Reier, T.; Oezaslan, M.; Strasser, P. *ACS Catal.* **2012**, *2*, 1765–1772.

[20] Lee, Y.; Suntivich, J.; May, K. J.; Perry, E. E.; Shao-Horn, Y. *J. Phys. Chem. Lett.* **2012**, *3*, 399–404.

[21] Zhao, Y.; Vargas-Barbosa, N. M.; Hernandez-Pagan, E. A.; Mallouk, T. E. *Small* **2011**, *7*, 2087–2093.

[22] Seitz, L. C.; Dickens, C. F.; Nishio, K.; Hikita, Y.; Montoya, J.; Doyle, A.; Kirk, C.; Vojvodic, A.; Hwang, H. Y.; Norskov, J. K.; Jaramillo, T. F. *Science* **2016**, *353*, 1011–1014.

[23] Geiger, S.; Kasian, O.; Shrestha, B. R.; Mingers, A. M.; Mayrhofer, K. J.; Cherevko, S. *J. Electrochem. Soc.* **2016**, *163*, F3132–F3138.

[24] Yagi, M.; Tomita, E.; Kuwabara, T. *J. Electroanal. Chem.* **2005**, *579*, 83–88.

[25] Slavcheva, E.; Radev, I.; Bliznakov, S.; Topalov, G.; Andreev, P.; Budevski, E. *Electrochim. Acta* **2007**, *52*, 3889–3894.

[26] McKone, J. R.; Warren, E. L.; Bierman, M. J.; Boettcher, S. W.; Brunschwig, B. S.; Lewis, N. S.; Gray, H. B. *Energy Environ. Sci.* **2011**, *4*, 3573–3583.

[27] Sheng, W.; Gasteiger, H. A.; Shao-Horn, Y. *J. Electrochem. Soc.* **2010**, *157*, B1529–B1536.

[28] Lim, B.; Jiang, M.; Camargo, P. H.; Cho, E. C.; Tao, J.; Lu, X.; Zhu, Y.; Xia, Y. *Science* **2009**, *324*, 1302–1305.

[29] Gasteiger, H. A.; Kocha, S. S.; Sompalli, B.; Wagner, F. T. *Appl. Catal. B* **2005**, *56*, 9–35.

[30] Chen, Y.; Li, C. W.; Kanan, M. W. *J. Am. Chem. Soc.* **2012**, *134*, 19969–19972.

[31] Hori, Y.; Wakebe, H.; Tsukamoto, T.; Koga, O. *Electrochim. Acta* **1994**, *39*, 1833–1839.

[32] Cave, E. R.; Montoya, J. H.; Kuhl, K. P.; Abram, D. N.; Hatsukade, T.; Shi, C.; Hahn, C.; Nørskov, J. K.; Jaramillo, T. F. *Phys. Chem. Chem. Phys.* **2017**, *19*, 15856–15863.

[33] Ma, M.; Trześniewski, B. J.; Xie, J.; Smith, W. A. *Angew. Chem. Int. Ed.* **2016**, *55*, 9748–9752.

[34] Pushkar, Y.; Yano, J.; Sauer, K.; Boussac, A.; Yachandra, V. K. *Proc. Natl. Acad. Sci. U. S. A.* **2008**, *105*, 1879–1884.

[35] Cox, N.; Retegan, M.; Neese, F.; Pantazis, D. A.; Boussac, A.; Lubitz, W. *Science* **2014**, *345*, 804–808.

[36] Krewald, V.; Neese, F.; Pantazis, D. A. *Isr. J. Chem.* **2015**, *55*, 1219–1232.

[37] Takashima, T.; Hashimoto, K.; Nakamura, R. *J. Am. Chem. Soc.* **2012**, *134*, 1519–1527.

[38] Yamaguchi, A.; Inuzuka, R.; Takashima, T.; Hayashi, T.; Hashimoto, K.; Nakamura, R. *Nat. Commun.* **2014**, *5*.

[39] Takashima, T.; Ishikawa, K.; Irie, H. *J. Phys. Chem. C* **2016**, *120*, 24827–24834.

[40] Takashima, T.; Ishikawa, K.; Irie, H. *Chem. Commun.* **2016**, *52*, 14015–14018.

[41] Nørskov, J. K.; Studt, F.; Abild-Pedersen, F.; Bligaard, T. *Fundamental Concepts in Heterogeneous Catalysis*; John Wiley and Sons, 2014.

[42] Kanan, M. W.; Nocera, D. G. *Science* **2008**, *321*, 1072–1075.

[43] Morris, N. D.; Suzuki, M.; Mallouk, T. E. *J. Phys. Chem. A* **2004**, *108*, 9115–9119.

[44] Trześniewski, B. J.; Diaz-Morales, O.; Vermaas, D. A.; Longo, A.; Bras, W.; Koper, M. T.; Smith, W. A. *J. Am. Chem. Soc.* **2015**, *137*, 15112–15121.

[45] Man, I. C.; Su, H.-Y.; Calle-Vallejo, F.; Hansen, H. A.; Martínez, J. I.; Inoglu, N. G.; Kitchin, J.; Jaramillo, T. F.; Nørskov, J. K.; Rossmeisl, J. *ChemCatChem* **2011**, *3*, 1159–1165.

[46] Greeley, J.; Jaramillo, T. F.; Bonde, J.; Chorkendorff, I.; Nørskov, J. K. *Nat Mater.* **2006**, *5*, 909–913.

[47] Hori, Y.; Kikuchi, K.; Suzuki, S. *Chem. Lett.* **1985**, *14*, 1695–1698.

[48] Hori, Y.; Kikuchi, K.; Murata, A.; Suzuki, S. *Chem. Lett.* **1986**, *15*, 897–898.

[49] Schouten, K. J. P.; Gallent, E. P.; Koper, M. T. *J. Electroanal. Chem.* **2014**, *716*, 53–57.

[50] Peterson, A. A.; Abild-Pedersen, F.; Studt, F.; Rossmeisl, J.; Nørskov, J. K. *Energy Environ. Sci.* **2010**, *3*, 1311.

[51] Tang, W.; Peterson, A. A.; Varela, A. S.; Jovanov, Z. P.; Bech, L.; Durand, W. J.; Dahl, S.; Nørskov, J. K.; Chorkendorff, I. *Phys. Chem. Chem. Phys.* **2012**, *14*, 76–81.

[52] Tributsch, H. *Phys. Status Solidi. A* **2014**, *211*, 2052–2062.

[53] Yeo, R.; Orehotsky, J.; Visscher, W.; Srinivasan, S. *J. Electrochem. Soc.* **1981**, *128*, 1900–1904.

[54] Sardar, K.; Petrucco, E.; Hiley, C. I.; Sharman, J. D.; Wells, P. P.; Russell, A. E.; Kashtiban, R. J.; Sloan, J.; Walton, R. I. *Angew. Chem. Int. Ed.* **2014**, *53*, 10960–10964.

[55] Owe, L.-E.; Tsypkin, M.; Wallwork, K. S.; Haverkamp, R. G.; Sunde, S. *Electrochim. Acta* **2012**, *70*, 158–164.

[56] Vesborg, P. C.; Jaramillo, T. F. *RSC Adv.* **2012**, *2*, 7933–7947.

[57] McCrory, C. C. L.; Jung, S.; Ferrer, I. M.; Chatman, S. M.; Peters, J. C.; Jaramillo, T. F. *J. Am. Chem. Soc.* **2015**, *137*, 4347–4357.

[58] McCrory, C. C.; Jung, S.; Peters, J. C.; Jaramillo, T. F. *J. Am. Chem. Soc.* **2013**, *135*, 16977–16987.

[59] Xu, Q.-Z.; Xu, Q.-Z.; Su, Y.-Z.; Wu, H.; Cheng, H.; Hui, Y.-P.; Li, N.; Liu, Z.-Q. *Curr. Nanosci.* **2014**, *11*, 107.

[60] Esswein, A. J.; Surendranath, Y.; Reece, S. Y.; Nocera, D. G. *Energy Environ. Sci.* **2011**, *4*, 499–504.

[61] Huynh, M.; Bediako, D. K.; Nocera, D. G. *J. Am. Chem. Soc.* **2014**, *136*, 6002–6010.

[62] Huynh, M.; Bediako, D. K.; Liu, Y.; Nocera, D. G. *J. Phys. Chem. C* **2014**, *118*, 17142–17152.

[63] Carmo, M.; Fritz, D. L.; Mergel, J.; Stolten, D. *Int. J. Hyd. Energ.* **2013**, *38*, 4901–4934.

[64] Puthiyapura, V. K.; Pasupathi, S.; Su, H.; Liu, X.; Pollet, B.; Scott, K. *Int. J. Hyd. Energ.* **2014**, *39*, 1905–1913.

[65] Fujii, K.; Nakamura, S.; Sugiyama, M.; Watanabe, K.; Bagheri, B.; Nakano, Y. *Int. J. Hyd. Energ.* **2013**, *38*, 14424–14432.

[66] Auinger, M.; Katsounaros, I.; Meier, J. C.; Klemm, S. O.; Biedermann, P. U.; Topalov, A. A.; Rohwerder, M.; Mayrhofer, K. J. *Phys. Chem. Chem. Phys.* **2011**, *13*, 16384–16394.

[67] Katsounaros, I.; Meier, J. C.; Klemm, S. O.; Topalov, A. A.; Biedermann, P. U.; Auinger, M.; Mayrhofer, K. J. *Electrochem. Commun.* **2011**, *13*, 634–637.

[68] Steegstra, P.; Ahlberg, E. *Electrochim. Acta* **2012**, *68*, 206–213.

[69] Ooka, H.; Figueiredo, M. C.; Koper, M. T. *Langmuir* **2017**, *33*, 9307–9313.

[70] Bajdich, M.; García-Mota, M.; Vojvodic, A.; Nørskov, J. K.; Bell, A. T. *J. Am. Chem. Soc.* **2013**, *135*, 13521–13530.

[71] Calle-Vallejo, F.; Díaz-Morales, O. A.; Kolb, M. J.; Koper, M. T. *ACS Catal.* **2015**, *5*, 869–873.

[72] Li, H.; Li, Y.; Koper, M. T.; Calle-Vallejo, F. *J. Am. Chem. Soc.* **2014**, *136*, 15694–15701.

[73] Takamatsu, A.; Yamada, I.; Yagi, S.; Ikeno, H. *J. Phys. Chem. C* **2017**, *121*, 28403–28411.

[74] Busch, M.; Ahlberg, E.; Panas, I. *J. Phys. Chem. C* **2012**, *117*, 288–292.

[75] Xu, Z.; Rossmeisl, J.; Kitchin, J. R. *J. Phys. Chem. C* **2015**, *119*, 4827–4833.

[76] Glöckner, C.; Kern, J.; Broser, M.; Zouni, A.; Yachandra, V.; Yano, J. *J. Biol. Chem.* **2013**, *288*, 22607–22620.

[77] Li, Y.; Yamaguchi, A.; Yamamoto, M.; Takai, K.; Nakamura, R. *J. Phys. Chem. C* **2016**, *121*, 2154–2164.

[78] Takashima, T.; Hashimoto, K.; Nakamura, R. *J. Am. Chem. Soc.* **2012**, *134*, 18153–18156.

[79] Yamanaka, K. *Jpn. J. Appl. Phys.* **1989**, *28*, 632.

[80] Kamiya, K.; Hashimoto, K.; Nakanishi, S. *ChemElectroChem* **2014**, *1*, 858–862.

[81] Wonders, A.; Housmans, T.; Rosca, V.; Koper, M. *J. Appl. Electrochem.* **2006**, *36*, 1215–1221.

[82] Jusys, Z.; Massong, H.; Baltruschat, H. *J. Electrochem. Soc.* **1999**, *146*, 1093–1098.

[83] Wang, H.; Löffler, T.; Baltruschat, H. *J. Appl. Electrochem.* **2001**, *31*, 759–765.

[84] Anastasijevic, N.; Baltruschat, H.; Heitbaum, J. *J. Electroanal. Chem.* **1989**, *272*, 89–100.

[85] Frisch, M. J. et al. Gaussian 09, revision D. 01. 2009.

[86] Zhou, X.; Yang, J.; Li, C. *J. Phys. Chem. A* **2012**, *116*, 9985–9995.

[87] Bauernschmitt, R.; Ahlrichs, R. *Chem. Phys. Lett.* **1996**, *256*, 454–464.

[88] Mo, Y.; Stefan, I. C.; Cai, W.-B.; Dong, J.; Carey, P.; Scherson, D. A. *J. Phys. Chem. B* **2002**, *106*, 3681–3686.

[89] Steegstra, P.; Busch, M.; Panas, I.; Ahlberg, E. *J. Phys. Chem. C* **2013**, *117*, 20975–20981.

[90] Laviron, E. *J. Electroanal. Chem.* **1979**, *101*, 19–28.

[91] Castillo-Blum, S. E.; Richens, D. T.; Sykes, A. G. *Inorg. Chem.* **1989**, *28*, 954–960.

[92] Hüppauff, M.; Lengeler, B. *J. Electrochem. Soc.* **1993**, *140*, 598–602.

[93] Casalongue, H. G. S.; Ng, M. L.; Kaya, S.; Friebel, D.; Ogasawara, H.; Nilsson, A. *Angew. Chem. Int. Ed.* **2014**, *28*, 7297–7300.

[94] Sivasankar, N.; Weare, W. W.; Frei, H. *J. Am. Chem. Soc.* **2011**, *133*, 12976–12979.

[95] Nakamura, R.; Nakato, Y. *J. Am. Chem. Soc.* **2004**, *126*, 1290–1298.

[96] Sproviero, E. M. *J. Inorg. Biochem.* **2017**, *171*, 52–66.

[97] Shoji, M.; Isobe, H.; Nakajima, T.; Shigeta, Y.; Suga, M.; Akita, F.; Shen, J.-R.; Yamaguchi, K. *Faraday Disc.* **2016**, *198*, 83–106.

[98] Ping, Y.; Nielsen, R. J.; Goddard III, W. A. *J. Am. Chem. Soc.* **2016**, *139*, 149–155.

[99] Pfeifer, V.; Jones, T. E.; Vélez, J. J. V.; Arrigo, R.; Piccinin, S.; Hävecker, M.; Knop-Gericke, A.; Schlögl, R. *Chem. Sci.* **2017**, *8*, 2143–2149.

[100] Le Formal, F.; Pastor, E.; Tilley, S. D.; Mesa, C. A.; Pendlebury, S. R.; Grätzel, M.; Durrant, J. R. *J. Am. Chem. Soc.* **2015**, *137*, 6629–6637.

[101] Klahr, B.; Hamann, T. *J. Phys. Chem. C* **2014**, *118*, 10393–10399.

[102] Hirai, S.; Yagi, S.; Seno, A.; Ohno, T.; Matsuda, T. *RSC Adv.* **2016**, *6*, 2019–2023.

[103] Hayashi, T.; Yamaguchi, A.; Hashimoto, K.; Nakamura, R. *Chem. Commun.* **2016**, *52*, 13760–13763.

[104] Kucernak, A. R.; Zalitis, C. *J. Phys. Chem. C* **2016**, *120*, 10721–10745.

[105] Conway, B.; Tilak, B. *Electrochim. Acta* **2002**, *47*, 3571–3594.

Chapter 3

Field Effects on Multi-Electron

Transfer

3.1 Introduction

3.1.1 Overview of This Chapter

In this chapter, the author has attempted to understand how the reaction environment affects multi-electron transfer reactions[1,2] by regulating the local pH during the electrochemical reduction of CO_2.[3] CO_2 reduction is currently under intensive investigation as a potential method to produce useful chemicals from atmospheric CO_2.[4–12] If the electrons necessary can be supplied from water *via* the oxygen evolution reaction investigated in Chapter 2, a sustainable chemical process of generating fuels from water and CO_2 can be realized.[13,14] However one of the main challenges in the field of CO_2 reduction is the low selectivity (Faradaic efficiency) due to the simultaneous evolution of hydrogen (HER, hydrogen evolution reaction),[5,15–17] which may occur either through the reduction of protons $(2\,H^+ + 2\,e^- \rightarrow H_2)$ or through the reduction of the solvent molecule itself $(2\,H_2O + 2\,e^- \rightarrow H_2 + 2\,OH^-)$. Although there have been many attempts to enhance the Faradaic efficiency of CO_2 reduction, no study has explicitly differentiated between the two HER pathways. On the other hand, the reaction rate of each HER pathway is affected differently by external factors such as pH,[18] and therefore, the distinction between the two HER pathways is expected to new insight into the selectivity of the electrochemical reaction. Therefore, the author has regulated the local pH at the surface of the working electrode using a Cu rotating disc electrode (RDE) system, and has studied the competition between HER and CO_2 reduction. Through this approach, the author has attempted to showcase the importance of the local reaction environment, such as the local pH, towards regulating multi-electron transfer reactions.

3.1.2   Biodiversity and the Geological Environment

The increasing concentration of atmospheric CO_2, and the positive correlation with mean global temperature is one of the most widely recognized trends concerning the global climate today.[19] There is still debate on whether this trend has been dictated by anthropological activity, or is merely a result of the natural geochemical cycle.[20,21] However, one thing which is clear, is that both the global temperature and the CO_2 concentration are increasing at an unprecedented rate with respect to the timescale of the human species. When *Homo sapiens* first came into existence 200 thousand years ago, the average temperature and CO_2 concentrations were $26°C$[22] and 250 ppm.[23,24] However, in the last 200 years, there has been a 100 ppm increase in the CO_2 concentration,[25] accompanied by a $0.8°C$ increase in the global temperature.[22] These changes are in the order necessary to markedly influence biological processes. For example, although C4 photosynthesis shows a higher energy conversion efficiency compared to C3 photosynthesis under current environmental conditions (CO_2: 380 ppm,[24] $30°C$[22]), C3 photosynthesis becomes more efficient at increased CO_2 concentrations (700 ppm).[24] The lifespan of model organisms such as *Caenorhabditis elegans*[26] and *Drosophila melanogaster*[27] has been known to decrease under high-temperature conditions in the order of several degrees.

Due to the impact of environmental conditions on individuals, a concentration shift in a major component of the global environment has always had drastic consequences towards the biosphere. A prime example may be the great oxygenation event, which was an increase in atmospheric oxygen following the occurrence of oxygenic photosynthesis *ca.* 2.3 billion years ago.[28–30] The transition from an anoxic to oxygenic atmosphere lead to a depletion of electron-rich compounds such as hydrogen or hydrogen sulfides from many environments. These compounds serve as the primary electron donor for many anaerobes today,[31,32] suggesting the atmospheric transition 2.3 billion years ago lead to a depletion of

the primary energy source for anaerobic lifeforms. Furthermore, oxygen is toxic to anaerobic organisms which do not possess methods to harness or neutralize its oxidative potential.[33–35] Therefore, although the newly evolved cyanobacteria possessed an innate advantage by utilizing a larger portion of the solar spectrum, the critical evolutionary factor compared to their ancestors, the anoxygenic photosynthetic bacteria, was their toxic waste, the byproduct "oxygen," which created the space for them to prosper. Needless to say, the accumulation of oxygen would further suppress competing anaerobic lifeforms, effectively cementing their dominance in the biosphere through a positive feedback effect. In this way, the increase in oxygen concentration can be viewed not only as a result, but also as a promoter of oxygenic photosynthesis.

Although we do not typically consider oxygen as a pollutant or a toxin, this is due to our vantage point as a species which relies solely on aerobic respiration as the terminal electron acceptor. Aerobic respiration and the subsequent evolution of the mitochondria can be viewed as a metabolic system which arose to take advantage of the enhanced oxygen concentration.[36] Many of the concepts associated with higher life, such as the organizational and regulatory complexity of eukaryotes, require the increased energy productivity due to aerobic respiration at the mitochondria. For example, eukaryotic cells are on average 1000-fold bigger than typical bacterial or archaeal cells,[37] and possess intracellular compartmentalization which allows for a multitude of reaction environments within one cell.[37–42] In other words, the expanded complexity of life enabled by the evolution of aerobic respiration and the mitochondria came at the expense of the extinction of a multitude of pre-existing anaerobic organisms.

It is possible to consider the cycle of environmental change, and the accompanying extinction and evolution, as a natural part of Earth's history. However, doing so is equivalent to acknowledging that humanity will eventually cease to exist when an environment unsuitable for human habitation finally arrives. Al-

though the human species have managed to adapt to climate change in the past such as the last ice age, the credibility of human survivability is surprisingly small with respect to geochemical timelines. For example, the 300-thousand-year existence of *Homo sapiens* [43] is dwarfed by the 150-million-year reign of the dinosaurs, which subsequently underwent mass extinction 66 million years ago. [44] Although several hypotheses to the direct cause of their extinction can be found in the literature, such as asteroid impacts or an increase in volcanic activity, here again, it is evident that abrupt changes in the climate impose severe risks to all species within the biosphere.

For these reasons, despite the seeming selfishness of this proposition, it is the author's belief that the suppression of abrupt climate changes is in the interest of all inhabitants of the current biosphere, *Homo sapiens* included. Mankind should not forget that he is also but one of the biosphere, and therefore, suppressing climate change is beneficial in terms of biodiversity, not just for endangered species but also for humanity.

To this end, it is important to develop the technology to regulate and neutralize further emissions. Although carbon capture and storage (CCS) technology, which has shown significant advancement in recent years, [45,46] may help curb the increase of CO_2 in the atmosphere, they do not help quench the human need for energy and easily accessible carbon building blocks. As carbon is an integral element in modern human society, it is important to realize a sustainable carbon cycle by developing a method to reduce CO_2, thus closing the carbon cycle which mankind is currently violating by utilizing excess amounts of fossil fuels. It is the author's belief that in the long run, such technology would help prolong the extinction of the human species, regardless of the extent human activity poses towards increased temperature and CO_2 concentrations. The current state of electrochemical CO_2 reduction will be covered in the following section.

3.1.3 Current Status of CO_2 Reduction

There are several methods to reduce CO_2 into useful chemicals. The most energy efficient process available today is the thermochemical reduction of CO_2 using hydrogen or methane (methane dry reforming) as reductants. For example, a combination of the reverse water gas shift (rWGS) reaction($CO_2 + H_2 \rightarrow CO + H_2O$)[47] with a subsequent hydrogenation step *via* Fischer-Tropsch synthesis has been reported to be an efficient methanol production pathway.[48–50] On the other hand, the electrochemical reduction of CO_2 has the advantage of being able to directly use the electrons obtained from water *via* the oxygen evolution reaction. The product distribution is also different, with hydrocarbon gas products such as methane and ethylene being favored over alcohols.[51–54] The insolubility of these products would enhance the efficiency of the total CO_2 reduction process, due to the ease of product separation necessary for downstream processing.

However, one major challenge for CO_2 reduction in aqueous electrolytes is the low selectivity due to the simultaneous evolution of hydrogen *via* the HER,[5,15–17] which may occur either through the reduction of protons ($2\,H^+ + 2\,e^- \rightarrow H_2$) or through the reduction of the solvent molecule itself ($2\,H_2O + 2\,e^- \rightarrow H_2 + 2\,OH^-$). In terms of selectivity, the majority of metal electrodes can be characterized in three categories.[55] The first category consists of metals such as Au[17,56,57] or Ag,[15,57] which selectively produce CO from CO_2. Au, in particular, is known to be highly efficient in producing CO (Faradaic efficiency $> 90\ \%$[57]). The second group consists of materials that primarily evolve hydrogen regardless of the presence of CO_2 such as Pt[57] and Ni.[57] The third group is electrodes that evolve formate ($HCOO^-$) such as Sn.[56,58–61] Out of the many materials studied previously however, metallic copper belongs to none of these groups, as it produces high amounts of hydrocarbons in high faradaic yield.[57]

This trend can be rationalized within the framework of the Sabatier principle based on the adsorption energies of hydrogen and CO_2 reduction intermediates.

For example, Figure 3.1 shows the expected activity of various materials for CO_2 reduction to HCOOH with respect to HER. Materials which are well known to produce formate such as Sn can be found on the top blue region, while Pt and Ni, which favor HER over formate production are indeed predicted to produce hydrogen (bottom right red region). Similar approaches have also been used extensively to rationalize why (specific facets of) Cu is efficient towards CO_2 reduction[62–73] based on the adsorption energies of the intermediates.
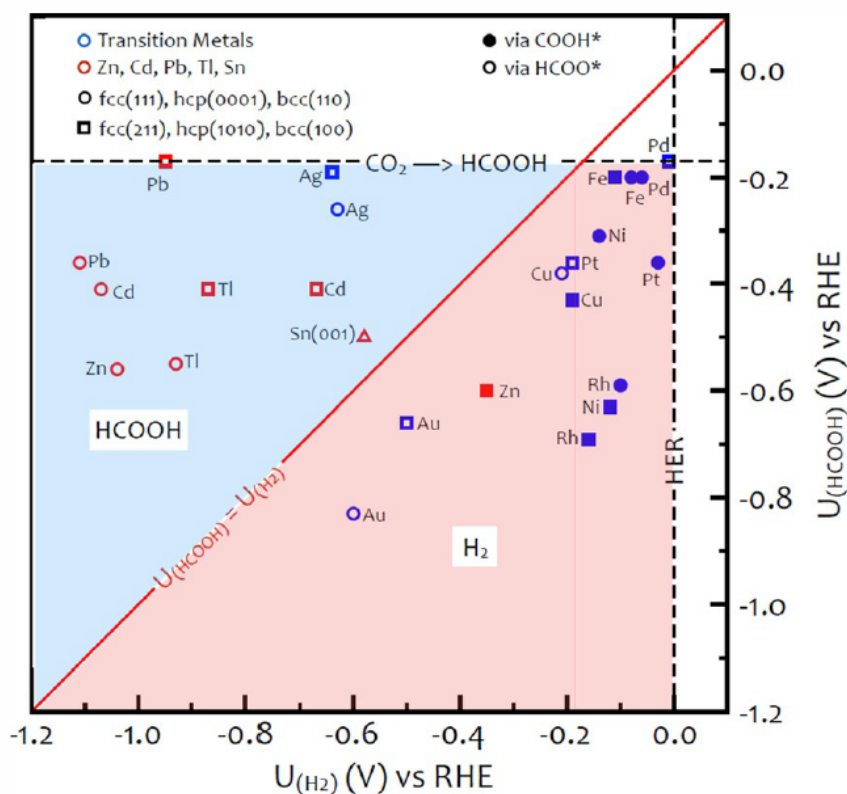
Fig. 3.1 Theoretical activity of various materials towards HER and HCOOH formation from CO_2 reduction. Reproduced from ref. 74 with permission from Wiley. The black dashed lines indicate the thermodynamic potentials for HER and HCOOH generation while the diagonal red line indicates equivalent activity for HER and HCOOH production. Filled and empty symbols indicate that HCOOH is produced *via* the carboxyl (COOH*) and formate (HCOO*) intermediate, respectively.

On the other hand, however, there are also numerous reports which show an increased CO_2 reduction selectivity based on changing the pH, either by using local pH effects[5,15] or by changing the pH of the bulk electrolyte.[75] These effects cannot be explained by the current implementation of the Sabatier principle in electrochemical systems, because the computational hydrogen electrode (CHE) model does not account for changes in the pH (see Chapter 1 for details). Most importantly, it does not account for the two pathways of HER, either from water reduction ($2\,H_2O + 2\,e^- \rightarrow H_2 + 2\,OH^-$) or proton reduction[*1]. They are identical within this framework due to the assumption of a concerted proton–electron transfer in every elementary step, meaning that pH is not an explicit parameter in the model (see Chapter 1 for details). In reality, however, water reduction is expected to become favored over proton reduction at low proton concentrations. This effect may become relevant even in acidic electrolytes because the local proton concentration at cathodes decreases during HER[76] and CO_2 reduction due to slow mass transport.[77–79] The onset potential and kinetics of the two HER pathways may also show different pH dependences.[18,80,81] Differentiating the proton source is especially important to discuss the competition of HER and CO_2 reduction, because CO_2 may interact with the two HER pathways differently. Furthermore, CO_2 may act as or form pH buffers,[77,78] adsorbates,[62] and proton donor/acceptors[82,83] during the reaction, all of which may show different effects depending on the HER pathway. Therefore, it is important to study the competition of CO_2 reduction and the two pathways of HER by explicitly taking into account the effect of mass transport and local pH at the electrode.[77,78]

[*1] Although the actual state of the proton or proton donor may be more complex, here, the notation "proton" refers collectively to all species which can be considered as solvated forms of a hydrogen nucleus. The term "proton reduction" here refers to hydrogen evolution from acidic media showing a direct dependence on proton concentration, and "water reduction" refers to hydrogen evolution independent of proton concentration.

3.1.4 Rotating Disc Electrode Theory

In this section, the theory behind voltammograms obtained using rotating disc electrodes (RDE) will be explained briefly. The mathematical theory presented here will provide the basis for the assignment of voltammetric features presented in the results section (section 3.4).

The main advantage of the RDE system is the extent of regulation one has over diffusion processes.[84] The forced convection obtained by rotating the electrode allows the diffusion flux of chemical species to be regulated explicitly. In the purpose of this study, as one reactant (water molecules) are in abundance compared to another (protons), identifying the occurrence of diffusion-limiting currents allows differentiation of reaction pathways which rely on one species over the other.

The reaction rate of a diffusion-limited process can be modeled mathematically by assuming a steady state. This assumption can be confirmed experimentally if the hysteresis between the anodic and cathodic scans of the voltammogram is negligible. Under this condition, the general equation for a flux of a given species (J) can be expressed as:

$$J = -\nabla C - \frac{zF}{RT}DC\nabla\phi + Cv \qquad (3.1)$$

Here, C and z represent the concentration and charge of said species, while F, R, T represent the Faraday constant, gas constant, and absolute temperature. ϕ indicates the electrical field, and v indicates the velocity vector. The three terms represent diffusion, migration, and convection respectively, and for electrochemical systems with sufficient supporting electrolyte ions, the second migration term can be neglected. The RDE system manipulates the velocity vector v, and based on hydrodynamic theory,[84,85] the velocity perpendicular to the electrode surface

$v_\perp$ can be expressed as:

$$v_\perp = 0.51 \ \omega^{1.5}\nu^{-0.5}ry \tag{3.2}$$

where ω indicates angular velocity, ν indicates kinematic viscosity of the solvent, r indicates the distance from the rotation center, and y indicates the distance from the electrode surface. Although transient currents will show a decrease similar to the case of stationary electrodes, it is due to the contribution from the third term in Equation 3.1 that the current does not decay toward zero, but instead to a steady-state value. Under such conditions where mass transport is the limiting factor of electron transfer rates, $C\mid_{y \to 0} = 0$, leading to the following expression:

$$v_\perp \frac{\partial C_b}{\partial y} = D\frac{\partial^2 C_b}{\partial y^2} \tag{3.3}$$

where C_b indicates the concentration (C) at the bulk solution $(y \to \infty)$. The solution of this differential equation yields:

$$C_b = (\frac{\partial C_b}{\partial y})_{y=0} \ 0.8934 \ (\frac{3D\omega^{-1.5}\nu^{0.5}}{0.51})^{1/3} \tag{3.4}$$

Under mass transport limiting conditions, the current is dependent only on the flux at the electrode surface $(\frac{\partial C_b}{\partial y})$ and not the electrode potential. Therefore, the limiting current $(j_{\lim})$ can be expressed as:

$$j_{\lim} = nFD(\frac{\partial C_b}{\partial y})_{y=0} = 0.62nFD^{2/3}\omega^{1/2}\nu^{-1/6}C_b \tag{3.5}$$

which is now commonly known as the Levich equation. This equation predicts that the limiting current density is proportional to the bulk concentration (C_b) and the square root of the rotation rate $(\omega^{1/2})$. This will be the diagnosis of whether a reactant is limited by mass transport or not. The diffusion layer

thickness δ under these conditions is given by:

$$\delta = 1.61 D^{1/3} \omega^{-1/2} \nu^{-1/6} \tag{3.6}$$

When the current is not limited by mass transport ($C_s > 0$, with C_s indicating the concentration at the electrode surface), the solution of equation 3.3 becomes:

$$j = 0.62 \; nFD^{2/3} \omega^{1/2} \nu^{-1/6} [C_b - C_s] \tag{3.7}$$

Therefore, in combination with the Levich equation (Equation 3.5), the current density can be expressed in general as:

$$j = j_{\lim}[\frac{C_b - C_s}{C_b}] = \frac{nFD[C_b - C_s]}{\delta} \tag{3.8}$$

Under conditions where the electron transfer is sufficiently slow such that the reverse reaction can be neglected, the disk current can be expressed as:

$$j = nFk_f(U)C_s = nFk_f(U)C_b(1 - \frac{j}{j_{\lim}}) \tag{3.9}$$

Here, $k_f(U)$ denotes the forward rate constant. Specifically when the effect of mass transport is minimal ($j \ll j_{\lim}$),

$$j = nFk_f(U)C_s = nFk_f(U)C_b \tag{3.10}$$

By defining this current as j_K, one obtains the Koutecký-Levich equation:

$$\frac{1}{j} = \frac{1}{j_K} + \frac{1}{j_{\lim}} = \frac{1}{j_K} + \frac{\omega^{1/2}}{0.62nFD^{2/3}\nu^{-1/6}C_b} \tag{3.11}$$

95

which can be rearranged as:

$$j = \frac{j_{\lim}}{1 + j_{\lim}/j_K} \tag{3.12}$$

Therefore, j exhibits a $j_{\lim}$ (rotation rate) dependence as shown in Figure 3.2. Based on the Koutecký-Levich equation, when the electron transfer kinetics are sufficiently fast compared to the mass transport flux ($j_K \gg j_{\lim}$), $j \rightarrow j_{\lim}$. On the other hand, when the electron transfer kinetics are much slower than mass transport, ($j_K \ll j_{\lim}$), $j \rightarrow j_K$. Based on the Koutecký-Levich equation (Equation 3.11), a plot of $1/j$ vs. $1/\omega^{1/2}$ will yield a linear plot which can be extrapolated to $\omega \rightarrow 0$ to yield j_K. Therefore, the Koutecký-Levich plot generated in this manner will allow kinetic parameters such as k_f to be obtained experimentally, giving insight into the mechanism.
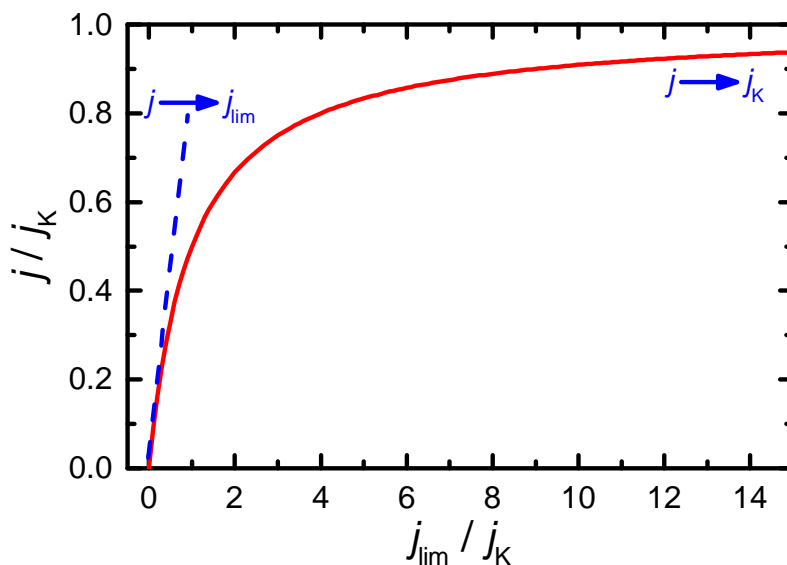
Fig. 3.2 Graphical representation of the Koutecký-Levich equation.

3.2 Objective

The objective of the work presented here is to understand the role of the local pH on the competition of HER (both proton reduction and water reduction) with respect to CO_2 reduction (Figure 3.3). As the proton concentration (pH) at the electrode affects only the proton reduction pathway of HER, regulating the mass transport flux of protons using a RDE system allows differentiation between the two HER pathways. Based on this differentiation, the author has attempted to study the interaction of each HER pathway with CO_2. Additionally, as the local pH near the electrode was found to change during the voltammetric scans, the voltammograms which were mathematically corrected for local pH changes during the measurement will be presented. Through this approach, the author has attempted to establish the importance of the reaction environment (pH) in multi-electron transfer reactions, and to provide deeper insight into the competition between CO_2 reduction and HER.
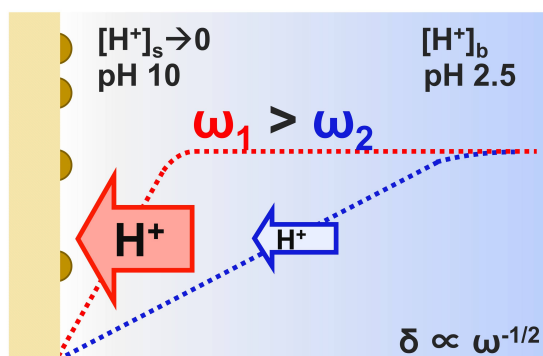
Fig. 3.3 A schematic illustration showing the concept of this work. An RDE system was employed to explicitly regulate the proton diffusion flux and the local pH at the electrode.

3.3 Materials and Methods

3.3.1 Electrochemistry

All electrolytes were prepared using HPLC (= 99.0 %) grade sodium perchlorate monohydrate (Fluka, 7791-07-3) and 60 wt% perchloric acid (Merck, 7601-90-3), which were used without further purification. A phosphate stock solution (pH 2.5, total concentration of phosphate ions: 10 M) was made from NaH_2PO_4 · H_2O (Merck, 10049-21-5) and H_3PO_4 (Merck, 7664-38-2), and was diluted as necessary with the perchlorate solution to yield an electrolyte with the desired buffer concentration. The HCHO used (Sigma-Aldrich, 50-00-0) contained *ca.* 10–15 wt% CH_3OH as a stabilizing agent. All electrolytes were bubbled with the appropriate gas (Ar, CO, or CO_2) 30 mins prior to the electrochemical measurement. The pH change due to switching from Ar atmosphere to CO_2 is negligible, based on pH meter readings (ΔpH < 0.05) and the identical height of the diffusion plateau of HER during cyclic voltammetry. The pH value of 2.5 was intentionally chosen because the proton concentration is high enough to ensure the pH does not change upon CO_2 bubbling, but low enough that the diffusion plateau can be observed at low current densities. The reference and counter electrodes were a commercial RHE (Gaskatel Hydroflex) and platinum wire respectively, with the exception of the Fourier-transform infrared (FTIR) measurements where an Ag/AgCl sat. reference electrode was employed due to the cell configuration. All potentials are reported versus the RHE. Ohmic resistance was compensated during cyclic voltammetry using the IVIUM potentiostat software (Ivium Soft), and after the measurements for the FTIR measurements.

3.3.2 Electrode Preparation

The Cu RDE was polished to a mirror finish using alumina paste (1.0 μm, 0.3 μm, 0.05 μm) and then sonicated before use. The Cu thin film used for the FTIR measurements was deposited on the silicon prism *via* sputtering and was used without further cleaning. No electropolishing was conducted in any of the experiments.

3.3.3 FTIR Measurements

The FTIR measurements were performed with a Bruker Vertex 80 V IR spectrophotometer with an mercury–cadmium–telluride (MCT) detector and p-polarized light in the external reflection configuration. The spectra correspond to an average of 100 scans with 8 cm^{-1} resolution, and used p-polarized light.

3.4 Results and Discussion

3.4.1 Effect of Local pH on the Selectivity of CO_2 Reduction

The cyclic voltammograms of a polycrystalline Cu RDE measured in an Ar-saturated 0.1 M $NaClO_4$ electrolyte (pH 2.5) is shown in Figure 3.4. Under unbuffered conditions, (black lines), two redox features can be observed. The first reduction current to be observed during the cathodic potential scan increases from *ca.* -0.5 V vs. RHE (reversible hydrogen electrode, all potentials in this chapter will be referred to this reference electrode) and exhibits a plateau current which is dependent on the rotation rate (mass transport). Due to the inertness of the electrolyte (Ar-saturated $NaClO_4$), it can be expected that the redox-active species exhibiting mass transport limitation is protons. Therefore, this current was ascribed to HER from proton reduction, where the notation "proton" refers collectively to all chemical species which can be considered solvated forms of a hydrogen/proton nucleus. On the other hand, a second reduction current was observed at potentials more negative -1.2 V. This second current was assigned to HER from water reduction, due to its independence from mass transport.

The assignment of this current is supported by the cyclic voltammograms in buffered conditions (red lines). Upon the addition of 10 mM phosphate, the plateau current was split into two plateaus, with a higher plateau current at potentials more negative than *ca.* -1.0 V. This is consistent with a local pH change due to mass transport limitation of protons, because when the pH at the electrode surface becomes more alkaline than the pK_{a2} of phosphate (7.2), the phosphate species at the electrode are deprotonated to form HPO_4^- species. This allows the transport of $H_2PO_4^-$ from the bulk electrolyte to make an additional contribution to the total proton flux, generating a step-like feature in the plateau current.
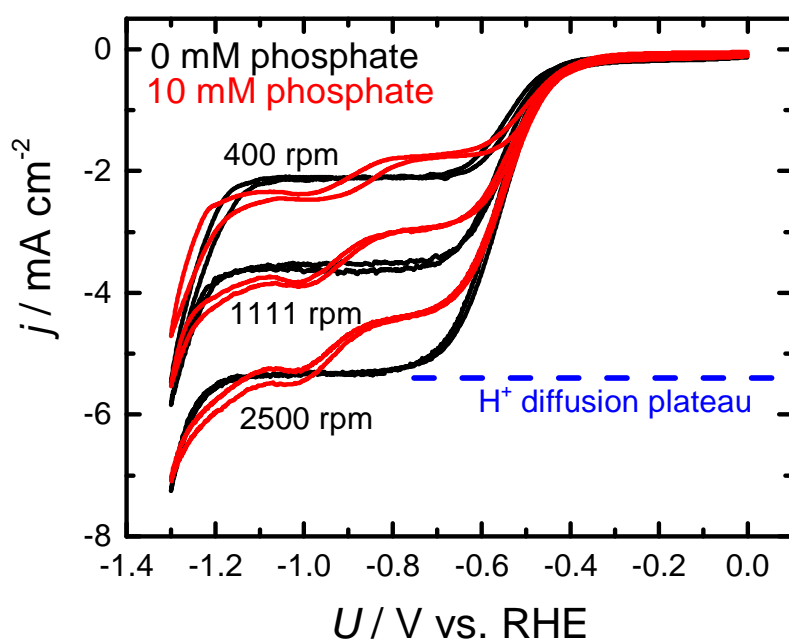
Fig. 3.4 Cyclic voltammograms of a polycrystalline Cu RDE in an Ar-saturated 0.1 M NaClO$_4$ electrolyte. Red: 10 mM phosphate, black: un-buffered. The smaller plateau current at $U > -0.8$ V is due to the slight increase of pH upon buffer addition. Numbers indicate the rotation rate of the RDE [unit: rotations per minute (rpm)]. Scan rate: 50 mV/s.

In order to obtain direct evidence into the assignment of the current, the rotation-rate-dependence and the pH-dependence of the plateau current were studied. Figure 3.5 shows the Levich plot of the plateau current in 0.1 M NaClO$_4$ (pH 2.5). The linear relationship between the plateau current and the square root of the rotation rate indicates an electron transfer process which is fully dictated by mass transport (Equation 3.5).

Therefore, according to the Levich equation (Equation 3.5), the concentration of the redox-active species should influence the plateau current linearly. Figure 3.6 shows the pH dependence of the cyclic voltammograms measured between pH 2.0 and 3.0. The plateau current obtained from these measurements exhibited a linear relationship with the proton concentration as shown in the inset, providing evidence that the plateau current can be ascribed to proton reduction ($2\,\mathrm{H^+} + 2\,\mathrm{e^-} \rightarrow \mathrm{H_2}$).
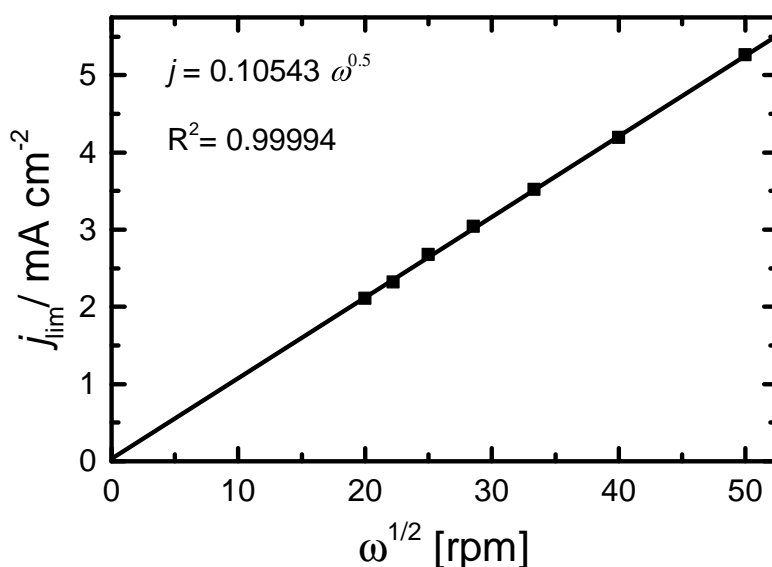
Fig. 3.5 Rotation rate dependence of the plateau current (j_{lim}) in a 0.1 M NaClO$_4$ solution (pH 2.5) under Ar-saturated conditions.
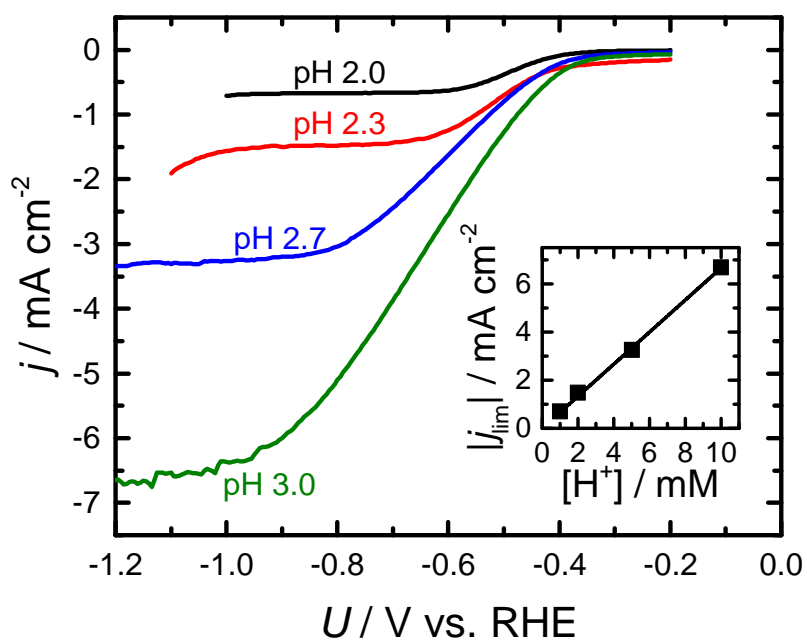
Fig. 3.6 Cyclic voltammograms of a polycrystalline Cu RDE (400 rpm) measured at different pH in Ar-saturated, unbuffered 0.1 M NaClO$_4$ solutions. Inset shows the relationship between proton concentration and the plateau current. Scan rate: 50 mV/s. The ohmic drop was not compensated in this figure.

Based on this assignment, the transition of the HER pathway from proton reduction to water reduction in Figure 3.4 occurs at *ca.* $-5.6 \, \text{mA cm}^{-2}$ at 2500 rpm, where the mass transport of protons becomes insufficient. However, the limiting current is linearly proportional to the concentration of protons (Figure 3.6, Equation 3.5), and therefore, the water reduction pathway will become increasingly important in more alkaline conditions. For example, the limiting current of protons at pH 7 can be calculated as *ca.* $0.2 \, \mu\text{A cm}^{-2}$ even at 2500 rpm, indicating the majority of the hydrogen detected in studies using stationary electrodes in neutral or alkaline electrolytes are likely to be derived from water reduction. It is important to note that the proton reduction pathway of HER is inhibited due to mass transport limitations and local pH effects, even in the presence of a buffer as shown in Figure 3.4. Such an effect is not unique to phosphate, but is expected to occur with other buffer molecules such as bicarbonate species, as will be discussed later in this chapter.

In order to evaluate the competition between the CO_2 reduction and the two pathways of HER, electrochemical measurements were conducted in a CO_2-saturated electrolyte. Figure 3.7 shows the cyclic voltammograms measured in a CO_2-saturated 0.1 M $NaClO_4$ electrolyte (pH 2.5) at different values of the disc rotation rate. Compared to the Ar-saturated solution (black lines), a slight negative shift of the onset for proton reduction current can be seen. However, a more pronounced suppression of the HER current is observed below -1.2 V, indicating CO_2 interferes with the water reduction pathway more significantly than the proton reduction pathway. This suppression in activity is not due to impurities in the electrolyte, as it does not occur in Ar atmosphere. Buffering effects are also minimal, as no increase in proton flux could be observed, even when the pH at the electrode surface becomes more alkaline than the pK_{a1} of H_2CO_3 (3.6). This is due to the low buffer capacity arising from the low solubility of CO_2 in acidic solutions, as will be explained later quantitatively.
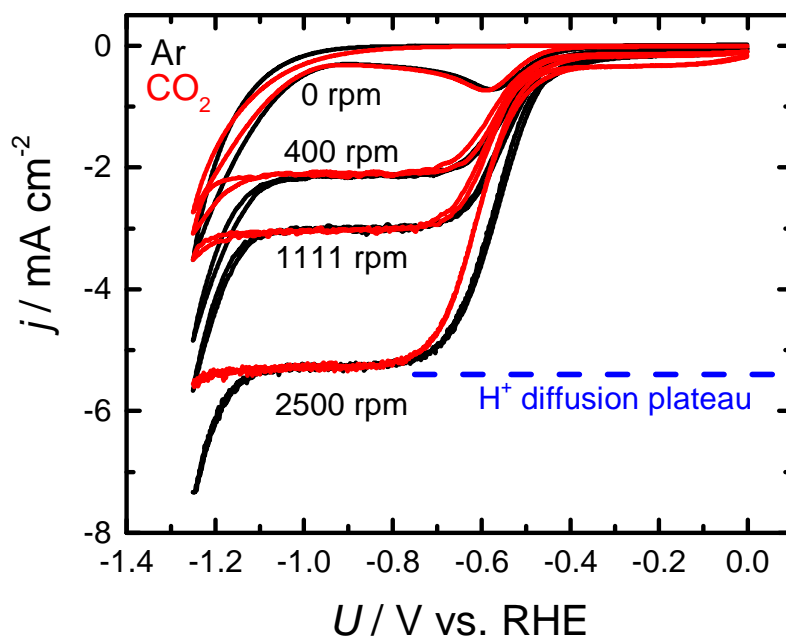
Fig. 3.7 Cyclic voltammograms of a polycrystalline Cu RDE in an un-buffered 0.1 M $NaClO_4$ electrolyte (pH 2.5). Red: CO_2 atmosphere, black: Ar atmosphere. No bulk pH change was observed upon CO_2 saturation as can be seen from the identical height of the limiting current. Numbers indicate the rotation rate of the RDE [unit: rotations per minute (rpm)]. Scan rate: 50 mV/s.

These results highlight the importance of surface pH effects, because without the change of local pH, proton reduction is expected to remain dominant even in the presence of CO_2. As shown in Table 3.1, in addition to having a smaller overpotential compared to water reduction, proton reduction is not inhibited by the presence of CO_2. Therefore, the main reason proton reduction does not become the dominant reaction is the lack of substrates, which occurs due to the change of local pH and the slow kinetics of proton mass transport.

Table 3.1   Competition of the two pathways of HER with CO_2 reduction.

Reaction Pathway	Onset Potential	Mass Transport	CO_2
Proton Reduction	-0.5 V	Limited	Independent
Water Reduction	-1.2 V	Independent	Inhibited

3.4.2 Origin of the Inhibitory Effect

In order to gain insight into the chemical origin of the species which inhibits water reduction selectively, cyclic voltammograms were measured in an electrolyte solution saturated with CO (Figure 3.8). CO is the two-electron reduction product of CO_2, and has previously been proposed to be the inhibitor for HER.[62,86,87] In accord with past reports, Figure 3.8 also shows that adsorbed CO inhibits HER significantly. However, similar to the case with CO_2, the proton reduction pathway was less sensitive to inhibition compared to water reduction. The different interaction between the two pathways of HER with CO_2 reduction further emphasizes the importance of explicitly distinguishing the substrate molecule for HER in order to understand the competition of CO_2 reduction with HER.
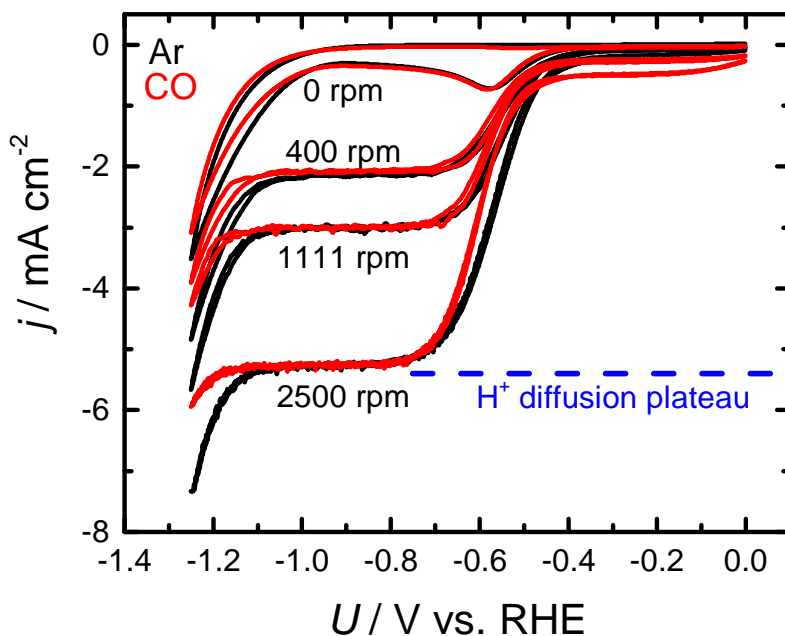
Fig. 3.8 Cyclic voltammograms of a polycrystalline Cu RDE in an unbuffered 0.1 M $NaClO_4$ electrolyte (pH 2.5). Red: CO atmosphere, black: Ar atmosphere. Numbers indicate the rotation rate of the RDE [unit: rotations per minute (rpm)]. Scan rate: 50 mV/s.

Interestingly, further reduced forms of CO_2 such as HCHO and CH_3OH showed minimal inhibitory effects as can be seen in Figure 3.9. Although HCHO has been reported to undergo hydration to generate methanediol,[88–92] these results nonetheless show that excessively reduced adsorbates are not responsible for the inhibitory effects of CO_2 or CO towards water reduction. Taken together, these observations suggest the selective inhibitory effect is due primarily to CO adsorbed on the surface of Cu.
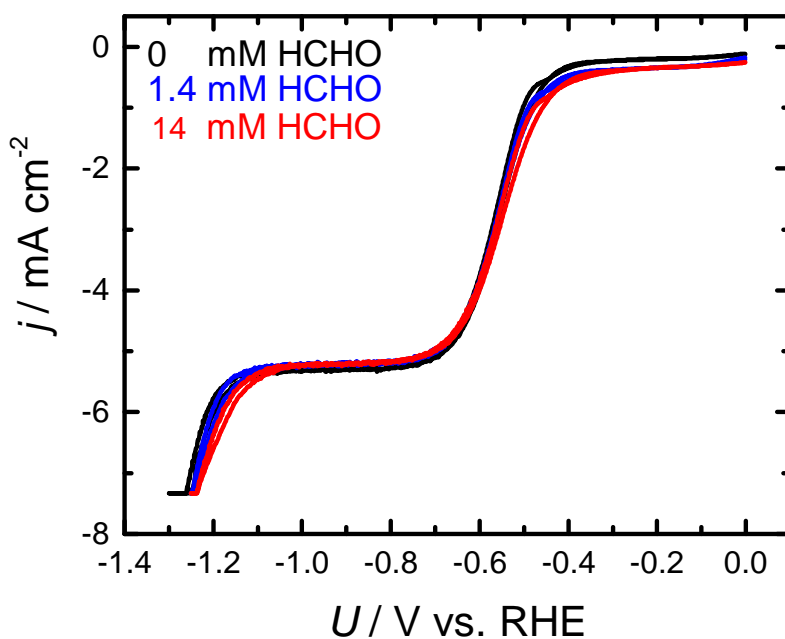
Fig. 3.9 Cyclic voltammograms of a polycrystalline Cu RDE in an Ar-saturated, unbuffered 0.1 M $NaClO_4$ electrolyte (pH 2.5) in the presence of various concentrations of HCHO. Rotation rate: 2500 rpm. Scan rate: 50 mV/s.

Further support that water reduction is inhibited by CO generated from CO_2 can be found in Figure 3.10, which shows the rotation rate dependence of HER inhibition. In order to evaluate the extent of inhibition due to the coexistence of CO or CO_2, the limiting current of proton reduction was subtracted from the total current. As the proton reduction rate is dictated by mass transport at potentials where water reduction is initiated ($U < -1.2$ V), subtracting this limiting current from the total reduction current is expected to express the sum of the reaction rates for water reduction and CO_2 (or CO) reduction. If the CO or CO_2 reduction current is negligible, comparing the subtracted reduction current in CO or CO_2 atmosphere to that in Ar atmosphere would allow quantitative evaluation of water reduction inhibition due to CO or CO_2. As shown in Figure 3.10, in both CO_2 and CO, water reduction is inhibited drastically from 0 to 500 rpm, whereas higher rotation rates have a less significant effect. The strong inhibition at low rotation rates ($\omega < 500$ rpm) is most likely due to the increased coverage of CO on the Cu surface due to efficient transport of CO and CO_2. The saturation of inhibition at higher rotation rates may be due to the CO coverage reaching a constant value. The higher current density in CO-saturated electrolytes may be due to a difference in the CO coverage as a result of the difference in solubilities of CO_2 and CO in water.
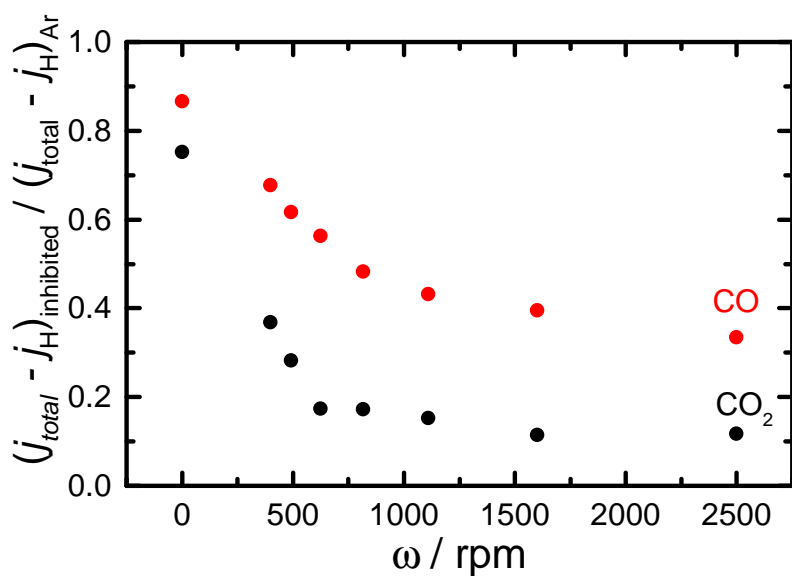
Fig. 3.10 Rotation rate dependence of the inhibition of water reduction from CO_2 (black) and CO (red). The y-axis represents the rate of water reduction in each atmosphere, normalized by that in an Ar atmosphere. A lower value on the y-axis implies a stronger inhibition. Current density values were obtained at -1.25 V vs. RHE.

In order to obtain direct evidence that the inhibitory effect of CO_2 reduction on water reduction is due to the adsorbed CO, *in-situ* FTIR spectra were measured in an attenuated total reflection infrared (ATR-IR) configuration (Figure 3.11). When the spectrum at 0 V was used as the reference, the intensity of the IR band at *ca.* 2050 cm^{-1}, assignable to adsorbed CO (CO_{ads}),[87] increases from -0.8 V during the negative potential step. Although CO is known to be further reduced on Cu electrodes at negative potentials,[57,93] the potential independence of the CO band intensity at water reduction potentials ($U < -1.21$ V) indicates that the CO coverage is also constant, suggesting inhibitory interactions such as site blocking or binding energy shifts of hydrogen[6] are possible. On the other hand, no CO_{ads} was detected at potentials more postive than -0.8 V, suggesting the CO coverage is insufficient to have a significant inhibitory influence on proton reduction. It is noteworthy that during this measurement, IR bands which resemble bicarbonate[94] were observed at 1435 and 1280 cm^{-1} at potentials more negative than -0.9 V (Figure 3.12), in accord with the depletion of protons at the electrode surface.
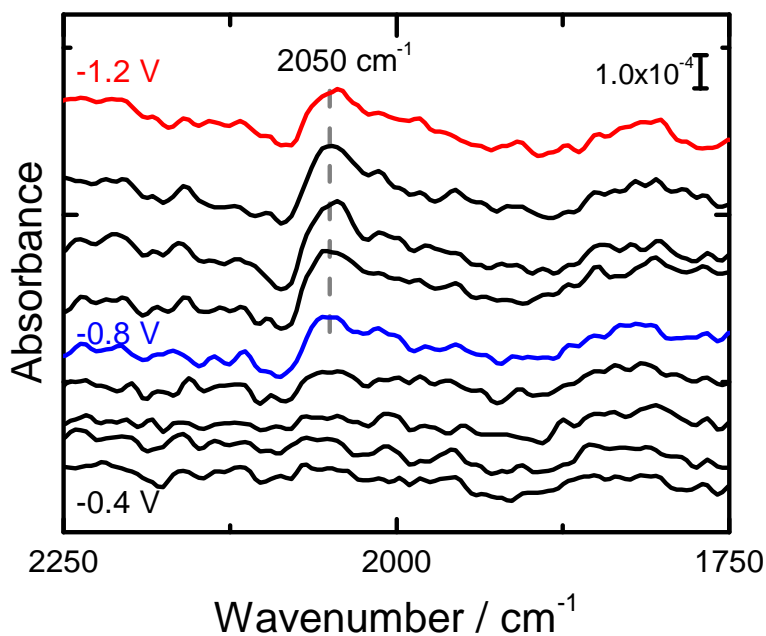
Fig. 3.11   FTIR spectra of a polycrystalline Cu electrode in 0.1 M NaClO$_4$ (pH 2.5). The reference spectrum was measured at 0 V, after saturating the solution with CO$_2$ for 30 minutes. Spectra are shown from -0.4 V to -1.2 V in 0.1 V intervals.
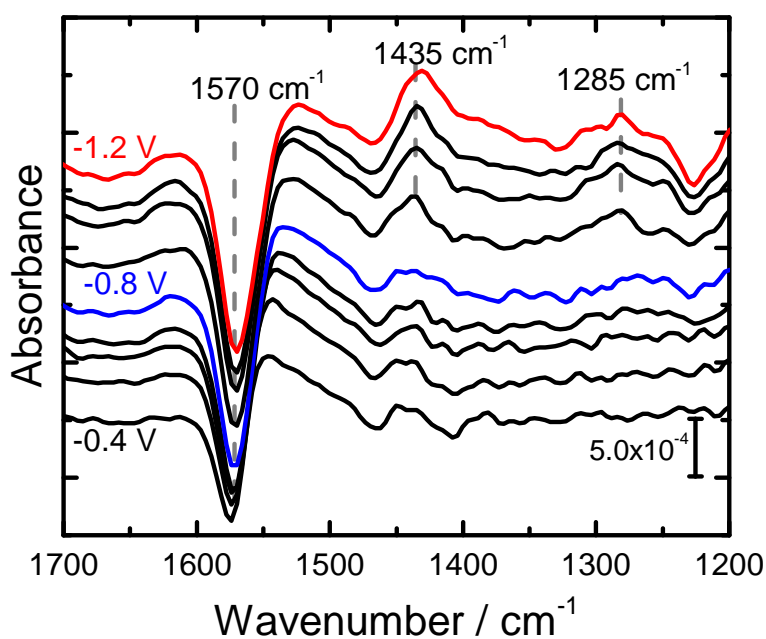
Fig. 3.12   FTIR spectra of a polycrystalline Cu electrode in the wavenumber region for perchlorate (1570 cm^{-1}), bicarbonate (1435 cm^{-1}), and carbonate (1285 cm^{-1}) adsorption. Spectra were measured under the same condition as in Figure 3.11.

Based on the combination of electrochemistry and spectroscopy, water reduction was found to be suppressed due to adsorbed CO, thus increasing the selectivity for CO_2 reduction. Copper has long been known to interact favorably with CO in the context of CO_2 reduction based on theoretical[63] and experimental[75,95,96] observations which show that CO can adsorb and desorb on Cu efficiently. However, no previous study has explicitly differentiated between the two HER pathways, which exhibit marked differences in terms of apparent onset potentials (Figures 3.4–3.8) and interaction with adsorbed CO (Figure 3.11). The clarification of the HER pathway which is inhibited by CO_{ads} is new insight into the competition of CO_2 reduction with HER, which may assist future catalyst development.

3.4.3   Mathematical Modeling

The differentiation between proton reduction and water reduction explained in the previous chapter was based on the difference in interaction with CO and the overpotential observed experimentally. However, due to changes in the local pH, the overpotential depicted for example in Figure 3.7 does not reflect the true kinetic barriers of each HER pathway. The slow kinetics of proton mass transport with respect to its consumption *via* HER generates a discrepancy between the pH at the surface of the working electrode and the bulk electrolyte. The increase of pH due to the depletion of protons at the surface of the electrode would lead to an overestimation of the overpotential on the RHE scale, especially for water reduction where the diffusion of protons is already mass transport limited. However, the RDE system allows precise control of the mass transport flux, which further allows quantitative estimations of the surface pH. For example, the local pH at -0.8 V can be estimated to be *ca.* 4.5, because the HER current density of proton reduction corresponds to 99 % of the limiting current. Based on Equation 3.7, this indicates that the proton concentration at the electrode surface must be 1 % of the bulk electrolyte (pH 2.5). In this section, the local pH at the electrode will be evaluated mathematically based on the RDE theory[76–78] presented in the introduction of this chapter in order to evaluate the true activation barriers of the two HER pathways.

As Auinger *et al.* have shown,[76] the amount of protons consumed and hydroxide ions generated from the HER corresponds to the mass transport flux of each ion under steady-state conditions. Therefore, the total current density (j_{total}) can be expressed using the mass transport fluxes of H$^+$ (J_{H}) and OH$^-$ (J_{OH}) as follows:

$$j_{\text{total}} = F(J_{\text{H}}\mid_{x\to 0} - J_{\text{OH}}\mid_{x\to 0}) \tag{3.13}$$

$$= -FD_{\text{H}}\frac{[H]_b - [H]_s}{\delta_{\text{H}}} + FD_{\text{OH}}\frac{[OH]_b - [OH]_s}{\delta_{\text{OH}}} \tag{3.14}$$

114

where x is the distance from the electrode, F is the Faraday constant, $[X]$ is the concentration of X, D_X is the diffusion coefficient, and δ_X is the thickness of the diffusion layer. Subscripts b and s denote bulk and surface values, and subscripts H and OH stand for protons and hydroxyl ions, respectively. δ_H and δ_{OH} show a rotation rate dependence as determined by the Levich equation (Equation 3.5). Normalizing j_{total} by the absolute value of the proton limiting current density:

$$| j_{\lim} | = F D_H \frac{[H]_b}{\delta_H} \tag{3.15}$$

yields a rotation-rate independent representation of the HER current:

$$\frac{j_{total}}{| j_{\lim} |} = -\frac{[H]_b - [H]_s}{[H]_b} + \frac{D_{OH}\delta_H}{D_H\delta_{OH}} \frac{[OH]_b - [OH]_s}{[H]_b} \tag{3.16}$$

Finally, the hydroxide ion concentrations can be substituted using the proton concentrations and the water dissociation constant K_w by assuming the water hydrolysis equilibrium ($[H] \times [OH] = K_w$). Therefore, the local proton concentration at the electrode can be expressed as:

$$[H]_s = \frac{1}{2}(-\alpha + \sqrt{\alpha^2 + 4(\frac{D_{OH}\delta_H}{D_H\delta_{OH}})K_w}) \tag{3.17}$$

where

$$\alpha = -[H]_b + \frac{D_{OH}\delta_H}{D_H\delta_{OH}} \frac{K_w}{[H]_b} - \frac{j_{total}}{| j_{\lim} |}[H]_b \tag{3.18}$$

Equation 3.17 allows the surface pH to be estimated based on the normalized current density $\frac{j_{\text{total}}}{|j_{\text{lim}}|}$. It is important to emphasize that the surface pH is not a function of the raw rotation rate, but the current density normalized by the limiting current $\frac{j_{\text{total}}}{|j_{\text{lim}}|}$. This is because the local pH is dictated based on the balance of the consumption and transport of protons, which are represented by j_{total} and j_{lim}, respectively. Therefore, the normalized current density $\frac{j_{\text{total}}}{|j_{\text{lim}}|}$ can also be interpreted as a normalized rotation rate, which is a quantitative representation of the ratio between proton supply and consumption.

Figure 3.13 shows the results of the modeling based on Equation 3.16. A drastic increase in the pH from 4 to 10 can be observed when the current density approaches the limiting current. The decrease of the proton concentration by 6 orders of magnitude in a narrow current range indicates the extent of mass transport limitations on the proton reduction pathway. This pH change is sufficient to deprotonate carbonic acid to bicarbonate and carbonate ions, indicating CO_2 may act as a buffer molecule, even in unbuffered electrolytes.
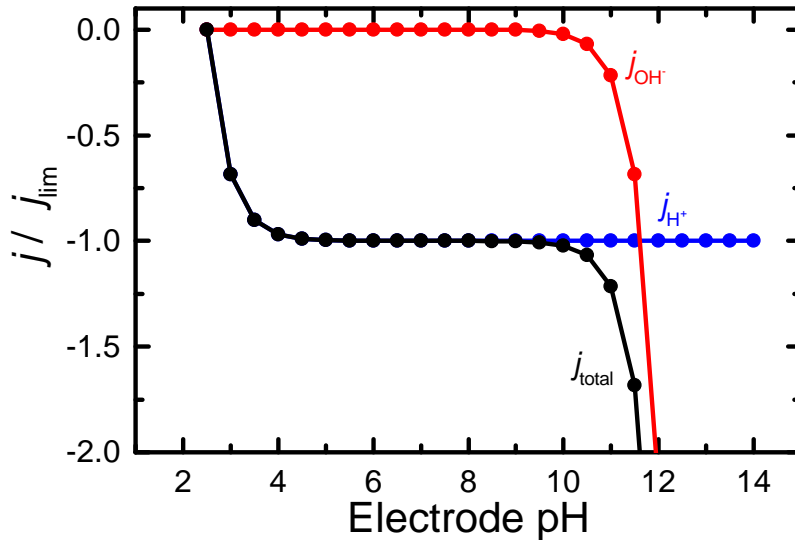
Fig. 3.13 Graphical representation of Equation 3.16. Red and blue lines indicate the first and second terms of Equation 3.16. Their total is shown in black. The diffusion layer thicknesses were obtained from the Levich equation (Equation 3.5) using a kinematic viscosity of 1 cm^2/s, $D_H = 9.31 \times 10^{-5}$ [cm^2/s], and $D_{OH} = 5.27 \times 10^{-5}$ [cm^2/s].[76]

In order to take into account the buffering effects of CO_2, the local pH of buffered solutions was modeled using a similar approach to the one above. Assuming a buffer ion with the acid-base equilibrium ($HA \rightarrow H^+ + A^-$, equilibrium constant: K_a), the difference between bulk pH and surface pH can be suppressed because the flux of buffer molecules makes an additional contribution to the net proton flux. The current density in a buffered solution is given by:

$$j_{\text{total}} = F(J_H \mid_{x \rightarrow 0} - J_{\text{OH}} \mid_{x \rightarrow 0} - J_A \mid_{x \rightarrow 0}) \tag{3.19}$$

Under steady state conditions, the flux of buffer molecules must meet the following equation:

$$J_{\text{HA}} \mid_{x \rightarrow 0} + J_A \mid_{x \rightarrow 0} = 0 \tag{3.20}$$

which is equivalent to:

$$D_{\text{HA}} \frac{[HA]_b - [HA]_s)}{\delta_{\text{HA}}} = -D_A \frac{[A]_b - [A]_s}{\delta_A} \tag{3.21}$$

By considering the acid–base equilibrium between HA and A^-, this leads to the following solution for $[A]_s$:

$$[A]_s = \frac{\beta[H]_b + 1}{\beta[H]_s + 1} [A]_b \tag{3.22}$$

where

$$\beta = \frac{D_{\text{HA}}}{D_A} \frac{\delta_A}{\delta_{\text{HA}}} \frac{1}{K_a} \tag{3.23}$$

Therefore, the normalized current density in a buffered solution can be expressed as:

$$\frac{j_{\text{total}}}{\mid j_{\text{lim}} \mid} = -\frac{[H]_b - [H]_s}{[H]_b} + \frac{D_{\text{OH}}\delta_H}{D_H\delta_{\text{OH}}} \frac{[OH]_b - [OH]_s}{[H]_b} + \frac{D_A\delta_H}{D_H\delta_A} \frac{[A]_b - [A]_s}{[H]_b} \tag{3.24}$$

where the third term indicates the contribution from the buffer component. By comparison with Equation 3.16, it becomes apparent that the buffering effect is linearly proportional to the concentration of the buffer molecule.

Figure 3.14 shows the numerical solution to Equation 3.24 at various buffer concentrations, assuming a bulk pH of 2.5 and using the diffusion constants of CO_2 and HCO_3^- for the diffusion constants of the protonated and deprotonated forms of buffer molecule. At low buffer concentrations (panel A), the voltammogram is almost identical with the unbuffered case, because the contribution of the third term in Equation 3.24 is negligible. However, upon increasing the buffer concentration, the buffer molecule makes a noticeable contribution as indicated by the step in the limiting current when the surface pH is larger than the pK_a (panels B and C). As seen experimentally in Figure 3.4, this is because the protonated buffer molecules in the bulk electrolyte will deprotonate in the high pH environment at the surface of the electrode, effectively increasing the mass transport flux. This qualitative argument can be understood quantitatively by comparing the first and third terms (proton transport from proton flux and buffer flux, respectively) of Equation 3.24. As maximum flux is attained when $[H]_b \gg [H]_s$ and $[HA]_b \gg [HA]_s$, the third term becomes significant when $\frac{D_A \delta_H}{D_H \delta_A} \frac{[A]_b}{[H]_b} \gg 1$.
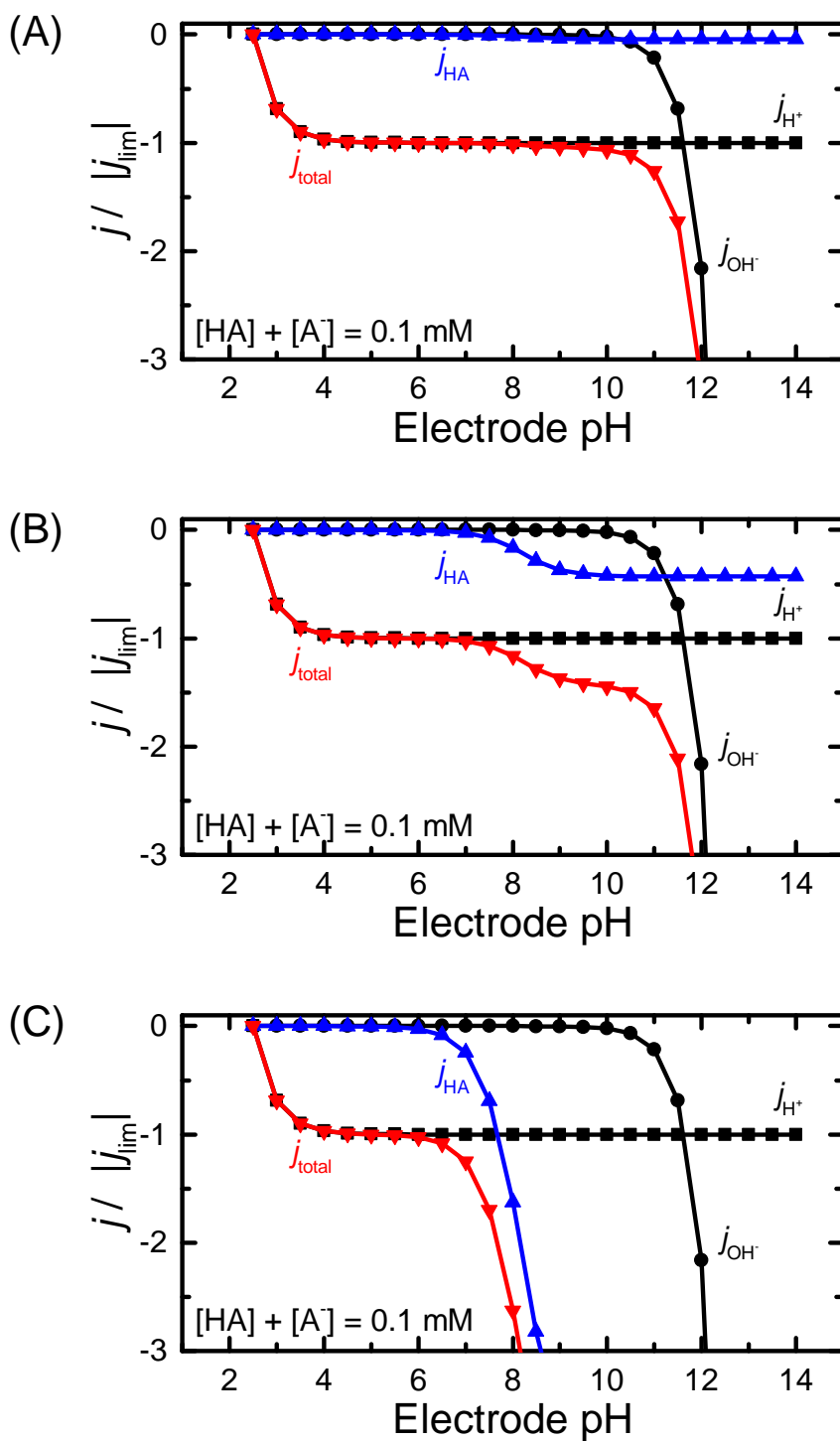
Fig. 3.14 Graphical representation of Equation 3.24 under three different total buffer concentrations (A: 0.1 mM, B: 1 mM, C: 10 mM). The flux of the H^+ and OH^- ions (black squares and circles, respectively) are equivalent to the unbuffered case. The total current density and the current density due to the flux of protons transported by HA are shown in red and blue triangles, respectively. All parameters except for those concerning buffer components are the same as in Figure 3.13.

Assuming an electrolyte in equilibrium with 1 atm of CO_2, the concentration of carbonic acid (H_2CO_3) can be estimated to be 6×10^{-5} M, based on the hydration equilibrium constant[97] $[H_2CO_3]/[CO_2] = 1.7 \times 10^{-3}$ and the solubility of CO_2 (1.5 g/L).[98] Taking into account the pK_a of carbonic acid ($pK_a \cong 3.6$) and the diffusion coefficients of bicarbonate 7.02×10^{-9} [cm^2/s],[99] leads to $\frac{D_A \delta_H}{D_H \delta_A} \frac{[A]_b}{[H]_b} = 0.00125 \ll 1$, indicating that CO_2 plays a negligible role as a buffer in pH 2.5. This is in accord with the identical height of the limiting current in Ar and CO_2 atmospheres (Figure 3.7). However, increasing the pH of the bulk electrolyte would alter this conclusion, as $[A]_b$ will increase simultaneously with the decrease of $[H]_b$. For example, a CO_2-saturated solution at pH 4 would yield a value of 1.25 for $\frac{D_A \delta_H}{D_H \delta_A} \frac{[A]_b}{[H]_b}$, indicating the buffer capacity of CO_2 cannot be ignored at pH > 4.

Having ascertained the absence of pH buffering effects from CO_2, the equations based on unbuffered electrolytes can be applied to the results obtained in pH 2.5 CO_2-saturated solutions (Figure 3.7). Specifically, the local pH at the surface of the electrode can be calculated based on Equations 3.17 and 3.18, in order to evaluate the true overpotential of the two HER pathways.

In contrast to Figure 3.7, which shows the current density with respect to the RHE at the bulk pH (pH 2.5), the voltammograms in Figure 3.15 show the normalized current density with respect to the RHE at the surface of the electrode ($U_{corrected}$). The large horizontal noise near $\frac{j_{total}}{|j_{lim}|} = -1$ is due to the drastic pH change near j_{lim} (4 < pH < 10) which amplifies the noise within the experimental current density data. There is a marked shift of the water reduction onset potential compared to the original cyclic voltammogram (Figure 3.7). In the raw experimental data, proton reduction exhibited a 600 mV smaller overpotential compared to water reduction. However, the majority of the apparent overpotential difference is due to local pH change, because the overpotential of the two HER pathways differs by only 200 mV after correcting for local pH dif-

ferences. Although the difference in the true activation barrier is much smaller than what is suggested from the raw experimental data (Figure 3.7), the smaller activation barrier of the proton reduction pathway showcases the importance of utilizing local pH to suppress the proton reduction pathway of HER to enhance the selectivity of CO_2 reduction products.
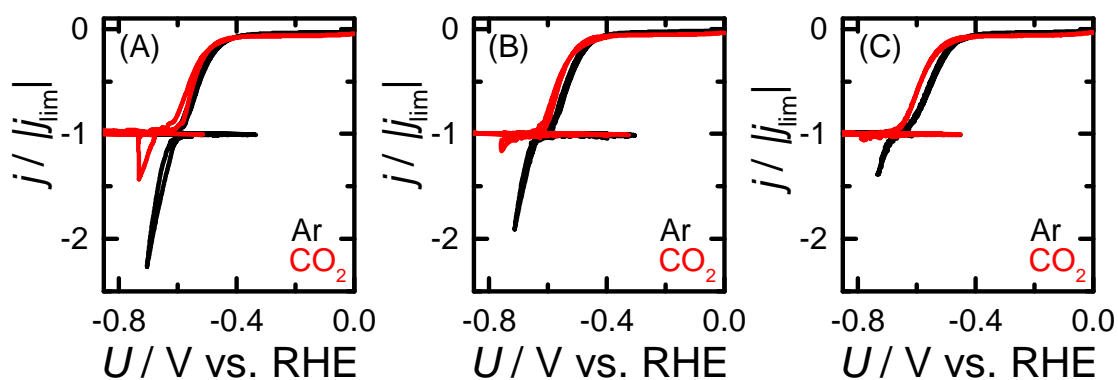
Fig. 3.15   Cyclic voltamogramms which have been corrected for changes in the local pH based on Equations 3.17 and 3.18. The original experimental data are from Figure 3.7. Black lines: Ar atmosphere, red lines: CO_2 atmosphere.

3.5 Summary and Conclusions

In summary, the author has proposed the importance of local pH effects on multi-electron transfer reactions by studying the competition between HER and CO_2 reduction. Although the two pathways of HER (proton reduction: $2\,H^+ + 2\,e^- \rightarrow H_2$ and water reduction: $2\,H_2O + 2\,e^- \rightarrow H_2 + 2\,OH^-$) were historically not differentiated, by explicitly studying the effect of pH (proton concentration) on the two pathways of HER, the contrasting behavior of the two HER pathways were highlighted. Despite the smaller activation barrier and the tolerance to inhibition by adsorbed CO, the major reaction pathway for HER was found to be the reduction of water molecules, due to the mass transport limitation of the proton reduction pathway. The observation that proton diffusion becomes rate-limiting even in a pH 2.5 electrolyte indicates the dominance of the water reduction pathway in the majority of CO_2 reduction studies which report results near pH 7. The increase of pH at the electrode surface also implies that previously neglected solution chemistry, such as the deprotonation of carbonic acid to form bicarbonate or carbonate species, may be relevant in understanding the details at the electrode-electrolyte interface. The results presented in this chapter showcase the importance of the local pH on multi-electron transfer reactions, and the understanding based on the explicit differentiation between the two HER pathways is expected to promote the development of selective catalysts for CO_2 reduction.

References

[1] Sakashita, N.; Watanabe, H. C.; Ikeda, T.; Ishikita, H. *Photosynth. Res.* **2017**, *133*, 75–85.

[2] Saito, K.; Sakashita, N.; Ishikita, H. *Aust. J. Chem.* **2016**, *69*, 991–998.

[3] Ooka, H.; Figueiredo, M. C.; Koper, M. T. *Langmuir* **2017**, *33*, 9307–9313.

[4] Ma, M.; Smith, W. A. *Anisotropic and Shape-Selective Nanomaterials*; Springer, 2017; pp 337–373.

[5] Ma, M.; Djanashvili, K.; Smith, W. A. *Angew. Chem. Int. Ed.* **2016**, *55*, 6680–6684.

[6] Zhang, Y.-J.; Sethuraman, V.; Michalsky, R.; Peterson, A. A. *ACS Catal.* **2014**, *4*, 3742–3748.

[7] Hirunsit, P.; Soodsawang, W.; Limtrakul, J. *J. Phys. Chem. C* **2015**, *119*, 8238–8249.

[8] Kortlever, R.; Tan, K.; Kwon, Y.; Koper, M. *J. Solid State Electrochem.* **2013**, *17*, 1843–1849.

[9] Kortlever, R.; Shen, J.; Schouten, K. J. P.; Calle-Vallejo, F.; Koper, M. T. *J. Phys. Chem. Lett.* **2015**, *6*, 4073–4082.

[10] Schouten, K. J. P.; Pérez Gallent, E.; Koper, M. T. *ACS Catal.* **2013**, *3*, 1292–1295.

[11] Schouten, K.; Kwon, Y.; Van der Ham, C.; Qin, Z.; Koper, M. *Chem. Sci.* **2011**, *2*, 1902–1909.

[12] Schouten, K. J. P.; Qin, Z.; Gallent, E. P.; Koper, M. T. *J. Am. Chem. Soc.* **2012**, *134*, 9864–9867.

[13] Tributsch, H. *Phys. Status Solidi. A* **2014**, *211*, 2052–2062.

[14] Lewis, N. S.; Nocera, D. G. *Proc. Natl. Acad. Sci. U. S. A.* **2006**, *103*, 15729–15735.

[15] Ma, M.; Trześniewski, B. J.; Xie, J.; Smith, W. A. *Angew. Chem. Int. Ed.* **2016**, *55*, 9748–9752.

[16] Tang, W.; Peterson, A. A.; Varela, A. S.; Jovanov, Z. P.; Bech, L.; Durand, W. J.; Dahl, S.; Nørskov, J. K.; Chorkendorff, I. *Phys. Chem. Chem. Phys.* **2012**, *14*, 76–81.

[17] Cave, E. R.; Montoya, J. H.; Kuhl, K. P.; Abram, D. N.; Hatsukade, T.; Shi, C.; Hahn, C.; Nørskov, J. K.; Jaramillo, T. F. *Phys. Chem. Chem. Phys.* **2017**, *19*, 15856–15863.

[18] Sheng, W.; Gasteiger, H. A.; Shao-Horn, Y. *J. Electrochem. Soc.* **2010**, *157*, B1529–B1536.

[19] Pastor, J.; Post, W. *Nature* **1988**, *334*, 55–58.

[20] Brysse, K.; Oreskes, N.; O' Reilly, J.; Oppenheimer, M. *Global Environ. Change* **2013**, *23*, 327–337.

[21] Dunlap, R. E.; McCright, A. M. *Organized Climate Change Denial*; Oxford University Press Oxford, 2011; pp 144–160.

[22] Hansen, J.; Sato, M.; Ruedy, R.; Lo, K.; Lea, D. W.; Medina-Elizade, M. *Proc. Natl. Acad. Sci. U. S. A.* **2006**, *103*, 14288–14293.

[23] Petit, J. R. et al. *Nature* **1999**, *399*, 429–436.

[24] Zhu, X.-G.; Long, S. P.; Ort, D. R. *Curr. Op. Biotechnol.* **2008**, *19*, 153–159.

[25] Harris, D. C. *Anal. Chem.* **2010**, 7865–7870.

[26] Bansal, A.; Zhu, L. J.; Yen, K.; Tissenbaum, H. A. *Proc. Natl. Acad. Sci. U. S. A.* **2015**, *112*, E277–E286.

[27] Miquel, J.; Lundgren, P. R.; Bensch, K. G.; Atlan, H. *Mech. Ageing Dev.* **1976**, *5*, 347–370.

[28] Olson, J. M. *Photosynth. Res* **2006**, *88*, 109–117.

[29] Blankenship, R. E. *Plant Physiol.* **2010**, *154*, 434–438.

[30] Blankenship, R. E. *Photosynth. Res* **1992**, *33*, 91–111.

[31] Powell, M. A.; Somero, G. N. *Science* **1986**, *233*, 563–567.

[32] Koch, M. S.; Mendelssohn, I. A.; McKee, K. L. *Limnol. Oceanogr.* **1990**, *35*, 399–408.

[33] Bradshaw, D.; Marsh, P.; Watson, G.; Allison, C. *Lett. Appl. Microbiol.* **1997**, *25*, 385–387.

[34] Kawasaki, S.; Watamura, Y.; Ono, M.; Watanabe, T.; Takeda, K.; Niimura, Y. *Appl. Environ. Microbiol.* **2005**, *71*, 8442–8450.

[35] Jenney, F. E.; Verhagen, M. F.; Cui, X.; Adams, M. W. *Science* **1999**, *286*, 306–309.

[36] Lane, N.; Martin, W. *Nature* **2010**, *467*, 929–934.

[37] Koonin, E. V. *Genome Biol.* **2010**, *11*, 209.

[38] Ovádi, J.; Saks, V. *Mol. Cell. Biochem.* **2004**, *256*, 5–12.

[39] Martin, W. *Philos. Trans. R. Soc. Lond. B Biol. Sci.* **2010**, *365*, 847–855.

[40] Jékely, G. *Eukaryotic Membranes and Cytoskeleton: Origins and Evolution*; Springer New York: New York, NY, 2007; pp 38–51.

[41] Hudder, A.; Nathanson, L.; Deutscher, M. P. *Mol. Cell. Biol.* **2003**, *23*, 9318–9326.

[42] Guigas, G.; Kalla, C.; Weiss, M. *FEBS Lett.* **2007**, *581*, 5094–5098.

[43] Schlebusch, C. M.; Malmström, H.; Günther, T.; Sjödin, P.; Coutinho, A.; Edlund, H.; Munters, A. R.; Vicente, M.; Steyn, M.; Soodyall, H. *Science* **2017**, *6363*, 652–655.

[44] Renne, P. R.; Deino, A. L.; Hilgen, F. J.; Kuiper, K. F.; Mark, D. F.; Mitchell, W. S.; Morgan, L. E.; Mundil, R.; Smit, J. *Science* **2013**, *339*, 684–687.

[45] D'Alessandro, D. M.; FEBS Lett., B.; Long, J. R. *Angew. Chem. Int. Ed.* **2010**, *49*, 6058–6082.

[46] Pires, J. C. M.; Martins, F. G.; Alvim-Ferraz, M. C. M.; Simões, M. *Chem. Engin. Res. Des.* **2011**, *89*, 1446–1460.

[47] Kaiser, P.; Unde, R. B.; Kern, C.; Jess, A. *Chem. Ing. Tech.* **2013**, *85*, 489–499.

[48] Xiaoding, X.; Moulijn, J. *Energy Fuels* **1996**, *10*, 305–325.

[49] Mallapragada, D. S.; Singh, N. R.; Curteanu, V.; Agrawal, R. *Ind. Engin. Chem. Res.* **2013**, *52*, 5136–5144.

[50] Joo, O.-S.; Jung, K.-D.; Moon, I.; Rozovskii, A. Y.; Lin, G. I.; Han, S.-H.; Uhm, S.-J. *Ind. Engin. Chem. Res.* **1999**, *38*, 1808–1812.

[51] Costentin, C.; Robert, M.; Savéant, J.-M. *Chem. Soc. Rev.* **2013**, *42*, 2423–2436.

[52] Lu, Q.; Rosen, J.; Zhou, Y.; Hutchings, G. S.; Kimmel, Y. C.; Chen, J. G.; Jiao, F. *Nat. Commun.* **2014**, *5*, 3242.

[53] Agarwal, A. S.; Zhai, Y.; Hill, D.; Sridhar, N. *ChemSusChem* **2011**, *4*, 1301–1310.

[54] Qiao, J.; Liu, Y.; Hong, F.; Zhang, J. *Chem. Soc. Rev.* **2014**, *43*, 631–675.

[55] Hori, Y. *Modern Aspects of Electrochemistry*; Springer, 2008; pp 89–189.

[56] Chen, Y.; Li, C. W.; Kanan, M. W. *J. Am. Chem. Soc.* **2012**, *134*, 19969–19972.

[57] Hori, Y.; Wakebe, H.; Tsukamoto, T.; Koga, O. *Electrochim. Acta* **1994**, *39*, 1833–1839.

[58] Machunda, R. L.; Ju, H.; Lee, J. *Curr. Appl. Phys.* **2011**, *11*, 986–988.

[59] Frankel, G.; Agarwal, A.; Sridhar, N. *Electrochim. Acta* **2014**, *133*, 188–196.

[60] Bumroongsakulsawat, P.; Kelsall, G. *Electrochim. Acta* **2014**, *141*, 216–225.

[61] Wu, J.; Harris, B.; Sharma, P. P.; Zhou, X.-D. *ECS Trans.* **2013**, *58*, 71–80.

[62] Peterson, A. A.; Abild-Pedersen, F.; Studt, F.; Rossmeisl, J.; Nørskov, J. K. *Energy Environ. Sci.* **2010**, *3*, 1311.

[63] Peterson, A. A.; Nørskov, J. K. *J. Phys. Chem. Lett.* **2012**, *3*, 251–258.

[64] Hansen, H. A.; Shi, C.; Lausche, A. C.; Peterson, A. A.; Nørskov, J. K. *Phys. Chem. Chem. Phys.* **2016**, *18*, 9194–9201.

[65] Nie, X.; Luo, W.; Janik, M. J.; Asthagiri, A. *J. Catal.* **2014**, *312*, 108–122.

[66] Montoya, J. H.; Peterson, A. A.; Nørskov, J. K. *ChemCatChem* **2013**, *5*, 737–742.

[67] Shi, C.; Hansen, H. A.; Lausche, A. C.; Nørskov, J. K. *Phys. Chem. Chem. Phys.* **2014**, *16*, 4720–4727.

[68] Montoya, J. H.; Shi, C.; Chan, K.; Nørskov, J. K. *J. Phys. Chem. Lett.* **2015**, *6*, 2032–2037.

[69] Ng, M.; Abild-Pedersen, F.; Kaya, S.; Mbuga, F.; Ogasawara, H.; Nilsson, A. *Phys. Rev. Lett.* **2015**, *114*.

[70] Shi, C.; Chan, K.; Yoo, J. S.; Nørskov, J. K. *Org. Process Res. Dev.* **2016**, *20*, 1424–1430.

[71] Sandberg, R. B.; Montoya, J. H.; Chan, K.; Nørskov, J. K. *Surf. Sci.* **2016**, *654*, 56–62.

[72] Liu, X.; Xiao, J.; Peng, H.; Hong, X.; Chan, K.; Nørskov, J. K. *Nat. Commun.* **2017**, *8*, 15438.

[73] Durand, W. J.; Peterson, A. A.; Studt, F.; Abild-Pedersen, F.; Nørskov, J. K. *Surf. Sci.* **2011**, *605*, 1354–1359.

[74] Yoo, J. S.; Christensen, R.; Vegge, T.; Nørskov, J. K.; Studt, F. *ChemSusChem* **2016**, *9*, 358–363.

[75] Schouten, K. J. P.; Gallent, E. P.; Koper, M. T. *J. Electroanal. Chem.* **2014**, *716*, 53–57.

[76] Auinger, M.; Katsounaros, I.; Meier, J. C.; Klemm, S. O.; Biedermann, P. U.; Topalov, A. A.; Rohwerder, M.; Mayrhofer, K. J. *Phys. Chem. Chem. Phys.* **2011**, *13*, 16384–16394.

[77] Gupta, N.; Gattrell, M.; MacDougall, B. *J. Appl. Electrochem.* **2006**, *36*, 161–172.

[78] Kas, R.; Kortlever, R.; Yılmaz, H.; Koper, M.; Mul, G. *ChemElectroChem* **2015**, *2*, 354–358.

[79] Shen, J.; Kortlever, R.; Kas, R.; Birdja, Y. Y.; Diaz-Morales, O.; Kwon, Y.; Ledezma-Yanez, I.; Schouten, K. J. P.; Mul, G.; Koper, M. T. *Nat. Commun.* **2015**, *6*.

[80] Ledezma-Yanez, I.; Wallace, W. D. Z.; Sebastián-Pascual, P.; Climent, V.; Feliu, J. M.; Koper, M. *Nat. Energ.* **2017**, *2*, 17031.

[81] Strmcnik, D.; Uchimura, M.; Wang, C.; Subbaraman, R.; Danilovic, N.; Van Der Vliet, D.; Paulikas, A. P.; Stamenkovic, V. R.; Markovic, N. M. *Nat. Chem.* **2013**, *5*, 300–306.

[82] Trummal, A.; Lipping, L.; Kaljurand, I.; Koppel, I. A.; Leito, I. *J. Phys. Chem. A* **2016**, *120*, 3663–3669.

[83] Tu, C.; Tripp, B. C.; Ferry, J. G.; Silverman, D. N. *J. Am. Chem. Soc.* **2001**, *123*, 5861–5866.

[84] Bard, A. J.; Faulkner, L. R.; Leddy, J.; Zoski, C. G. *Electrochemical Methods: Fundamentals and Applications*; Wiley: New York, 1980.

[85] Levich, V. G. *Physicochemical Hydrodynamics*; Prentice Hall, 1962.

[86] Hori, Y.; Murata, A.; Takahashi, R. *J. Chem. Soc. Faraday Trans.* **1989**, *85*, 2309–2326.

[87] Wuttig, A.; Liu, C.; Peng, Q.; Yaguchi, M.; Hendon, C. H.; Motobayashi, K.; Ye, S.; Osawa, M.; Surendranath, Y. *ACS Cent. Sci.* **2016**, *2*, 522–528.

[88] Hansen, H. A.; Montoya, J. H.; Zhang, Y.-J.; Shi, C.; Peterson, A. A.; Nørskov, J. K. *Catal. Lett.* **2013**, *143*, 631–635.

[89] Kent IV, D. R.; Widicus, S. L.; Blake, G. A.; Goddard III, W. A. *J. Chem. Phys.* **2003**, *119*, 5117–5120.

[90] Matubayasi, N.; Morooka, S.; Nakahara, M.; Takahashi, H. *J. Mol. Liq.* **2007**, *134*, 58–63.

[91] Hazra, M. K.; Francisco, J. S.; Sinha, A. *J. Phys. Chem. A* **2013**, *117*, 11704–11710.

[92] Mugnai, M.; Cardini, G.; Schettino, V.; Nielsen, C. J. *Mol. Phys.* **2007**, *105*, 2203–2210.

[93] Hori, Y.; Murata, A.; Takahashi, R.; Suzuki, S. *J. Am. Chem. Soc.* **1987**, *109*, 5022–5023.

[94] Martínez-Hincapié, R.; Berná, A.; Rodes, A.; Climent, V.; Feliu, J. M. *J. Phys. Chem. C* **2016**, *120*, 16191–16199.

[95] Chen, C. S.; Handoko, A. D.; Wan, J. H.; Ma, L.; Ren, D.; Yeo, B. S. *Catal. Sci. Technol.* **2015**, *5*, 161–168.

[96] Hori, Y.; Kikuchi, K.; Suzuki, S. *Chem. Lett.* **1985**, *14*, 1695–1698.

[97] Housecroft, C.; Sharpe, A. G. *Inorganic Chemistry (4th Edition)*; Pearson, 2012.

[98] Dodds, W.; Stutzman, L.; Sollami, B. *Ind. Engin. Chem.* **1956**, *1*, 92–95.

[99] Zeebe, R. E. *Geochim. Cosmochim. Acta* **2011**, *75*, 2483–2498.

Chapter 4

Genetic and Cellular Level Regulation of Multi-Electron Transfer

4.1 Introduction

4.1.1 Overview of This Chapter

In this chapter, the author has attempted to understand how multi-electron transfer reactions are regulated in biological systems. While factors such as valence change (Chapter 2) and local reaction environments (Chapter 3) are expected to be of importance even in biological systems, energy–material conversion takes place at a scale larger than individual enzymes, and therefore, the author has hypothesized that optimization and regulation of multi-electron transfer may take place at an even larger scale. Based on this hypothesis, the author has studied the biological multi-electron transfer process of photosynthesis from the viewpoint of enzyme genetics and motility responses to excess light. The optimization strategy of these two factors shows how biology has emphasized the balance of energy consumption and energy generation in order to realize a sustainable energy–material conversion system. Not only is this valuable insight for designing artificial multi-electron transfer systems, the regulation of multi-electron transfer at the genetic and cellular levels shown in this chapter also showcases the importance of assessing enzymes from different perspectives in order to fully understand the principles of biological optimization.

4.1.2 Importance of Understanding Biological Optimization Principles

The efficiency of energy–material conversion has always been a critical factor for biological systems. For example, the amount of energy available per gene has previously been proposed to allow the evolution of complex life on Earth.[1–4] The dominance or extinction of a species in a given ecosystem is dictated by how well they proliferate, which is limited by the amount of resources they can gather from a given environment.[5,6] The flow of energy and materials is what separates host-symbiont interactions[7–11] with that of a parasite.[12–16] Therefore, the efficiency of energy–material conversion is one of the most important aspects in biology and Nature.

Yet, biology is known to be extremely inefficient at energy–material conversion. For example, photosynthesis is one of the most widespread, and therefore evolutionary successful, means of energy–material conversion.[17,18] However, the solar-to-chemical energy conversion efficiency of photosynthesis is only in the order of 0.1–5%,[19,20] which is markedly lower than what technology is capable of achieving today.[21–23] One reason to the low energy conversion efficiency is because light intensity can no longer be harvested above a certain threshold.[24,25]

Various evolutionary strategies could have been taken to counteract this phenomenon. For example, reactive oxygen species (ROS) are proposed to both directly damage photosystem II (PS II) and inhibit its repair.[26] However, enzymes such as catalases[27,28] or superoxide dismutases[28–30] are known to specifically scavenge ROS, and an arrangement of enzymes in a super complex may alleviate photoinhibition by immediately quenching the ROS. At the physiological scale, the xanthophyll cycle has been proposed to protect the photosynthetic apparatus against excess light,[31] while heat shock has been reported to lower the threshold for photodamage.[32] These studies indicate the possibility to protect the photosynthetic apparatus from outside the photosynthetic electron transport chain. However, the fact that Nature still achieves only an overall energy con-

version efficiency of < 10 %, despite the importance of bioenergetics, seems to suggest that Nature operates under a different principle. In other words, the optimization strategy of Nature does not seem to be focused solely on higher efficiency. Therefore, uncovering how Nature optimized energy–material conversion may give insight to understanding life and the ecosystem in the context of energy–material flow.

4.2 Objective

The objective of the work presented in this chapter is to enhance the current understanding of multi-electron transfer by uncovering regulatory mechanisms which were previously unconsidered. To this end, the optimization principles of photosynthesis were studied using a combination of interspecies genetic analysis and light-induced motility experiments. This approach is in contrast to numerous studies which have proposed multi-electron transfer mechanisms of enzymes based on the X-ray crystal structures of the enzyme active site. While the majority of previous studies have focused on the scale of the protein (physical structures and 3-dimensional atomic coordinates),[33–35] the genetic and cellular level optimization presented in this chapter yields insight into the biological strategy of energy–material conversion from a different perspective. In combination with the research presented in Chapters 2 and 3 which have focused on physicochemical regulatory mechanisms such as valence change,[36–38] and local pH,[39] the author has attempted to develop an understanding of multi-electron transfer regulation which traverses a multitude of scales, from the microscopic to the macroscopic.

4.3   Materials and Methods

4.3.1   Criteria of Species Used for Genetic Analysis

All cyanobacteria species whose operon data were available within ProOpDB[40,41] as of November 2015 were investigated. A list of the species investigated, and the copy number of *psbA* and *cox1* genes within their genome, are shown in Table 4.1.

4.3.2   Criteria of Genes Used for Genetic Analysis

The function of each gene was determined based on a string search of its gene name and encoded protein description. The criteria used to classify genes are shown in Table 4.2. Although some genes were not always annotated as *psbA* or *cox1* in the original database (instead being annotated as *ctaD* for example), they have been referred to as *psbA* and *cox1* if the encoded subunit is the same. Therefore, the term "*psbA*" refers to all genes which encode the D1 subunit of PS II, and likewise in the case of "*cox1*" for subunit I of cytochrome c oxidase (COX). The KEGG (Kyoto Encyclopedia of Genes and Genomes) database[42–44] was used to supplement the scope of target genes by adding all genes listed under the categories of PS II (M00161) and COX, prokaryotes (M00155) to the genes investigated in this study.

Table 4.1 Species investigated in this study and the number of *psbA/ cox1* copies inside their genome.

Species	*psbA*	*cox1*
Acaryochloris marina MBIC11017	3	1
Anabaena Azollae 0708	2	4
Anabaena PCC 7120	5	3
Anabaena variabilis ATCC 29413	6	4
Synechococcus sp. JA-3-3Ab	4	1
Synechococcus sp. JA-2-3B′a(2-13)	3	1
Cyanothece ATCC 51142	5	3
Cyanothece PCC 7424	5	1
Cyanothece PCC 7425	3	2
Cyanothece PCC 7822	4	3
Cyanothece PCC 8801	4	1
Cyanothece PCC 8802	4	1
Gloeobacter violaceus PCC7421	5	2
Microcystis aeruginosa NIES843	6	1
Nostoc punctiforme PCC73102	5	4
Prochlorococcus marinus AS9601	2	1
Prochlorococcus marinus MED4	1	1
Prochlorococcus marinus MIT9211	1	1
Prochlorococcus marinus MIT9215	1	2
Prochlorococcus marinus MIT9301	1	1
Prochlorococcus marinus MIT9303	2	1
Prochlorococcus marinus MIT9312	2	1
Prochlorococcus marinus MIT9313	2	1
Prochlorococcus marinus MIT9515	2	2
Prochlorococcus marinus NATL1A	3	1
Prochlorococcus marinus NATL2A	3	1
Prochlorococcus marinus SS120	1	1
Synechococcus elongatus PCC6301	3	2
Synechococcus elongatus PCC7942	3	1
Synechococcus CC9311	4	2
Synechococcus CC9605	3	2
Synechococcus CC9902	4	1
Synechococcus CC7002	3	2
Synechococcus RCC307	4	2
Synechococcus WH7803	4	2
Synechococcus WH8102	4	2
Synechocystis PCC6803 GT-S	3	2
ThermosynechococcuselongatusBP1	3	1
Total	123	65

Table 4.2   Criteria for classification of gene families.

Gene family	Gene name includes:	Protein description includes:
psbA	"*psbA*"	"D1" or "q(b)"
cox1	"*cox1*" or "*ctaD*" or "*coxA*"	"subunit 1" or "subunit I"
PS II-related	"*psb*"	"photosynthe" or "photosystem II"
COX-related	"*cox*" or "*cta*"	"cytochrome c oxidase" or cytochrome-c oxidase

4.3.3 Calculation Method of Distance Between Genes

The distance between a *psbA* gene and another PS II related gene as defined by Table 4.1 was determined according to the gene position listed in ProOpDB and KEGG. The same analysis was performed for *cox1* by measuring the distance with another COX related gene. Only genes on the same DNA strand were considered for this analysis.

4.3.4 Basis of Generated ATP per Cycle for PS II

3 values of ATP/cycle (ATP/O_2, ATP: adenosine triphosphate) were used in this study, based on the report by Miyata *et al.*[45]

(1) ATP/O_2 = 4.8 based on experimental measurements. (2) ATP/O_2 = 3.0 based on H^+/e^- = 3, H^+/ATP = 4, and O_2/e^- = 1/4. (3) ATP/O_2 = 2.6 based on H^+/e^- = 3, H^+/ATP = 14/3, and O_2/e^- = 1/4. Further details concerning the origin of ATP/O_2, such as the number of protons transferred during light harvesting or the number of protons necessary for the synthesis of 1 ATP molecule, can be found in the original literature.

4.3.5 Basis of Generated ATP per Cycle for COX

The amount of ATP generated during 1 cycle of respiration was determined based on the fact that the complete oxidation of 1 glucose molecule yields 38 molecules of ATP (2 from glycolysis, 2 from the tricarboxylic acid (TCA) cycle, 4 from 2 molecules of flavin adenine dinucleotide (FADH$_2$), and 30 from 10 molecules of nicotinamide adenine dinucleotide (NADH)). As this process uses 6 oxygen molecules, the ATP produced per O_2 molecule is 6.3.[46]

4.3.6 Estimation of Repair Costs from Gene Expression Costs

It is well established that the least stable subunit of PS II is the catalytic D1 subunit, because the reactive oxygen species are produced during photoinhibition at the catalytic site. It has also been clarified that the D1 subunit is rapidly re-

synthesized via expression of the *psbA* gene under *in-vivo* conditions.[45,47,48] On the other hand, although the least stable COX subunit is less obvious, *cox1* genes form an operon with *cox2* and *cox3* genes as shown in Figure 4.3A. Therefore, the repair cost of COX is insensitive to which COX gene was used to estimate the repair cost (Figure 4.5).

4.3.7 Cultivation of *E. gracilis*

Euglena gracilis strain Z cells were provided by Euglena Co., Ltd. and were cultivated photoautotrophically in Cramer-Myers medium according to previous literature.[49,50] The *E.* gracilis cells were allowed to reach the stationary phase using 60-mL test tubes at 29 °C under constant illumination by a 20-watt fluorescent lamp. The medium was bubbled constantly with 5% CO_2-in-air during cultivation.

4.3.8 Photoresponse Measurements

Cells were used for the photoresponse measurements immediately after removing from the incubator. Therefore, no process to align their day-light cycles were performed. Monochromatic light was irradiated horizontally into a transparent petri dish containing *ca.* 15 mL of cell suspension at an optical density (OD) of 0.4 at 680 nm. The dry cell weight per liter was roughly 0.2 g, and the cell density was estimated to be $\sim 10^6$ cells per mL. A 300 W Xe lamp (Asahi Spectra, MAX-302) equipped with a UV cut-off filter (L39, transparent at wavelengths larger than 390 nm, Irie Seisakusho) and an interference filter was used as the monochromatic light source. The irradiated light had a half-width of *ca.* 10–15 nm and projected in a cone-like shape, rather than a straight gradient. No heat filter was used due to the light strength in the IR region being negligible. After 24 hours of light irradiation, a photograph of the resulting cell suspension was taken.

4.3.9   Calculation of the Optimum light intensity

The light intensity at the region with the highest cell concentration after 24-hour-irradiation was defined as the "optimum light intensity", due to the apparent preference of *E. gracilis* cells to orient themselves at this light intensity. The light intensity at this specific region of the petri dish was measured using a Spectro-radiometer (Ushio USR 45). ND filters from Asahi Spectra were used in case the light intensity was too high to be measured directly. No light diffraction or dispersion at the edge of the petri dish which held the cell suspension was accounted for.

4.3.10   Cell Aggregation Measurements

20-mL cell suspensions at an OD_{680} of 0.4 (dry cell weight = 0.2 g/L) were added to 20-mL serum bottles, which were then irradiated from below at an intensity of 2.5 mW cm^{-2}, or wrapped in aluminum foil as a control experiment for cells kept in the dark. After 24 hours, 0.4-mL samples of the resulting suspension was repeatedly taken from the topmost layer to a 96-well plate until the entire cell suspension had been collected (see Figure 4.1 for a visual representation). The absorption at 680 nm of each well was measured using a plate reader (Tecan Infinite M200 PRO) to estimate the cell concentration in each sample.
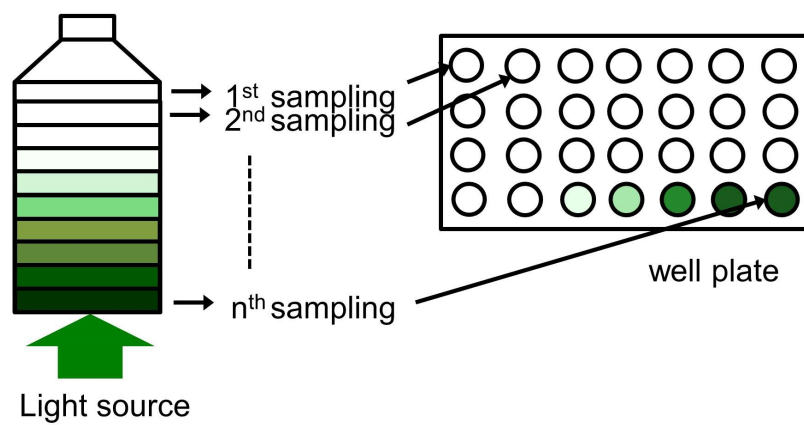
Fig. 4.1 Methodology of cell aggregation measurements. 0.4-mL aliquots of the cell suspension were repeatedly sampled from the topmost layer into a 96-well plate.

4.4 Results and Discussion

4.4.1 Gene Level Regulation

As shown in Figure 1.1, PS II and COX catalyze the oxygen evolution reaction (OER) and the oxygen reduction reaction (ORR), which are reverse reactions of each other.[51,52] The two reactions combined compose a sustainable energy conversion cycle, similar to how mankind may one day use solar-driven water electrolysis in combination with fuel cells.[51] The energy produced during the multi-electron transfer reactions at PS II and COX are initially converted to a chemical potential gradient of protons (proton motive force) which is later converted to ATP (Figure 4.2A).[46,53–56] Eventually however, the deactivation of the multi-electron transfer enzymes will occur, triggering a repair process (Figure 4.2B). The cost of this repair process, defined by the amount of ATP necessary to repair the enzyme, is related to the length of the genetic sequence encoding the damaged region.[46] In terms of life-cycle assessment, the amount of ATP produced during OER/ORR (Figure 4.2A) must be larger than the amount of ATP necessary to repair the enzyme (Figure 4.2B) to ensure a net positive energy gain. In light of the fact that stability is a critical requirement even in artificial systems,[57,58] understanding how Nature addressed life-cycle costs of multi-electron transfer enzymes is expected to provide a guideline for the development of artificial systems.[52,59]

(A) Energy Generation

Proton pumping
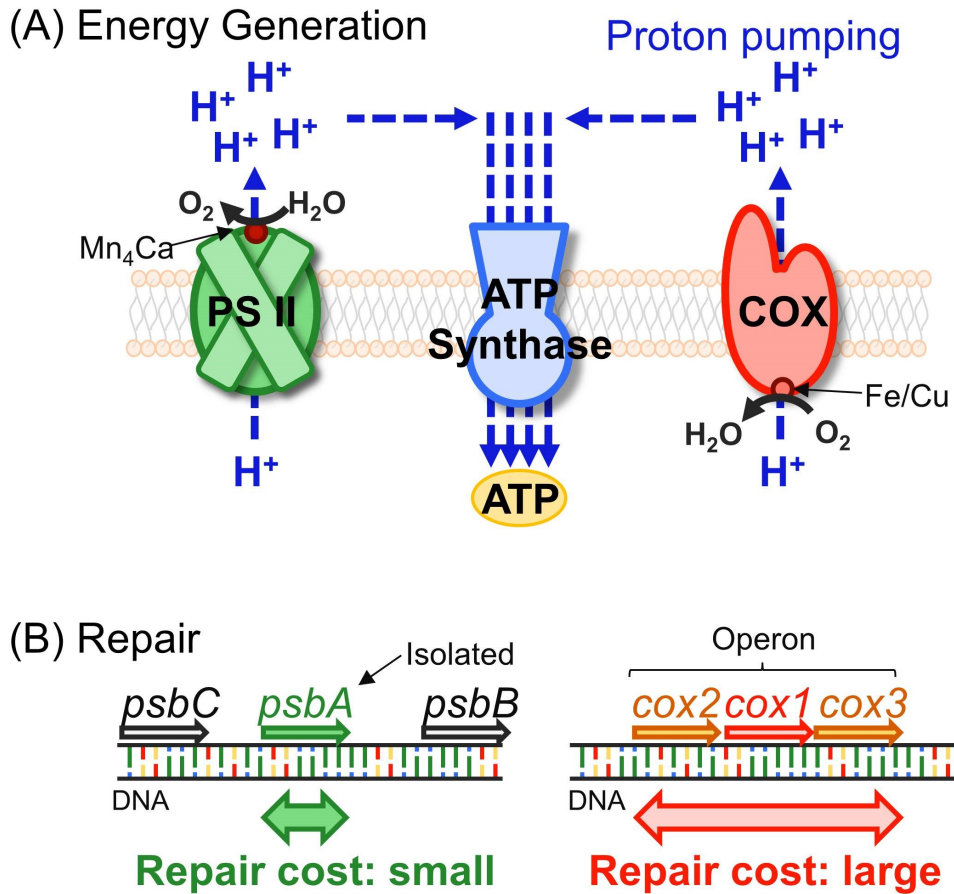
(B) Repair

Fig. 4.2 Schematic diagram of photosynthesis (enzyme: PS II) and respiration (enzyme: COX). PS II and COX generate energy (ATP) *via* OER and ORR (A) Upon enzyme deactivation, ATP is consumed to repair the catalyst (B). A longer genetic sequence increases the repair cost. The balance between ATP generation (stability) and consumption (repair) dictates the minimum turnover cycles necessary for a net positive ATP yield.

In order to assess the optimization strategy concerning the repair cost of PS II and COX, their genetic structure was investigated. It is well known that genetic information is often organized into structures called operons[60–64] in the case of prokaryotes such as cyanobacteria. This allows the expression of nearby genes ($\leq$ 20 kilobasepairs, kbp) to be regulated simultaneously. This would be beneficial for organisms which possess only a small amount of energy per gene such as prokaryotes, because fewer regulatory regions would allow for smaller genome sizes.[1] On the other hand, forming an operon would increase the repair cost due to the larger size of the coding region.

Figure 4.3A shows the operon structure of *psbA* and *cox1* in a histogram format, compiled from the prokaryotic operon database ProOpDB.[40,41] The two genes encode the catalytic region of PS II and COX (*psbA*: D1 subunit of PS II, *cox1*: subunit I of COX), and therefore, biological optimization of OER and ORR catalysts is expected to be most pronounced in these two genes. Based on this database, the majority of *psbA* genes (94 %) were expressed individually (number of co-expressed genes:1), whereas *cox1* was almost always expressed together with the two other subunits of COX (number of co-expressed genes:3).
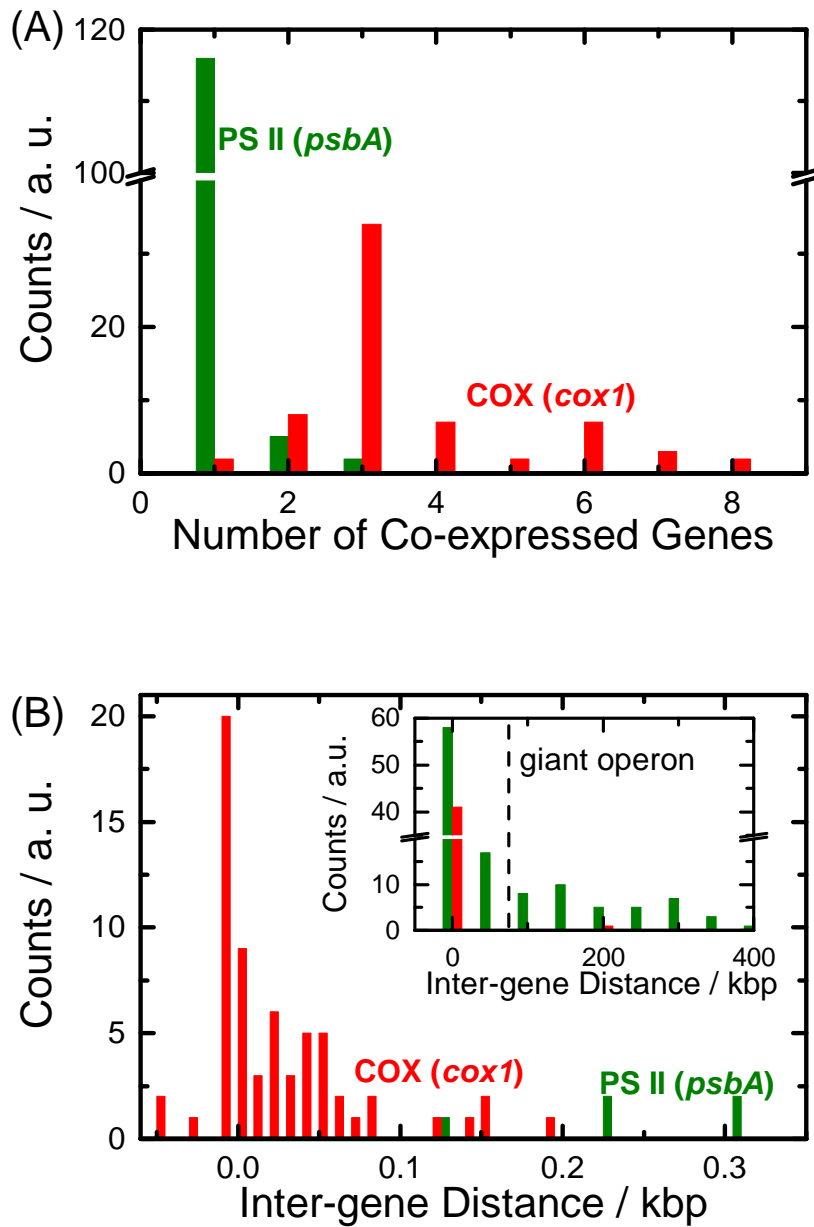
Fig. 4.3 Genetic structure of *psbA* and *cox1* genes. A: Number of coexpressed genes based on the operon prediction of ProOpDB. B: Distance between *psbA* and another PS II gene or *cox1* and another COX gene. Inset shows the inter-gene distance on a larger scale.

The tendency to express *psbA* genes individually compared to *cox1* can also be found in Figure 4.3B, which shows the inter-gene distance in histogram format. In the case of *cox1*, *cox2* and *cox3* were almost always found to be located less than 0.1 kbp away on the same DNA strand, providing further evidence that the catalytic site of COX (*cox1*) is synthesized together with the substrate-binding site (*cox2*) and the transmembrane scaffold (*cox3*). On the other hand, the *psbA* gene is located distally from other PS II genes as can be seen in the inter-gene distance which is several orders of magnitude larger than that of COX (Figure 4.3B inset). In many cases, the distance between the *psbA* gene and another PS II gene is larger than even the largest operons reported in the literature (70–80 kbp, dashed line in inset).[64] These results indicate that although PS II as a whole functions as a water-oxidizing photo-anode, the OER catalytic site (*psbA*) is synthesized independently from light-harvesting antennae complexes (*psbB*, *psbC*), other reaction center proteins (*psbD*), or secondary electron transport subunits (*psbE*, *psbF*). The result from the inter-gene distance analysis is consistent with the analysis based on the operon structure: *psbA* is regulated independently from other PS II genes, while *cox1* is regulated together with other major COX subunits. Although the independent behavior of the *psbA* gene[47,65,66] and the operonic nature of the *cox1* gene[67] has been proposed previously based on biochemical observations, this is the first study which has explicitly confirmed a stark contrast between the genetic strategy of OER and ORR enzymes.

In order to evaluate how differences in the genetic structure affect the bioenergetics of multi-electron transfer enzymes, the repair cost of each enzyme was estimated based on Equation 4.1, which represents the expression cost of a gene. The first and second terms of this equation correspond to gene transcription[68] and translation[69] costs, respectively.

$$
\begin{aligned}
\text{Repair Cost} = {} & 2 \times (\text{DNA sequence length}) \\
& + 2 \times (\text{protein sequence length}) \; [\text{unit : ATP}]
\end{aligned}
\tag{4.1}
$$

Here, sequence lengths refer to the number of base pairs and amino acid monomers. In the case of PS II, the gene expression cost of *psbA* was considered to represent the repair cost of the enzyme, because the photoinhibititory effects from ROS are most pronounced in the catalytic D1 subunit.[45,70,71] On the other hand, the gene expression costs of *cox1* were used to calculate the repair cost of COX, because the operonic nature of *cox1* with *cox2* and *cox3* genes indicates the repair cost of COX is irrelevant to which gene is used for the repair cost estimation.

The enzyme repair cost of PS II and COX, calculated from the gene expression cost of *psbA* and *cox1*, is shown in Figure 4.4A. The selective replacement of the catalytic subunit, made possible by the individual regulation of the *psbA* gene, benefits PS II significantly as can be seen in the differences in the repair cost (PS II: $\sim 2.5 \times 10^3$ [ATP], COX: $\sim 8 \times 10^3$ [ATP]).

It should be noted that the repair cost estimated by Equation 4.1 does not consider other processes which may require additional ATP such as post-translational events or amino acid monomer synthesis. Therefore, Equation 4.1 is expected to give an underestimate of the repair cost of each enzyme. Therefore, the repair cost estimated from Equation 4.1 represents the minimum amount of ATP each enzyme must generate in order for the net ATP yield to be positive. As the total amount of ATP produced during the lifetime of an enzyme

is determined by the number of catalytic cycles it performs before deactivation (turnover number, TON), the stability requirement for each enzyme to generate a net positive amount of ATP is represented in the following inequality:

$$\text{Lifetime ATP yield} = (\text{TON} \times \text{ATP/Cycle}) - (\text{Repair Cost}) > 0 \qquad (4.2)$$

While the exact value of the ATP generated per OER cycle (ATP/O_2) at PS II differs depending on the evaluation method,[45] a stark contrast in the minimum TON between the two multi-electron transfer enzymes can nonetheless be observed. As shown in Figure 4.4B, only $500 \sim 1000$ cycles are necessary to generate the ATP required for PS II repair, because the genetic structure of the *psbA* gene allows the OER catalytic site to be repaired selectively. On the other hand, COX has a much larger minimum TON ($\sim$1500), because the simultaneous regulation of all of its components leads to an increase in the repair cost.
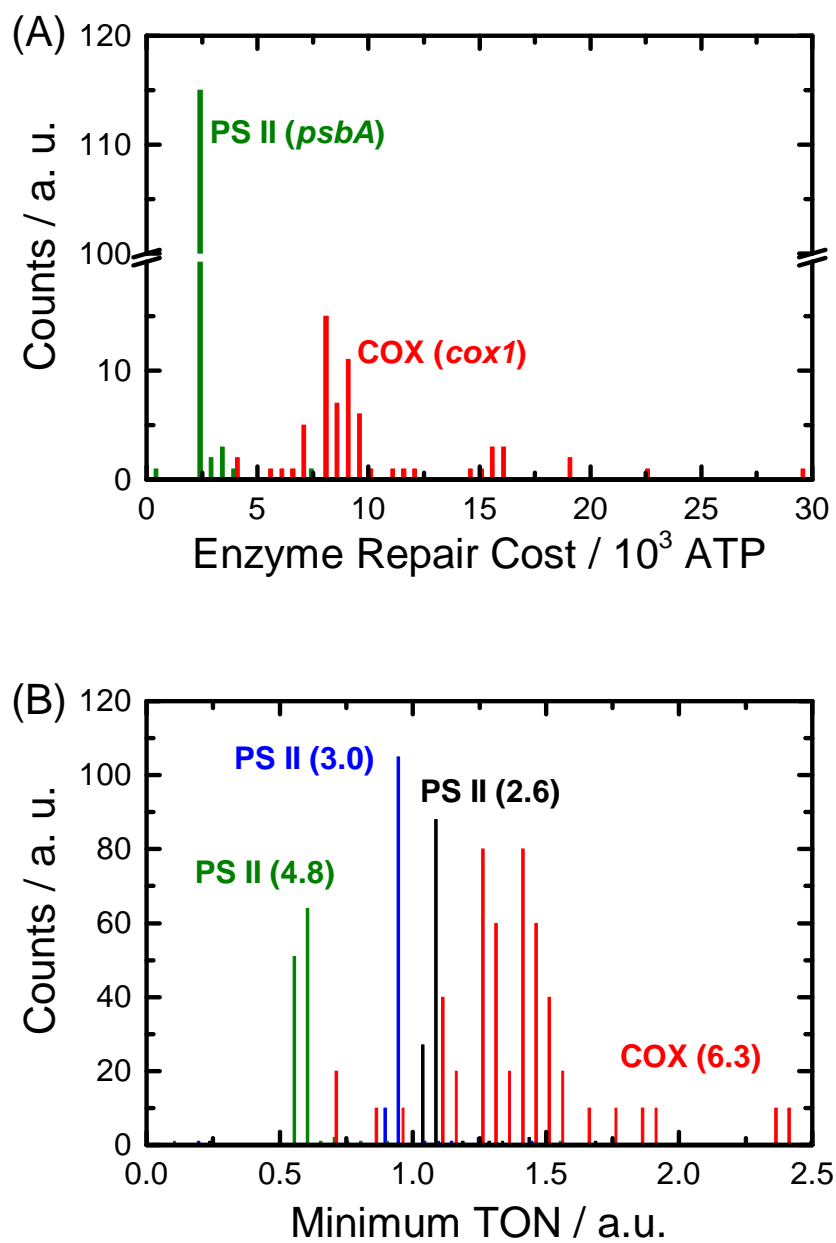
Fig. 4.4 A: Histogram of the repair cost of PS II and COX B: Histogram of the minimum TON for PS II and COX. Numbers in parentheses indicate the ATP/cycle used for the calculation.
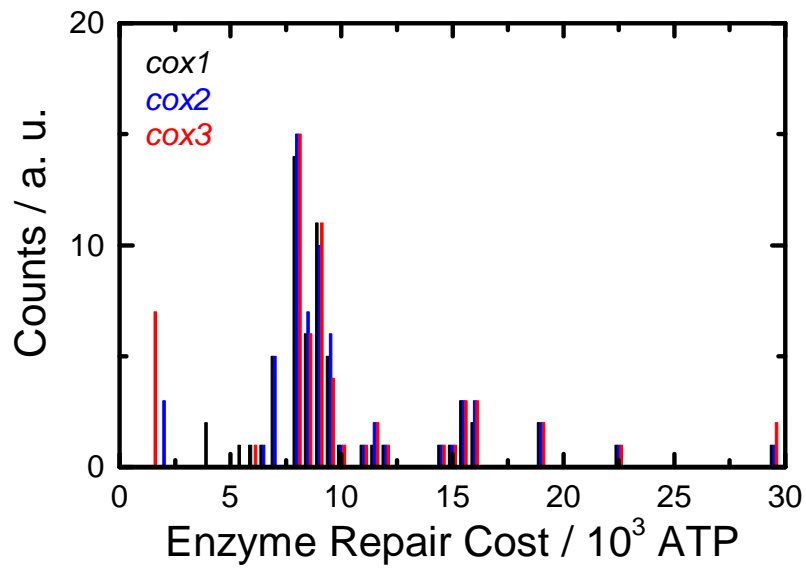
Fig. 4.5   Histogram of the repair cost of COX depending on which gene was used for the calculation.

The difference in repair cost showcases a stark contrast in terms of enzyme bioenergetics between OER and ORR enzymes. While the photoinhibition process of PS II is already well recognized,[35,45,48,70–78] the strategy to how this challenge was addressed in Nature was revealed only by directly comparing the genetic structure of PS II and COX across 38 species of phylogenetically diverse[79] cyanobacteria. The results shown here suggest that instead of directly addressing the low stability of PS II by developing a more robust OER enzyme, Nature has circumvented this problem altogether by isolating the gene encoding the least stable D1 subunit (*psbA*) from other PS II genes (Figure 4.3). The separate regulation of the unstable OER center with other PS II components such as light-harvesting pigments lowers the repair cost of PS II such that replacing the D1 subunit upon damage becomes a viable strategy. Therefore, instead of optimizing the OER enzyme at the protein crystal structure level to enhance the stability, optimization of the genetic structure has proven to be an effective strategy to counteract the low stability of PS II.

4.4.2 Cellular Level Regulation

In order to confirm how biology addressed the challenge of stability at the cellular scale, the photomotility[*1] of *E. gracilis* cells were studied. Although the photoresponse of *E. gracilis* cells has been known for more than 100 years ago,[86] the present study is the first to study this physiological response from the viewpoint of multi-electron transfer regulation. As the primary evolutionary benefit of motility is to optimize the surrounding environment, it can be expected that *E. gracilis* cells will orient themselves according to the light intensity and the wavelength.

As *E. gracilis* cells are known to show behavioral responses to gravity and oxygen levels,[87,88] the motility of *E. gracilis* cells was first studied using a petri dish with lateral light irradiation. This approach allows only the photoresponse of the cells, rather than the response to a mixture of stimuli, to be evaluated. Figure 4.6 shows the cell distribution within a petri dish before and after light irradiation for 24 hours. Prior to irradiation of the cell suspensions, the cells were uniformly distributed (Figure 4.6A). Upon irradiation with blue light (400 nm, 1.5 mW cm^{-2}) for 24 hours, an intense band of cells with a "C" shape was formed around the light origin (Figure 4.6B). On the other hand, irradiation of green light (530 nm, 1.5 mW cm^{-2}) resulted in the cells being selectively attracted to the light source (Figure 4.6C). These results clearly show that *E. gracilis* cells exhibit a wavelength dependent response to visible light, which was further confirmed by the homogeneous cell distribution formed after several hours of turning off the light source.

[*1] *E. gracilis* cells are known to exhibit several photo-induced motility responses, such as phototaxis, photophobic response, and photokinesis.[80–85] Although these phenomena are biologically distinct behavior due to differences in signal transductory pathways, these responses can be discerned only at the scale of each individual cell ($\sim \mu$m scale). For this reason, the term "photoresponse" was used in this section to refer to these responses collectively.
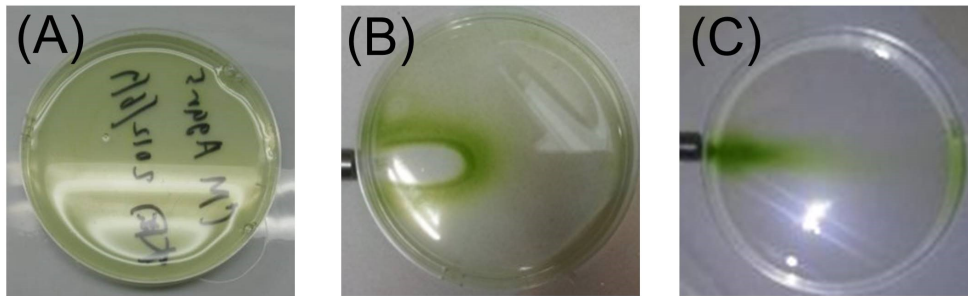
Fig. 4.6 Cell distribution before and after light irradiation. A: Homogeneous cell distribution prior to light irradiation. B: 24 hours after irradiation of monochromatic light (400 nm) from the left. C: 24 hours after irradiation of monochromatic light (530 nm) from the left. The light intensity was 1.5 mW cm^{-2} in all cases.
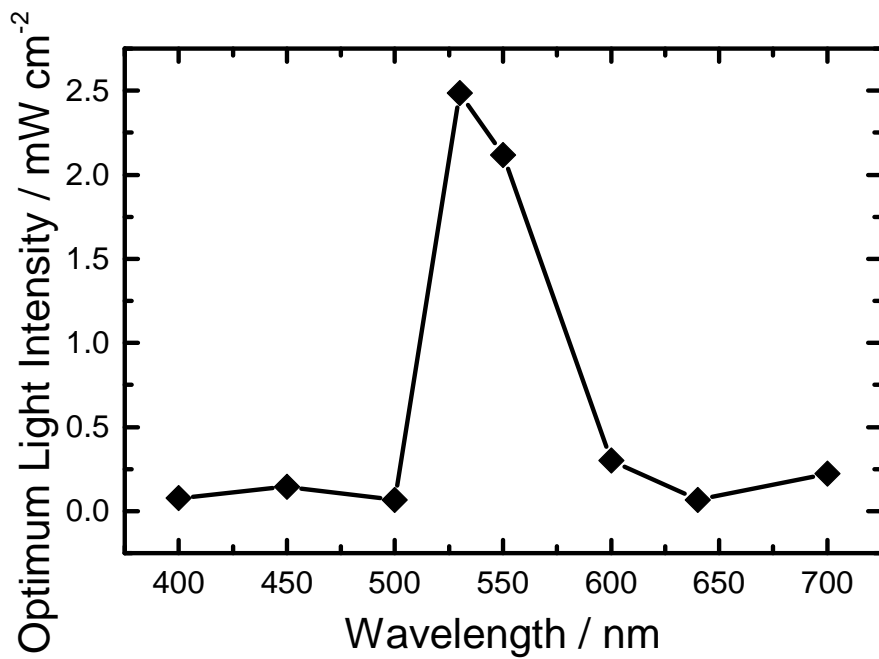
Fig. 4.7 Action spectrum of negative photoresponses.

In order to ascertain whether photosynthesis and photoinhibition are related to the observed photomotility response, the light intensity at which each wavelength of light induces a negative photoresponse was monitored. The action spectrum of the negative photoresponse is shown in Figure 4.7.

It has been previously reported that *E*. gracilis cells form a visible band perpendicular to the oxygen gradient, because the cells are attracted to a specific oxygen concentration, which allows for maximum cell activity.[88] In analogy to this oxytactic response, the author hypothesized that the photoresponse of *E*. gracilis is also influenced by an optimum light intensity (OLI). At the OLI, the photosynthetic activity would be sufficiently high to maintain required energy levels, but the cells would not experience significant photoinhibitory effects. If the OLI represents the border intensity where *E*. gracilis cells switch between positive and negative photoresponses,[*2] it can be expected that cells will accumulate at regions corresponding to the OLI, where they will ultimately form a visible band of cells. According to this hypothesis, the OLI is expected to show a wavelength dependence, as not all wavelengths of light are photosynthetically active. To investigate this hypothesis, the light intensity at the place with highest cell concentration was measured using light with various wavelengths and intensity.

Figure 4.7 shows the plots of OLI in the wavelength region between 400 and 700 nm. The obtained spectrum shows that photosynthetically active light (blue and red) have a lower OLI compared to wavelengths that are inactive for photosynthesis ($500 < \lambda < 600$ nm). In contrast to blue and red light, the cells were attracted to all but the strongest intensities of green light (Figure 4.6). These results support the hypothesis that the balance between photosynthesis and photoinhibition influences the photomotility of *E*. gracilis, as a clear preference to

---

[*2] Positive photoresponse: Approach the light source, negative photoresponse: Avoid the light source.

avoid high-intensity photosynthetic light could be observed. Instead, cells preferentially orient themselves at light intensities which avoid the detrimental effects of photoinhibition, but still allow photosynthesis to proceed.

This result correlates well with those from an experiment in which the light intensity of blue light directed at the cells was reduced from 1.5 to 0.15 mW cm^{-2} (Figure 4.8). As these images show clearly that *E.* gracilis cells approached the source of blue light as the intensity was reduced, it appears that *E.* gracilis cells indeed have an OLI which is related to photosynthesis and photoinhibition.

The results of the *E.* gracilis photomotility confirms the importance of preventing photoinhibition proposed based on the genetic analysis presented in the previous section. Although photochemical considerations suggest it would be beneficial for the photosynthetic organisms to accumulate in regions with higher intensities of photosynthetically active light, *E.* gracilis cells were found to retreat from photosynthetically active blue and red light unless the light intensity was lowered below the OLI. The observation that photosynthetic organisms retreat from photosynthetically active light show to what extent biology valued stability over energy conversion efficiency, and yields insight into the inefficiency of biological photosynthesis.
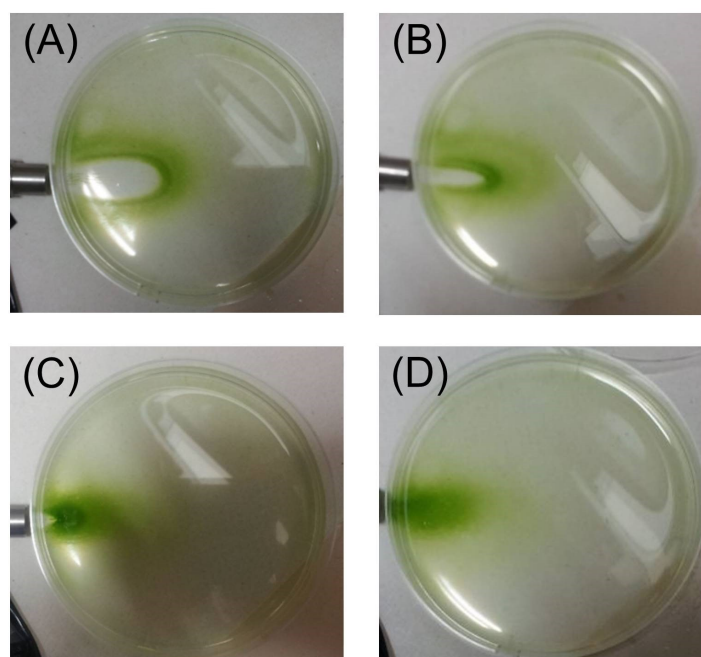
Fig. 4.8　Difference in cell distribution according to the intensity of 400-nm light. (A): 1.5, (B): 0.75, (C): 0.33, and (D): 0.15 mW cm^{-2}, respectively.

4.4.3 Biofuel Production Using *E. gracilis* Photomotility

In addition to the cellular-level multi-electron transfer regulation based on cell motility, the author has attempted to apply the macroscopic photoresponse in algal biofuel production.[89] The methodology presented here has been filed as an international patent.[90]

Biofuel production from CO_2 using microalgae has been the focus of intensive research[91–93] for producing carbon neutral sources of energy, due to their higher fuel production rate per gram of biomass in comparison to high plants such as corn and sugar canes.[94] However, one of the main issues in algal biofuel production at the industrial scale is the large amount of energy required for downstream processing steps, such as harvesting the microalgae cells from the growth media.[94–101]

As a possible cost-effective alternative to existing techniques such as centrifugation[96] or membrane separation,[97] the macroscopic photoresponse of *E. gracilis* cells was investigated. Additional benefits of using *E. gracilis* cells include the high commercial value of its photosynthetic product as a precursor of jet fuel[102] and the ease of suppressing contamination, due to the acidic pH ($\sim$3.5) of its autotrophic growth medium (Cramer-Myers medium).

Based on the OLI curve shown in Figure 4.7, 530-nm green light was expected to be most efficient for cell aggregation. This is because although increasing the light intensity enlarges the collection area, thus allowing for the operation of larger bioreactors, cells avoid areas with light intensity higher than the OLI. In the case of green light, the light intensity can be increased to 2.5 mW cm^{-2} due to the high tolerance of *E. gracilis*. This light intensity can be easily obtained from spectral diffraction of sunlight without loss of efficiency, because green light was originally "wasted" in terms of photosynthetic efficiency.

Figure 4.9 shows the results of the cell aggregation performed in a 20-mL serum bottle. The serum bottle was irradiated with 530-nm light from the bottom, and

after 24 hours, the supernatant was progressively sampled from top to bottom (See Figure 4.1 for details) and examined spectroscopically in 96-well plates.

The control sample left in the dark for 24 hours remained homogeneous as the cell concentration showed negligible difference between the topmost sample and the bottommost sample. However, in the case of green light irradiation, the color of the sampled aliquot was clear and transparent, except for the last four samples. The final four samples, taken from the bottom of the serum bottle, contained cells that had accumulated at the vicinity of the light source during light irradiation. A quantification of the cell concentration, estimated from the absorption measurements at 680 nm (chlorophyll absorption) is shown in Figure 4.10, along with the results of samples generated using white light (non-monochromatic light) of the same intensity.

Fig. 4.9   Photograph showing the results of the cell sampling.
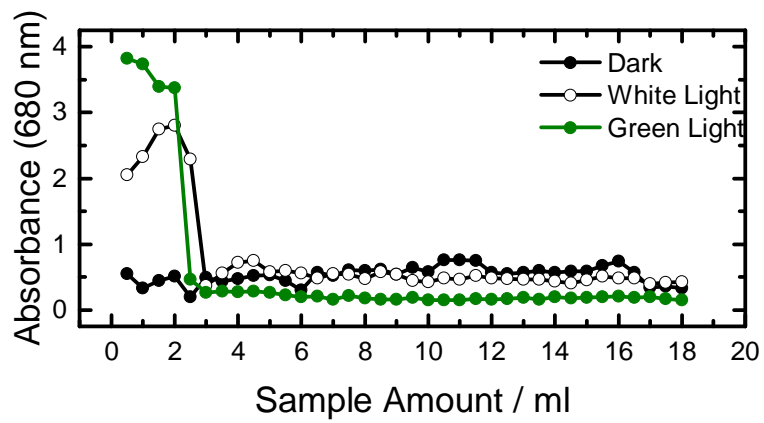
Fig. 4.10 Depth profile of the cell concentration estimated based on the absorption at 680 nm.

Although white light also promoted cell accumulation, green light proved to be more efficient at concentrating the cells. A possible explanation may be because white light consists of light with different wavelengths, each of which has a different OLI. As each wavelength of light would attract cells to different regions of the reactor, this would result only in a broad attraction of cells to the light source. This photoresponse is in stark contrast to the acute cell distribution at the bottom of the bottle observed in the case of green light. Based on the absorbance of the four samples collected from the bottom of the serum bottles after green-light irradiation (Figure 4.10), the cell accumulation rate and cell collection rate were found to be 8.7-fold and 70%, respectively. The intense cell accumulation was also seen from optical microscopic images of the sampled liquid from the bottle with light (Figure 4.11).
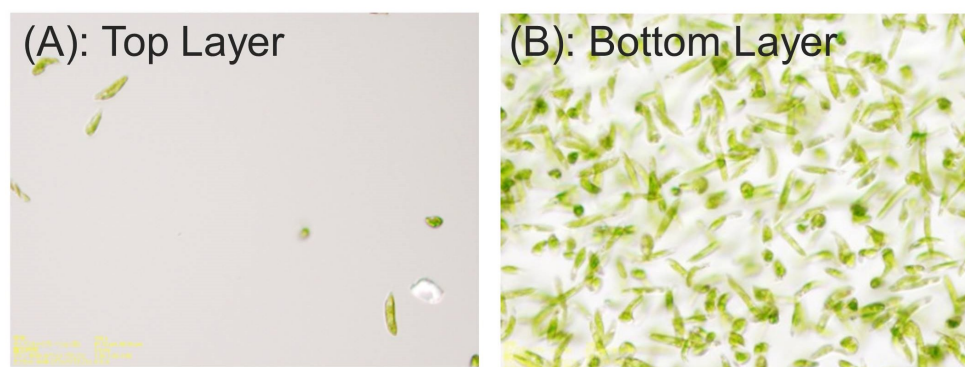
Fig. 4.11 Optical microscope images of the *E.* gracilis suspension sampled from the top (A) and bottom (B) of the serum bottle after green light irradiation.

The cell concentration efficiency realized by this method are comparable to the efficiency of centrifugal separation.,[95] and utilization of green light for cell aggregation has multiple benefits. For example, the lack of competition with the light absorption by chlorophylls in photosystems I and II allows green light to penetrate into the cell suspension twice as efficiently as blue or red light. Therefore, the findings in this present study offer the use of green light in solar radiation, which was originally wasted energy in photosynthesis, as the energy source for one of the most energy-intensive downstream processes in microalgal biofuel production.

4.5 Summary and Conclusions

The results presented in this chapter provide evidence that photosynthesis was optimized not towards a higher power conversion efficiency within the process of photosynthesis, but towards a higher net power conversion efficiency at the cellular scale, which is dictated by the balance of energy consumption and generation. In the case of genetic optimization, it became apparent that PS II was optimized such that the cost of enzyme repair was minimized. While the genetic level optimization does not serve to increase the power conversion efficiency during photosynthesis, it allows the net energy gain to be increased by minimizing the amount of energy necessary for enzyme repair. The evolutionary strategy to minimize the damage from excess light is further manifest in the photomotility of *E.* gracilis cells, as the optimum light intensity for photosynthetically active light was 10-fold weaker compared to photosynthetically inactive light. This suggests the existence of a tandem structure in Nature, where light energy not used for photosynthesis is used to guide the cells to optimum light conditions. The author has demonstrated the potential use of this photo-induced behavioral response as a potential method for cell concentration in biofuel processing.[90]

References

[1] Lane, N.; Martin, W. *Nature* **2010**, *467*, 929–934.

[2] Thannickal, V. J. *Am. J. Respir. Cell. Mol. Biol.* **2009**, *40*, 507–510.

[3] Raymond, J.; Segrè, D. *Science* **2006**, *311*, 1764–1767.

[4] Halliwell, B. *Plant Physiol.* **2006**, *141*, 312–322.

[5] Allesina, S.; Bodini, A. *J. Theor. Biol.* **2004**, *230*, 351–358.

[6] Dohm, C.; Leal, I. R.; Tabarelli, M.; Meyer, S. T.; Wirth, R. *J. Trop. Ecol.* **2011**, *27*, 645–649.

[7] Wolpert, J. S.; Albersheim, P. *Biochem. Biophys Res. Commun.* **1976**, *70*, 729–737.

[8] Carlson, R. W.; Sanders, R. E.; Napoli, C.; Albersheim, P. *Plant Physiol.* **1978**, *62*, 912–917.

[9] Ishikawa, H. *Insect Biochem.* **1982**, *12*, 613–622.

[10] Pai, R.; Kang, G. *Ind. J. Med. Res.* **2008**, *128*, 587.

[11] Dale, C.; Moran, N. A. *Cell* **2006**, *126*, 453–465.

[12] Kitchell, J. F.; Breck, J. E. *Can. J. Fish Aquat. Sci.* **1980**, *37*, 2159–2168.

[13] Barber, I.; Scharsack, J. *Parasitology* **2010**, *137*, 411–424.

[14] Giorgi, M. S.; Arlettaz, R.; Christe, P.; Vogel, P. *Proc. R. Soc. Lond., B, Biol. Sci.* **2001**, *268*, 2071–2075.

[15] Mayack, C.; Naug, D. *J. Invertebr. Pathol.* **2009**, *100*, 185–188.

[16] Sheldon, B. C.; Verhulst, S. *Trends Ecol. Evol.* **1996**, *11*, 317–321.

[17] Raines, C. A. *Plant Physiol.* **2011**, *155*, 36–42.

[18] Ting, C. S.; Rocap, G.; King, J.; Chisholm, S. W. *Trends Microbiol.* **2002**, *10*, 134–142.

[19] Esper, B.; Badura, A.; Rögner, M. *Trends Plant Sci.* **2006**, *11*, 543–549.

[20] Zhu, X.-G.; Long, S. P.; Ort, D. R. *Curr. Op. Biotechnol.* **2008**, *19*, 153–159.

[21] Fujii, K.; Nakamura, S.; Sugiyama, M.; Watanabe, K.; Bagheri, B.; Nakano, Y. *Int. J. Hyd. Energ.* **2013**, *38*, 14424–14432.

[22] Nakamura, A.; Ota, Y.; Koike, K.; Hidaka, Y.; Nishioka, K.; Sugiyama, M.; Fujii, K. *Appl. Phys. Express* **2015**, *8*, 107101.

[23] Jia, J.; Seitz, L. C.; Benck, J. D.; Huo, Y.; Chen, Y.; Ng, J. W. D.; Bilir, T.; Harris, J. S.; Jaramillo, T. F. *Nat. Commun.* **2016**, *7*, 13237.

[24] Powles, S. B. *Annu. Rev. Plant Physiol.* **1984**, *35*, 15–44.

[25] Barber, J.; Andersson, B. *Trends Biochem. Sci.* **1992**, *17*, 61–66.

[26] Nishiyama, Y.; Allakhverdiev, S. I.; Murata, N. *Biochim. Biophys. Acta* **2006**, *1757*, 742–749.

[27] Beers, R. F.; Sizer, I. W. *J. Biol. Chem.* **1952**, *195*, 133–140.

[28] Orr, W. C.; Sohal, R. S. *Science* **1994**, *263*, 1128–1128.

[29] Grankvist, K.; Marklund, S. L.; Täljedal, I. *Biochem. J.* **1981**, *199*, 393–398.

[30] Melov, S.; Ravenscroft, J.; Malik, S.; Gill, M. S.; Walker, D. W.; Clayton, P. E.; Wallace, D. C.; Malfroy, B.; Doctrow, S. R.; Lithgow, G. J. *Science* **2000**, *289*, 1567–1569.

[31] Demmig, B.; Winter, K.; Krüger, A.; Czygan, F.-C. *Plant Physiol.* **1987**, *84*, 218–224.

[32] Schuster, G.; Even, D.; Kloppstech, K.; Ohad, I. *EMBO J.* **1988**, *7*, 1.

[33] Rossmeisl, J.; Dimitrievski, K.; Siegbahn, P.; Nørskov, J. K. *J. Phys. Chem. C* **2007**, *111*, 18821–18823.

[34] Yano, J.; Yachandra, V. *Chem. Rev.* **2014**, *114*, 4175–4205.

[35] Vinyard, D. J.; Ananyev, G. M.; Charles Dismukes, G. *Annu. Rev. Biochem.* **2013**, *82*, 577–606.

[36] Ooka, H.; Wang, Y.; Yamaguchi, A.; Hatakeyama, M.; Nakamura, S.; Hashimoto, K.; Nakamura, R. *Phys. Chem. Chem. Phys.* **2016**, *18*, 15199–15204.

[37] Ooka, H.; Takashima, T.; Yamaguchi, A.; Hayashi, T.; Nakamura, R. *Chem. Commun.* **2017**, *53*, 7149–7161.

[38] Ooka, H.; Yamaguchi, A.; Takashima, T.; Hashimoto, K.; Nakamura, R. *J. Phys. Chem. C* **2017**, *121*, 17873–17881.

[39] Ooka, H.; Figueiredo, M. C.; Koper, M. T. *Langmuir* **2017**, *33*, 9307–9313.

[40] Taboada, B.; Ciria, R.; Martinez-Guerrero, C. E.; Merino, E. *Nucleic Acids Res.* **2011**, *40*, D627–D631.

[41] Taboada, B.; Verde, C.; Merino, E. *Nucleic Acids Res.* **2010**, *38*, e130–e130.

[42] Kanehisa, M.; Goto, S. *Nucleic Acids Res.* **2000**, *28*, 27–30.

[43] Ogata, H.; Goto, S.; Sato, K.; Fujibuchi, W.; Bono, H.; Kanehisa, M. *Nucleic Acids Res.* **1999**, *27*, 29–34.

[44] Kanehisa, M.; Goto, S.; Kawashima, S.; Okuno, Y.; Hattori, M. *Nucleic Acids Res.* **2004**, *32*, D277–D280.

[45] Miyata, K.; Noguchi, K.; Terashima, I. *Photosynth. Res* **2012**, *113*, 165–180.

[46] Asashima, M. *Life Science 3rd Edition*; Yodosha, 2009.

[47] Nguyen, T. A.; Brescic, J.; Vinyard, D. J.; Chandrasekar, T.; Dismukes, G. C. *Mol. Biol. Evol.* **2011**, *29*, 35–38.

[48] Mulo, P.; Sicora, C.; Aro, E.-M. *Cell. Mol. Life Sci.* **2009**, *66*, 3697.

[49] Cramer, M.; Myers, J. *Arch. Mikrobiol.* **1952**, *17*, 384–402.

[50] Gualtieri, P.; Barsanti, L.; Rosati, G. *Arch. Microbiol.* **1986**, *145*, 303–305.

[51] Muradov, N. Z.; Veziroğlu, T. N. *Carbon-Neutral Fuels and Energy Carriers (Green Chemistry and Chemical Engineering)*; CRC Press, 2017.

[52] Armstrong, F. A.; Hirst, J. *Proc. Natl. Acad. Sci. U. S. A.* **2011**, *108*, 14049–14054.

[53] Cox, N.; Pantazis, D. A.; Neese, F.; Lubitz, W. *Acc. Chem. Res.* **2013**, *46*, 1588–1596.

[54] Popović, D. M. *Amino Acids* **2013**, *45*, 1073–1087.

[55] Blankenship, R. E. *Molecular Mechanisms of Photosynthesis*, 1st ed.; Wiley-Blackwell, 2002.

[56] Vogt, S.; Rhiel, A.; Weber, P.; Ramzan, R. *BioEssays* **2016**, *38*, 556–567.

[57] McCrory, C. C. L.; Jung, S.; Ferrer, I. M.; Chatman, S. M.; Peters, J. C.; Jaramillo, T. F. *J. Am. Chem. Soc.* **2015**, *137*, 4347–4357.

[58] McCrory, C. C.; Jung, S.; Peters, J. C.; Jaramillo, T. F. *J. Am. Chem. Soc.* **2013**, *135*, 16977–16987.

[59] Sathre, R.; Scown, C. D.; Morrow, W. R.; Stevens, J. C.; Sharp, I. D.; Ager, J. W.; Walczak, K.; Houle, F. A.; Greenblatt, J. B. *Energy Environ. Sci.* **2014**, *7*, 3264–3278.

[60] Peschek, G. A. *Biochim. Biophys. Acta* **1996**, *1275*, 27–32.

[61] Jacob, F.; Monod, J. *J. Mol. Biol.* **1961**, *3*, 318–356.

[62] Oehler, S.; Eismann, E. R.; Krämer, H.; Müller-Hill, B. *EMBO J.* **1990**, *9*, 973.

[63] Lupski, J. R.; Smiley, B. L.; Godson, G. N. *Molecular and General Genetics MGG* **1983**, *189*, 48–57.

[64] Hamoen, L. W.; Venema, G.; Kuipers, O. P. *Microbiology* **2003**, *149*, 9–17.

[65] Maid, U.; Valentin, K.; Zetsche, K. *Curr. Genet.* **1990**, *17*, 255–259.

[66] Turmel, M.; Lemieux, B.; Lemieux, C. *MGG* **1988**, *214*, 412–419.

[67] Schmetterer, G.; Valladares, A.; Pils, D.; Steinbach, S.; Pacher, M.; Muro-Pastor, A. M.; Flores, E.; Herrero, A. *J Bacteriol.* **2001**, *183*, 6429–6434.

[68] Alberts, B.; Johnson, A.; Lewis, J.; Raff, M.; Roberts, K.; Walter, P. *Molecular Biology of the Cell, 5th Edition*, 5th ed.; Garland Science, 2007.

167

[69] Moldave, K. *Annu. Rev. Biochem.* **1985**, *54*, 1109–1149.

[70] Noguchi, K.; Go, C.-S.; Terashima, I.; Ueda, S.; Yoshinari, T. *Funct. Plant Biol.* **2001**, *28*, 27–35.

[71] Noguchi, K.; Go, C.-S.; Miyazawa, S.-I.; Terashima, I.; Ueda, S.; Yoshinari, T. *Funct. Plant Biol.* **2001**, *28*, 37–47.

[72] Aro, E.-M.; Virgin, I.; Andersson, B. *Biochim. Biophys. Acta* **1993**, *1143*, 113–134.

[73] Bailey, S.; Thompson, E.; Nixon, P. J.; Horton, P.; Mullineaux, C. W.; Robinson, C.; Mann, N. H. *J. Biol. Chem.* **2002**, *277*, 2006–2011.

[74] Raven, J. A. *Physiol. Plant.* **2011**, *142*, 87–104.

[75] García-Plazaola, J. I.; Esteban, R.; Fernández-Marín, B.; Kranner, I.; Porcar-Castell, A. *Photosynth. Res* **2012**, *113*, 89–103.

[76] Campbell, D.; Eriksson, M.-J.; Öquist, G.; Gustafsson, P.; Clarke, A. K. *Proc. Natl. Acad. Sci. U. S. A.* **1998**, *95*, 364–369.

[77] Campbell, D.; Zhou, G.; Gustafsson, P.; Oquist, G.; Clarke, A. K. *EMBO J.* **1995**, *14*, 5457.

[78] Vinyard, D. J.; Gimpel, J.; Ananyev, G. M.; Cornejo, M. A.; Golden, S. S.; Mayfield, S. P.; Dismukes, G. C. *J. Biol. Chem.* **2013**, *288*, 5451–5462.

[79] Zhaxybayeva, O.; Gogarten, J. P.; Charlebois, R. L.; Doolittle, W. F.; Papke, R. T. *Genome Res.* **2006**, *16*, 1099–1108.

[80] Häder, D.-P.; Lebert, M.; Richter, P. *Adv. Space. Res.* **1998**, *21*, 1277–1284.

[81] Diehn, B. *Science* **1973**, *181*, 1009–1015.

[82] Daiker, V.; Häder, D.-P.; Richter, P. R.; Lebert, M. *Planta* **2011**, *233*, 1055–1062.

[83] Matsunaga, S.; Takahashi, T.; Watanabe, M.; Sugai, M.; Hori, T. *Plant Cell Physiol.* **1999**, *40*, 213–221.

[84] Mikolajczyk, E.; Diehn, B. *Photochem. Photobiol.* **1975**, *22*, 269–271.

[85] Meyer, R.; Hildebrand, E. *J. Photochem. Photobiol. B* **1988**, *2*, 443–453.

[86] Drews, G. *Photosynth. Res* **2005**, *83*, 25–34.

[87] Häder, D.-P. *Arch. Microbiol.* **1987**, *147*, 179–183.

[88] Porterfield, D. M. *Biol. Bull.* **1997**, *193*, 229–230.

[89] Ooka, H.; Ishii, T.; Hashimoto, K.; Nakamura, R. *RSC Adv.* **2014**, *4*, 20693–20698.

[90] Hashimoto, K.; Nakamura, R.; Ooka, H.; Ueda, I.; Matsuda, H. Method for Concentrating Microalga Culture Fluid and Apparatus Therefor (WO2014136574A1). 2014.

[91] Zhu, X.-G.; Long, S. P.; Ort, D. R. *Curr. Op. Biotechnol.* **2008**, *19*, 153–159.

[92] Blankenship, R. E. et al. *Science* **2011**, *332*, 805–809.

[93] Work, V. H.; Beliaev, A. S.; Konopka, A. E.; Posewitz, M. C. *Biofuels* **2012**, 103–105.

[94] Biello, D. *Sci. Am.* **2011**, *305*, 58–65.

[95] Kim, J.; Yoo, G.; Lee, H.; Lim, J.; Kim, K.; Kim, C. W.; Park, M. S.; Yang, J.-W. *Biotechnol. Adv.* **2013**, *31*, 862–876.

[96] Dassey, A. J.; Theegala, C. S. *Bioresour. Technol.* **2013**, *128*, 241–245.

[97] Gerardo, M. L.; Oatley-Radcliffe, D. L.; Lovitt, R. W. *Environ. Sci. Technol.* **2014**, *48*, 845–853.

[98] Hanotu, J.; Bandulasena, H. C. H.; Zimmerman, W. B. *Biotechnol. Bioeng.* **2012**, *109*, 1663–1673.

[99] Salim, S.; Vermuë, M. H.; Wijffels, R. H. *Bioresour. Technol.* **2012**, *118*, 49–55.

[100] Li, L.; Pan, G. *Environ. Sci. Technol.* **2013**, *47*, 4555–4562.

[101] Gualtieri, P.; Barsanti, L.; Passarelli, V. *Ann. Inst. Pasteur Microbiol.* **1988**, *139*, 717–726.

[102] Koritala, S. *J. Am. Oil. Chem. Soc.* **1989**, *66*, 133–134.

Chapter 5

General Conclusions

5.1 Summary of This Thesis

Throughout this thesis, the author has assessed multi-electron transfer regulation from microscopic to macroscopic viewpoints and has proposed that reactions can be regulated at the scale of the metal valence change, local pH, gene sequences, and cell motility. Through these approaches, the author has attempted to clarify the mechanistic origin which leads to the difference in activity between 3d-metals and 4d/5d rare metal catalysts, as well as gain insight into the evolutionary strategy of biological energy–material conversion.

In Chapter 2, the author has studied the oxygen evolution mechanism of amorphous iridium oxide (IrO_x) from the viewpoint of valence change and charge accumulation using *in-situ* spectroelectrochemical techniques. In contrast to 3d-metal catalysts such as MnO_2 or Fe_2O_3, the valence change of IrO_x ($Ir^{3+} \rightarrow Ir^{4+} \rightarrow Ir^{5+}$) was found to be more favorable than the overall OER process on thermodynamic and kinetic terms. The rate-limiting step was found to be the formation of an Ir^{5+} species with an absorption maximum at 450 nm (species A_{450}) based on *in-situ* evanescent wave spectroscopy. A different Ir^{5+} (absorption maximum: 410 nm) was found to exist prior to the rate-limiting step, further indicating that the charge accumulation process of $Ir^{3+} \rightarrow Ir^{4+} \rightarrow Ir^{5+}$ is not rate-limiting. On the basis of computation, the transition of Ir^{5+} to species A_{450} was found to be assignable to a spin transition of an oxygen ligand. Upon spin transition, this oxygen atom was found to spontaneously form an O–O bond with the adjacent oxygen atom. This result is in accord with the proposed mechanism that the generation of species A_{450} (spin inversion of an oxygen ligand) is the rate-limiting step of IrO_x.

The difference in the OER mechanism between IrO_x (valence change: smooth) and MnO_2 (valence change: rate-limiting) may be due to the difference in their electronic structures. The valence change of MnO_2 (and Fe_2O_3) was found to be rate-limiting due to charge disproportionation of the high-spin d^4 electronic

state. This is because charge disproportionation stabilizes the total electronic energy of the system by exchanging the orbital of the (originally) unpaired e_g electrons. On the other hand, IrO_x lacks e_g electrons due to the low-spin electronic structure. This would effectively suppress charge disproportionation in advance, allowing for a more favorable charge accumulation process. The favorable charge accumulation process on IrO_x allows the precursor of the rate-limiting step (Ir^{5+} with an absorption at 410 nm) to accumulate, facilitating the rate-limiting step of $Ir^{5+} \rightarrow$ species A_{450} (O–O bond formation). This is evident in the Tafel slope ($\frac{\partial E}{\partial \ln j} = 30$ mV/decade) which is known to occur only when the precursor of the rate-limiting step is in electrochemical equilibrium. These results give insight into the reason why 4d/4d rare metals are often more active than their 3d-metal counterparts, as the low-spin electronic configuration of the 4d/5d-metals would enhance the efficiency of the charge accumulation process.

In Chapter 3, the author has studied the effect of local pH on the competition of CO_2 reduction and hydrogen evolution (HER). There are two presumable pathways for the evolution of hydrogen in aqueous electrolytes: A proton-concentration-dependent pathway ($2\,H^+ + 2\,e^- \rightarrow H_2$, proton reduction) and a proton concentration independent pathway ($2\,H_2O + 2\,e^- \rightarrow H_2 + 2\,OH^-$, water reduction). Due to the existence of multiple pathways, the net hydrogen evolution rate is expected to be the sum of these reaction rates. However, because the pH is not an explicit factor in the presiding d-band theory (computational hydrogen electrode model) of electrocatalysis, these pathways cannot be distinguished, and therefore, the competition of CO_2 reduction with HER is still unclear.

In order to address this challenge, the author has explicitly differentiated between the two HER pathways by using a Cu rotating disc electrode (RDE) system as a means to control the local pH at the electrode. The onset potential of proton reduction observed experimentally was found to be more than 600 mV more positive than that for water reduction, suggesting the existence of a smaller

reaction barrier for proton reduction. Although the majority of the overpotential difference was assignable to the change of the pH near the electrode, the intrinsic overpotential for proton reduction was still smaller by *ca.* 200 mV, indicating that proton reduction and water reduction are fundamentally different chemical reactions. Accordingly, these two pathways interact differently with CO_2 reduction. While the water reduction pathway was inhibited drastically in the presence of CO_2, the proton reduction pathway showed negligible changes in the reaction rate. This selective inhibitory effect was assigned to the adsorbed CO, which is formed only under water reduction potentials as observed using *in-situ* Fourier-transform infrared (FTIR) spectroscopy. The fact that CO_2 cannot inhibit proton reduction which has a lower overpotential than water reduction indicates that proton reduction would become the major reaction if local pH effects did not take place. The importance of local pH on the selectivity of CO_2 reduction shown in this study is expected to help develop further efficient systems for the reduction of CO_2.

Finally, in Chapter 4, the author has studied how biology regulates multi-electron transfer processes at the genetic and cellular scale. Photosynthesis is the process of acquiring electrons from water (oxygen evolution) and reducing CO_2 (CO_2 reduction) using the obtained reducing power. Previous studies have focused mainly on the optimization at the protein structure level, such as the structure of the active site or the role of hydrogen bonding networks. In contrast, because bioenergetics plays such a fundamental role in biology and evolution, the author hypothesized that optimization would occur, not only within each enzyme, but at the various levels within the organism which utilizes said enzyme.

In order to confirm this hypothesis and to gain insight into novel methods of multi-electron transfer regulation, the author has studied the genetic sequence of photosystem II (PS II) in comparison with that of cytochrome c oxidase (COX). Even though PS II and COX both represent the two main energy pathways in

174

Nature, and are reverse reactions of each other, the two enzymes were found to possess distinctly different genetic structures. Namely, the active site (D1 subunit) of PS II was found to be synthesized separately from the rest of the enzyme, whereas the major subunits of COX were found to be regulated simultaneously. The difference in genetic structure suggests that instead of developing a stable, light-harvesting, oxygen evolving catalyst (PS II), Nature chose to frequently repair an easily-deactivated enzyme. This can become a valid strategy, only if the repair cost is minimized as clarified based on the genetic structure analysis. The author has further confirmed how photosynthesis has emphasized the stability and the balance between energy consumption and generation by studying the photomotility of green algae *Euglena gracilis*. *E.* gracilis cells were found to retreat from the light source upon blue light (400 nm) irradiation, whereas green light (530 nm) was found to attract *E.* gracilis cells. Taking into account the absorption spectra of chlorophyll, the observed wavelength dependence is in accord with the hypothesis that photosynthetic organisms do not attempt to maximize the power conversion efficiency of photosynthesis itself, but instead, maintain the balance between the energy gain from photosynthesis, and the energy loss due to cell damage (photoinhibition). The finding that biology regulates multi-electron transfer processes by optimizing genetic sequences and motility responses gives insight not only into the development of next-generation artificial multi-electron systems, but also gives insight into the fundamental evolutionary concepts of biology.

5.2   Closing Remarks

One of the ultimate goals of developing efficient multi-electron transfer systems is to enhance the sustainability of human society. The author has initially entered the field, precisely because of his interest in sustainability, and because of the potential of chemistry to change the flow of energy and materials between human society and the biosphere. As mankind has often looked upon biological systems for ideas, here, the author presents his view of how biology operates energy–material conversion, based on the research presented in this study.

The importance of an efficient energy–material conversion strategy in biology has been mentioned multiple times in this thesis (See introductions of Chapter 3 and 4). For example, the increased energy per gene, due to the evolution of mitochondria has been proposed to be a prerequisite of biological complexity. The dominance of a specific species in an ecosystem is also ultimately determined by the amount of energy and materials they can uptake from the environment relative to other competing species. Therefore, the energy–material conversion performed through multi-electron transfer reactions is the fundamental basis for life.

However, as the author has shown in Chapter 4, one of the most successful forms of biological energy–material conversion, is highly inefficient. Photosynthesis has an overall energy conversion efficiency in the order of 0.1–1 %, which is more than a magnitude lower than what modern technology can achieve. Therefore, despite the importance of energy–material conversion efficiency, photosynthesis does not seem to have been optimized to maximize its efficiency. Instead, it has used multiple strategies to suppress the damage from excessive solar radiation, either by minimizing the repair cost (gene level optimization), or by adjusting the light intensity (motility response).

This seemingly inefficient evolutionary strategy is the opposite of cancer cells. The usage of aerobic fermentation in favor of aerobic respiration as the primary

energy acquisition pathway inhibits apoptosis (programmed cell death), which allows cells to continue to divide without limit. Furthermore, while aerobic respiration is more efficient in terms of energy efficiency (ATP per glucose), fermentation is the kinetically favored pathway, quickly depleting the available resources from the environment. Ultimately, the cancer cells deprive the host of the necessary nutrients, leading to the death of the host. However, upon the death of the host, the cancer cell, which has cut off its only access to nutrients outside the host, brings death unto itself. The collapse of the ecosystem shown here portrays the results of an overly selfish energy–material conversion strategy. In the eyes of the author, this is a miniature representation of the relationship between current human society and the natural environment.

From this perspective, the sustainable energy cycle presented in the very beginning of this thesis (Figure 1.1) has strong implications. Human society as a whole is still relying on the combustion of fossil fuels to provide the majority of its energy needs. However, as in Nature, human society must close the energy–material conversion cycle, not only by reducing the amount of fossil fuel combustion but also by acquiring the electrons and protons from a different source, such as water molecules. As mentioned in the introduction of Chapter 3, the sustainable energy–material conversion cycle we know of today, based on the four-electron transfer between water and oxygen, was not sustainable when it first came into existence, because the accumulation of toxic oxygen caused a mass destruction of the ecosphere. Only when oxygen levels stabilized due to the evolution of a consumption process (aerobic respiration) has the biosphere regained its sustainability. In this way, sustainability can be achieved only when the system in question becomes a transient entity between the flow of electrons and protons. Biology has achieved this by evolving a process to recycle oxygen, and in the same way, mankind must also evolve a process to recycle our waste products. Upon doing so, the biosphere and the human society form a

single, sustainable, energy–material conversion loop: The electrons and protons obtained from water briefly appear as components, before being reacquired by oxygen, yielding the starting molecule (water). It is towards this sustainable energy scenario that mankind must aspire to. The insight presented in this thesis shows both how Nature has acquired this sustainability, as well as possible ways mankind may also realize this ultimate goal.

List of Publications

Publications included in this thesis:

1. "Light-Induced Cell Aggregation of *Euglena gracilis* Towards Economically Feasible Biofuel Production" H. Ooka, T. Ishii, K. Hashimoto, R. Nakamura, *RSC Adv.*, **2014**, *4*, 20693–20698.

2. "Legitimate Intermediates of Oxygen Evolution on Iridium Oxide Revealed by *In Situ* Electrochemical Evanescent Wave Spectroscopy" H. Ooka, Y. Wang, A. Yamaguchi, M. Hatakeyama, S. Nakamura, K. Hashimoto, R. Nakamura, *Phys. Chem. Chem. Phys.*, **2016**, *18*, 15199–15204.

3. "Competition Between Hydrogen Evolution and Carbon Dioxide Reduction on Copper Electrodes in Mildly Acidic Media" H. Ooka, M. C. Figueiredo, M. T. M. Koper, *Langmuir*, **2017**, *33*, 9307-9313.

4. "Element Strategy of Oxygen Evolution Electrocatalysis Based on *In Situ* Spectroelectrochemistry" H. Ooka, T. Takashima, A. Yamaguchi, T. Hayashi, R. Nakamura, *Chem. Commun.*, **2017**, *53*, 7149–7161.

5. "Efficiency of Oxygen Evolution on Iridium Oxide Determined from the pH Dependence of Charge Accumulation" H. Ooka, A. Yamaguchi, T. Takashima, K. Hashimoto, R. Nakamura, *J. Phys. Chem. C*, **2017**, *121*, 17873–17881.

6. "Design Strategy of Multi-electron Transfer Catalysts Based on a Bioinformatic Analysis of Oxygen Evolution and Reduction Enzymes" H. Ooka, K. Hashimoto, R. Nakamura, *Mol. Inform.* (under review).

Other Publications:

7. 「水分解触媒のための元素戦略」 大岡英史、山口晃、橋本和仁、中村龍平、化学工業、**2014**、*65*, 15–20.

8. "Evidence that Crystal Facet Orientation Dictates Oxygen Evolution Intermediates on Rutile Manganese Oxide" H. Kakizaki, H. Ooka, T. Hayashi, A. Yamaguchi, K. Hashimoto, R. Nakamura, *Adv. Funct. Mater.* (in press).

9. "Selective Electrocatalytic Reduction of Nitrite to Dinitrogen based on Decoupled Proton-Electron Transfer" D. He, Y. Li, H. Ooka, Y. K. Go, F. Jin, S.-H. Kim, R. Nakamura, *J. Am. Chem. Soc.* (in press).

Acknowledgements